

American University in Cairo

## AUC Knowledge Fountain

---

Theses and Dissertations

Student Research

---

Fall 2014

### Novel on-chip applications using silicon photonics

Rania Gamal

*The American University in Cairo AUC*

Follow this and additional works at: <https://fount.aucegypt.edu/etds>



Part of the [Electrical and Computer Engineering Commons](#)

---

#### Recommended Citation

##### APA Citation

Gamal, R. (2014). *Novel on-chip applications using silicon photonics* [Master's Thesis, the American University in Cairo]. AUC Knowledge Fountain.

<https://fount.aucegypt.edu/etds/1821>

##### MLA Citation

Gamal, Rania. *Novel on-chip applications using silicon photonics*. 2014. American University in Cairo, Master's Thesis. *AUC Knowledge Fountain*.

<https://fount.aucegypt.edu/etds/1821>

This Master's Thesis is brought to you for free and open access by the Student Research at AUC Knowledge Fountain. It has been accepted for inclusion in Theses and Dissertations by an authorized administrator of AUC Knowledge Fountain. For more information, please contact [thesisadmin@aucegypt.edu](mailto:thesisadmin@aucegypt.edu).



THE AMERICAN UNIVERSITY IN CAIRO

School of Science and Engineering

# Novel On-Chip Applications Using Silicon Photonics

A Thesis submitted to  
The Department of Electronics Engineering  
In Partial Fulfillment of the Requirements for  
The Degree of Master of Science

---

**Rania Gamal**

Supervised By

**Dr. Mohamed Swillam**

**Dr. Yehea Ismail**

2014

The American University in Cairo  
School of Science and Engineering

Novel On-Chip Applications Using Silicon Photonics

A Thesis Submitted By  
Rania Gamal

Submitted to  
The Department of Electronics Engineering  
In Partial Fulfillment of the Requirements for  
The Degree of Master of Science

---

Dr. Mohamed Swillam  
Thesis Advisor  
Assistant Professor in the Physics Department  
Associate Chair of Physics Department  
The American University in Cairo

---

Date

---

Dr. Karim Addas  
Examiner  
Assistant Professor in the Physics Department  
The American University in Cairo

---

Date

---

Dr. Ziad A. El-Sahn  
Examiner  
Assistant Professor in the Electronics Engineering Department  
Alexandria University

---

Date

---

Dr. Yehea Ismail  
Professor in the Electronics Engineering Department  
The American University in Cairo  
Director of the Center for Nanoelectronics and Devices  
Zewail City for Science and Technology

---

Date

© 2014  
Rania Gamal

*To Nasser and Nivan,*

# Acknowledgements

First, I would like to thank my dear husband who made sure I was well-fed while I spend an untold amount of hours plastered to my computer screen. And whose never-faltering confidence in me was always a mattress to fall upon in my less fortunate days. And for about a thousand other things that I cannot possibly fit in the space of this acknowledgement!

I would also like to express my gratitude towards my supervisors, Dr. Yehea Ismail and Dr. Mohamed Swillam. A very warm thank you to Dr. Yehea who founded a prestigious research center in an impressive amount of time, and gave the opportunity for people like myself to start their research career on a solid foundation. Big thanks to him for being kind, attentive and continuously supportive towards his research team, and whose brilliance and enthusiasm never ceased to inspire us. And a big thanks to Dr. Mohamed Swillam, who worked with me side-by-side for the last two years, and who has single-handedly taught me everything I know about photonics! He always had time for his students despite his very busy schedule and many responsibilities. I hope I can make you both proud.

A big thank you to my colleagues for always making me laugh, and for being true team players; I will miss them very much. A special thanks to Ms. Gehan Kamel; I have only met Ms. Gehan for a few times during the past two years, but she was always amazingly helpful and generous with her time—a solid example of what a kind and hardworking person is.

And lastly, my mother, the woman who taught me that "math is a game" and that building blocks and solving puzzles is far more fun than playing with dolls. Mom, you shaped who I am in so many (positive) ways, and I could not be more grateful.

*“The important thing is not to stop questioning.”*

- *Albert Einstein*

# Abstract

The emerging field of silicon photonics offers solutions to designing CMOS-compatible optical devices. By taking advantage of the immense fabrication infrastructure offered by the silicon industry, it would be possible to design optical structures that are smaller, faster, less-power consuming and cheaper than traditional, non-silicon-based optical devices. In this dissertation, the design and performance testing of two novel silicon photonic structures are presented: 1) Silicon nanowire ridge waveguide for sensing applications at the optical transmission frequency. 2) Doped silicon plasmonic structures for negative-index, epsilon-near-zero and sensing applications at the mid-infrared.

For the first design, silicon nanowires are arranged in a ridge shape to act as a sensitive medium. Most conventional optical sensors rely on evanescent field detection, where only the tail of the incident wave contributes to the sensing process. Silicon nanowires, on the other hand, allow a large portion of the light wave to be present in the low-index-region, which is comprised of the gaps between the nanowires. This feature provides an opportunity for the optical wave to be vastly affected by the refractive index of the gaps between the nanowires. Thus, by introducing materials-under-test, or analytes, to the gaps, the optical signal response is heavily altered, hence, providing a much larger sensitivity than evanescent field sensors. Previous literature has reported on rib-shaped silicon nanowire sensors. We show that the proposed design is more superior in several areas. Firstly, simulations show that ridge-shaped sensors respond slightly more strongly to refractive-index changes than rib-shaped sensors. This could be due to their slightly larger optical overlap with their surroundings, provided by the inherently larger dimensions of the ridge shape. They can also detect up to a  $10^{-8}$  refractive-index-changes in the surrounding environment. Secondly and more importantly, single-mode operation, which is usually mandatory for most optical sensor configurations, can be guaranteed using more flexible dimensions for the ridge-shaped nanowire waveguide than for its rib-shaped counterpart. This provides a fabrication convenience, since devices with larger dimensions are generally cheaper and easier to manufacture. Additionally, since the ridge waveguide sports a wide low-thickness region, it can cover the substrate and safe-guard it against erosion during the fabrication process. To further characterize our design, the ridge-shaped silicon nanowire waveguide was put in a bimodal interferometer sensor configuration. The sensitivity obtained through FDTD simulations proved to be very high; its value was comparable to recently reported sensitivities using much larger footprints. This very high sensitivity-to-footprint ratio, along with the CMOS compatibility of the proposed design, deems it as a suitable candidate for on-chip integration.



In the second portion of this dissertation, we aim to model and characterize high-confinement plasmonic devices using doped silicon in the mid-infrared range. The mid-infrared range is home to some important applications such as molecular sensing, environmental monitoring and security applications. Traditional plasmonic devices possess some much desired features that may be utilized in the mid-infrared. These include hosting a high surface sensitivity, and having the ability to guide and confine light through subwavelength structures, including sharp bends. However, much of these features are exclusive to the near-infrared and visible frequencies, where the plasma resonance of conventional plasmonic materials lie. This is because conventional materials tend to suffer from low confinement in the mid-infrared region, and are rendered inconvenient for applications that require high confinement such as sensing and on-chip communications. For this reason and for its CMOS compatibility, doped silicon plasmonics seems to be a viable solution. We demonstrate that plasma resonance tunability can be achieved through controlling the doping level. Moreover, the dispersion characteristics of doped silicon devices were analyzed for different applications at the mid-infrared region, and displayed valuable phenomenon such as negative dispersion, which can be utilized for slow light and metamaterial applications, and epsilon-near-zero characteristics, that can be used for extraordinary transmission. The mid-infrared dispersion was studied thoroughly for multiple structures, including the slot structure and the rectangular shell structure. The potential for biological and environmental sensing for the aforementioned structures, as well as for a doped silicon nanoparticle was investigated and very high sensitivity was achieved. In addition, the performance of the slot structure in the negative dispersion region was established through using the waveguide as a slow light medium. Moreover, plasmonic structures that can be used for on-chip light-guiding, such as bends and junctions were evaluated. FDTD simulations showed superior performance through successful light-splitting in gaps as wide as  $1\mu\text{m}$ .

# Contents

Acknowledgements.....	iv
Abstract.....	vi
List of Figures .....	x
List of Abbreviations .....	xiv
Chapter 1: Introduction .....	1
Chapter 2: Overview on Photonic Biosensors .....	6
2.1    What Is a Biosensor?.....	6
2.2    Brief Overview of Immobilization .....	7
2.3    Photonic Biosensors.....	9
2.3.1    Evanescent Field Sensors .....	10
2.3.2    Novel waveguides for biosensing applications .....	14
2.4    The FDTD Method.....	17
Chapter 3: Bimodal Optical Biosensor Based on Silicon Nanowire Ridge Waveguide .....	17
3.1    Silicon Nanowire Ridge Waveguide (SNRW).....	17
3.2    Design Consideration for the SNRW .....	18
3.3    The Relative Sensitivity of the SNRW.....	21
3.4    Bimodal Interferometric Waveguide based on SNRW.....	24
Chapter 4: Overview on Mid-Infrared Plasmonics.....	28
4.1    Plasmonics .....	28
4.1.1    Surface Plasmon Polaritons .....	28
4.1.2    Drude Model .....	30
4.1.3    Surface Plasmons Applications .....	32
4.2    The Mid-Infrared (Mid-IR).....	36
4.2.1    Mid-IR Applications.....	36
4.2.2    Conventional Plasmonics at the Mid-IR.....	37
4.2.3    Designer Plasmonics .....	37
Chapter 5: Mid-IR Doped Silicon Plasmonics.....	39
5.1    Material Modelling .....	39
5.1.1    Determining the Doping Concentration .....	39
5.1.2    Relationship between Doping Concentration and Plasma Resonance.....	40
5.1.3    Material Modeling .....	44

5.1.4	Single-Interface Propagation .....	45
5.2	The Finite-Width Slot Waveguide .....	46
5.2.1	Modal and Dispersion Simulations for Slot Waveguide.....	46
5.2.2	Applications for the Plasmonic Slot Waveguide .....	51
5.3	Rectangular Shell Waveguide .....	53
5.4	Doped Silicon SIS Waveguide.....	56
5.4.1	90 Degree Bends .....	60
5.4.2	T-Junction Splitters .....	61
5.4.3	X-Junction Splitters .....	62
5.4.4	Propagation Losses in SIS Waveguides .....	65
5.5	Doped Silicon Nanoparticles .....	66
Chapter 6: Conclusion .....		66
Publications.....		69
References .....		70

# List of Figures

Figure 2.1. Simplified biosensor model.....	7
Figure 2.2. Common surface biofunctionalization strategies (adopted from [7]) .....	8
Figure 2.3. Top view of Mach-Zehnder sensor .....	11
Figure 2.4. Structure of the bimodal waveguide (taken from [15]).....	12
Figure 2.5. Grated optical waveguide .....	13
Figure 2.6. The ring resonator waveguide .....	14
Figure 2.7. Modal profile of a slot waveguide .....	15
Figure 2.8. Displacement of the electric and magnetic field vector components in a cubic unit cell of the Yee space lattice. ....	17
Figure 3.1. The SNRW structure. The nanowires are arranged in a ridge shape and placed on top of a silicon dioxide substrate. (a) Front view. (b) 3D view. ....	19
Figure 3.2. (a) Width, $w$ , and height, $h$ , of the rib (higher-thickness region in the ridge waveguide). (b) 2D map showing single-mode vs. multi-mode operation of various dimensions of the rib waveguide. (c) fundamental mode of single-mode SNRW. (d) first-order mode of SNRW with small height. (e) first-order mode of SNRW with large height. ....	20
Figure 3.3. Percentage change of effective index for the SNRW and the BSRW as a response to the change in the surrounding environment.....	21
Figure 3.4. (a) Rib nanowire waveguide. (b) SOI grating waveguide. (c) optical mode for rib nanowires waveguide. (d) optical mode for SOI grating waveguide.....	22
Figure 3.5. Percentage change in effective index for a refractive index change of the surrounding-environment for SNRW, rib nanowires, and SOI gratings. ....	23
Figure 3.6. Percentage change of effective index for the SNRW as a response to minute changes in the surrounding environment.....	24
Figure 3.7. (a) Fundamental mode and (b) first-order mode of dual-mode section in the SNRW bimodal configuration.....	25
Figure 3.8. 3D SNRW bimodal waveguide. ....	25
Figure 3.9. Propagation profile of the $y$ -component of the electric field through a $10\mu\text{m}$ -long SNRW bimodal sensor (top view) .....	26
Figure 3.10. Normalized transmitted power spectrum for different refractive index surroundings ( $n_{\text{surr}}$ ) with rib width = $2\mu\text{m}$ .....	26
Figure 3.11. Normalized transmitted power spectrum for different refractive index surroundings ( $n_{\text{surr}}$ ) with rib width = $1.5\mu\text{m}$ .....	28

Figure 4.1. (a) Propagation of surface plasmon polaritons on a metal/dielectric interface, illustrating the electric field lines and charge polarization on the surface. (b) Modal profile of surface plasmons. ....	29
Figure 4.2. The Kretschmann configuration.....	35
Figure 5.1. Slot structure; inset shows slot mode with gap width, $W_{gap}$ , rib width, $W_{rib}$ , and height, $H$ .....	40
Figure 5.2. Doping concentration vs. modal effective index for $\lambda = 3\mu\text{m}$ , $5\mu\text{m}$ and $10\mu\text{m}$ for a slot waveguide with $W_{gap} = 5\text{nm}$ and $W_{rib} = 50\text{nm}$ . ....	40
Figure 5.3. Doping concentration vs. modal effective index for $\lambda = 3\mu\text{m}$ , $5\mu\text{m}$ and $10\mu\text{m}$ for a slot waveguide with a $W_{gap} = 100\text{nm}$ and $W_{rib} = 50\text{nm}$ . ....	41
Figure 5.4. The real permittivity of doped silicon with $N_d \approx 5 \times 10^{20}\text{cm}^{-3}$ versus the wavelength. Assuming that the surrounding dielectric material is air, the dispersion will be maximum near $3\mu\text{m}$ . ....	44
Figure 5.5. Single-interface propagation of a 400nm (a) doped silicon slab, (b) silver slab on an $\text{SiO}_2$ substrate. ....	45
Figure 5.6. The dispersion relation for the silicon slot structure with a 5nm gap and a 100nm gap. Insets a and b belong in Region 1 and describe the dielectric mode for the 100nm gap slot waveguide and the 5nm gap slot waveguide, respectively. Insets c and d belong in Region 2 and depict a leaky mode for the 100nm gap slot waveguide and the 5nm gap slot waveguide, respectively.....	46
Figure 5.7. The dispersion relation for the slot structure showing the 3 main regions: Region 1: dielectric region, Region 2: negative dispersion, Region 3: plasmonic region.	47
Figure 5.8. Dispersion curves for the 5nm gap slot structure for three different doping concentrations. The plasma resonance exists around 3, 5, and $10\mu\text{m}$ . ....	48
Figure 5.9. Dispersion curves for the 100nm gap slot structure for three different doping concentrations. The plasma resonance exists around 3, 5, and $10\mu\text{m}$ . ....	49
Figure 5.10. Plot of the effective modal index near resonance against the gap width. The plot shows the curves for a doped silicon slot with three doping concentrations with their resonances indicated in the legend; the rib width is fixed at 50nm. ....	50
Figure 5.11. Plot of the effective modal index near resonance against the gap width for the doped silicon slot. The rib widths are set at 50, 100 and 250nm, and the doping concentration is fixed at $5 \times 10^{20}\text{cm}^{-3}$ , while the gap width is varied from 5nm to 100nm. ....	51
Figure 5.12. The solid curves depict the dispersion of a 100nm gap width, 50nm rib width doped silicon slot waveguide immersed in a dielectric medium. The dashed curves depict the dispersion of a slot waveguide with a dielectric filling in the gap only.	52

Figure 5.13. The time plot of the output electric field pulse from a plasmonic doped silicon slot waveguide and a dielectric silicon slot waveguide. ....	53
Figure 5.14. Performance of a rectangular shell sensor. (a) The rectangular shell structure with gap width, $W_x$ , equal to 30nm, and gap height, $W_y$ , equal to 50nm and variable thickness, $t$ . (b) The dispersion relation for a doped silicon rectangular shell waveguide with plasma resonance around $3\mu\text{m}$ for $t = 25, 35$ and $45\text{nm}$ . ....	54
Figure 5.15. Dispersion relations for the $30 \times 50\text{nm}$ rectangular shell waveguide for three different doping concentrations. ....	55
Figure 5.16. The dispersion relations for the rectangular shell waveguide using doped silicon with plasma resonance around $10\mu\text{m}$ with fillings of $n = 1, 1.25$ and $1.5$ . ....	56
Figure 5.17. SIS structure using doped silicon, where $H$ is the slot height and $W_{gap}$ is the gap width of the slot. ....	56
Figure 5.18. Dispersion of SIS doped silicon waveguide showing the real part of the effective refractive index against the wavelength. There are 4 regions: 1. Radiative region. 2. Cut-off region. 3. Negative-dispersion region. 4. Plasmonic region. The modal profile for each region is shown in the insets. ....	57
Figure 5.19. Dispersion of an SIS doped silicon waveguide showing the plasmonic region. ....	58
Figure 5.20. Dispersion of SIS doped silicon waveguide showing the real part of the effective refractive index against the wavelength for a 100nm gap and heights of 20, 50, and 100nm. ....	58
Figure 5.21. Dispersion of an SIS doped silicon waveguide showing the real part of the effective refractive index against the wavelength for a 200nm gap and heights of 20, 50, and 100nm. ....	59
Figure 5.22. Dispersion of an SIS doped silicon waveguide showing the real part of the effective refractive index against the wavelength for a $1\mu\text{m}$ gap and heights of 20, 50, and 100nm. ....	59
Figure 5.23. 2D FDTD simulation showing the propagation of $5\mu\text{m}$ signal through $10\mu\text{m}$ long slot waveguides with: (a) 5nm gap, (b) 25nm gap, (c) 50nm gap and (d) 100nm gap. ....	60
Figure 5.24. Transmission through a 100nm gap 90 degree bend. Inset shows the propagation profile within the bend. ....	61
Figure 5.25. (a) Transmission spectrum of a 100nm doped Si t-junction splitter. (b) Propagation profile of a doped Si t-junction splitter. ....	61
Figure 5.26. Transmission spectrum of a doped Si t-junction splitter with a 200nm wide input arm and 100nm wide output arms. ....	62

Figure 5.27. (a) Transmission spectrum of a 100nm gap doped Si x-junction splitter. (b) Propagation profile of a doped Si x-junction splitter. ....	63
Figure 5.28. Transmission spectrum of a 100nm gap doped Si x-junction splitter with a 300nm-wide input arm and 100nm-wide output arms.....	64
Figure 5.29. Transmission spectrum of an x-junction splitter with a 1 $\mu$ m-wide gap. ....	64
Figure 5.30. Transmission spectrum of an x-junction splitter with a 2 $\mu$ m-wide gap. ....	64
Figure 5.31. Propagation losses for a 1 $\mu$ m-long SIS waveguide with a 100nm-wide gap and a 200nm-wide gap. ....	65
Figure 5.32. Nanodisk sensor based on doped silicon with plasma resonance at 3 $\mu$ m, with surrounding refractive index, $n = 1, 1.25$ and $1.5$ . Inset shows the mode profile at 3 $\mu$ m. ....	66

# List of Abbreviations

CMOS	Bulk silicon ridge waveguide
CMOS	Complementary metal-oxide semiconductor
ENZ	Epsilon-near-zero
FDTD	Finite-difference-time-domain
Mid-IR	Mid-infrared
MIM	Metal-insulator-metal
MZI	Mach-Zehnder Interferometer
NIR	near-infrared
OCF	Optical confinement factor
PML	Perfectly matched layer
RIU	Refractive-index-unit
SFR	Sensitivity to footprint ratio
SIS	Silicon-insulator-silicon
SNOW	Silicon nanowire optical waveguide
SNRW	Silicon nanowire ridge waveguide
SOI	Silicon-on-insulator
SPP	Surface plasmon polariton
VLSI	Very-large-scale integration



# Chapter 1: Introduction

The persistent need to access the internet from everywhere is probably what inspired the use of optical solutions rather than electronic ones. Where the electronic systems based on copper failed at fulfilling the ever-expanding bandwidth and distance requirements, the optical systems flourished. High-speed computers also benefited from the enormous speeds of optical interconnects. Today, optical systems are paving their way into applications in the medical field, including diagnostics, therapeutics and imaging. However, optical devices are typically bulky, and made from non-standardized components such as III–V-based compounds such as indium phosphide (InP), gallium arsenide (GaAs) and lithium niobate (LiNbO<sub>3</sub>). There is hardly any automation in the fabrication of these devices, as they are usually custom-made, and assembled manually. Thus, optical devices are sometimes viewed as unpractical solutions due to the large expenses required in their production. This hurdle may be overcome by using an optical technology that can be batch fabricated, and made available at a low cost to the mass market. For this reason, a lot of effort has been put recently into realizing optical components that are based on silicon; this research field is commonly referred to as “silicon photonics.” Perhaps the main merit of working with silicon is to take advantage of the readily available knowledge gained from years of study done on this material by the microelectronics industry. This is a well-understood material, and its fabrication infrastructure is immense.

Many doors are unlocked when one contemplates the prospects of taking advantage of the manufacturability provided by the silicon technology, which includes the ease of miniaturization and integration. For instance, optical components could be easily integrated with one another on a single-chip to form compact optical systems that are eligible for batch fabrication. This could allow the production of low-cost, robust photonic devices. Mass producing such devices will greatly increase the commercial marketplace of optical components. Another possibility brought upon by the use of silicon photonics is the prospect of integrating optical components alongside electronic components using the CMOS technology. Such integration can provide new and endless possibilities for the optoelectronic industry [1].

In this dissertation, we study the performance of novel silicon photonic devices in two spectral regions: the optical transmission wavelength centered around 1.55 $\mu\text{m}$ , as well as in the mid-infrared (mid-IR) region (2 - 20 $\mu\text{m}$ ). Traditionally, optical devices guide the

light in the high-index medium. The proposed devices, alternatively, are designed with specific parameters that allow the light to propagate in the low-index medium, the purpose of that will be discussed later. Ultimately, the main goal for our devices is to provide high confinement so as to be eligible for use in on-chip applications. The performance of our devices in several of these applications, such as sensing and slow light applications, is studied.

In the first spectral region—wavelength around  $1.55\mu\text{m}$ —we designed a miniaturized photonic sensor based on silicon nanowires. The testing and characterization of the design was carried out through the use of finite-difference-time-domain (FDTD) simulation software. There were three primary challenges in this design: 1) to ensure that the nanowires are capable of transmitting light with minimum leakage. 2) To ensure that the device reacts greatly to changes in the surrounding environment (i.e., make sure it is highly sensitive). 3) To improve upon existing silicon photonic sensors. In general, sensitivity is defined as the change in a certain parameter (e.g. phase or resonance shift) in the output signal per a change in a physical parameter (e.g. dimensions, surrounding refractive index, and temperature) in the sensing system. For our purposes, we define sensitivity as the change in the effective refractive index of the sensor per the change in the surrounding refractive index. As mentioned beforehand, our devices are meant to guide light in the low-index region. In the case of silicon nanowires, the spacing between the wires along with their diameters can allow the incident light to see them as an effective index medium. The effective index would have an average value between the refractive index of silicon and the surrounding environment, or the cladding (usually air by default). Thus, this effective medium will have an overall larger index than the air, and should be capable of guiding the light; this resolves our first design challenge. The main advantage, and purpose, of using nanowires is seen in sensing applications—specifically biosensing applications, where a complex fluid is detected. In these scenarios, the material being sensed, or the analyte, will be inserted in the gaps between the nanowires, thus, altering the refractive index of the cladding. Hence, the light wave within the gaps amid the silicon nanowires will overlap completely with the analyte, and hence, the overall effective index of the waveguide will be altered accordingly. As will be seen in future chapters, optical sensing configurations rely upon measuring the effective index change induced upon the introduction of the analyte to the optical waveguide. The majority of optical sensors rely on evanescent field detection where only the tail of the light interacts with the analyte. Since our design provides a much larger overlap between the light and the analyte, it is expected to be far more sensitive than conventional devices; this addresses our second challenge.

Silicon nanowire sensors have been briefly investigated before [2], however, they were arranged in a small rib waveguide. The issue with such a waveguide is that it leaves a large area of the substrate exposed, and this could introduce fabrication challenges that could result in the erosion of the substrate surface during the etching process. Instead, we propose to use silicon nanowire ridge waveguides (SNRW), where the nanowires are arranged in the shape of a ridge. This design covers the entire substrate, and can dodge the fabrication inconvenience mentioned earlier. Moreover, as this device is physically bigger than the silicon nanowire rib waveguide (while still being miniature), the optical mode produced by this device is physically larger than that of the rib waveguide. This provides an even larger playfield for the light and analyte to interact and improving the sensitivity; this solves the third and final design challenge.

After addressing our main design goals, we needed to put our device to the test; this was done by basing it upon an optical sensing configuration. We chose to use the bimodal sensor configuration. The bimodal waveguide is a type of interferometric waveguide, where a straight waveguide supports a single mode in a certain section, and two modes in another section. These modes interfere with one another and produce an interference pattern at the output. The bimodal waveguide was chosen mainly for its simplicity. It is a straight waveguide that does not involve bends or junctions, as do popular configurations, such as ring-resonators and Mach-Zehnder interferometers (MZI). The presence of bends introduces a fabrication difficulty, as well as bending losses. The bending losses are especially exaggerated when the device is miniaturized, since this would require the bends to be more severe. Another advantage for using the bimodal waveguide is the fact that its compactness could allow for multiple sensing channels to co-exist, which could facilitate either the parallelization of sensing multiple features on a single-chip, or enhance the sensing of a single feature. Because this device is miniature and silicon-based, it is eligible for integration with the ever-trending lab-on-a-chip devices [3].

The second (and larger) focus of this dissertation is on photonic devices in the mid-IR range. This spectral area is a minefield for sensing applications, chiefly because it contains the 'vibrational fingerprints' of many relevant molecules, as well as atmospheric transmission windows which could be used for imaging and security applications. However, the mid-IR range is an under-researched area, as there has been technical difficulties in creating sources and detectors that functioned in this area until the mid-nineties. We explore this area through the use of plasmonic slot structures. Plasmonic structures are known for their unique ability to confine light to sub-wavelength scales, as they are not limited by diffraction losses, as is the case with conventional photonic devices. They are

also famous for their high-surface sensitivity, which is a prime reason for their appeal as mid-IR photonic devices. Not unlike silicon nanowires, slot waveguides allow the light to be confined to the low-index region, where it may interact with some analyte. It also “squeezes” the optical mode, which enhances the optical confinement, thus, improving the performance of on-chip applications in general. Hence, it is our main goal to design high-confinement, silicon-based plasmonic slot devices in the mid-IR, which may be used for plasmonic on-chip applications.

Conventional plasmonic devices are realized using conducting materials—typically, noble metals such as silver and gold. However, noble-metal-plasmonics can only guarantee high field confinement when operated near their plasma resonance, which lies in the visible and near-infrared (NIR) frequencies. When operated in the mid-IR, the plasmonic modes of noble metals tends to leak into the cladding, and hence, noble metals are not suited for mid-IR applications. Additionally, conventional plasmonic devices are not CMOS-compatible, and require non-standard fabrication techniques. This discourages any attempt to engineer noble metals to work efficiently in the mid-IR. Hence, we may rephrase our design goal to: mapping (and improving) the performance of highly confined plasmonics in the NIR to the mid-IR through the use of doped silicon.

In order to use silicon—a semiconductor—as a plasmonic medium, it is injected with dopants until it starts to behave as a metal. The doping concentration, which can be altered using well-known manufacturing techniques, is responsible for shifting the plasma resonance of the material to the mid-IR. Hence, the plasma resonance of the silicon can be tuned by adjusting the doping concentration. Operating doped silicon that has a plasma frequency in the mid-IR not only enhances confinement, but also shows the potential for being used in many novel applications. This was discovered by studying the dispersion relation of a finite-width doped silicon slot and an infinite-width doped silicon slot. The dispersion showed that our design has potential to work as a slow light medium, a negative-dispersion medium, an epsilon-near-zero (ENZ) medium, and a highly-sensitive plasmonic medium. Of these, the potential of using the waveguide as a slow light medium and as a sensor were investigated. In addition, the performance of typical plasmonic gap structures used in on-chip devices, such as 90 degree bends, and t- and x-junctions, were studied in the mid-IR. Aside from slot waveguides, other structures based on highly-doped silicon were investigated, namely the rectangular shell waveguide and nanoparticles; both structures show great potential for sensing applications.

Thus, the main message here is that silicon is highly flexible and can work efficiently as an optical waveguide in typical photonic settings, as well as plasmonic

settings, over a large bandwidth. Besides the obvious advantage of being CMOS-compatible, silicon has good electrical and mechanical properties, including low surface scattering losses and high mobility. Perhaps, the main limitation of our work is that our results are based on computer simulations, which do not take into account certain real-world problems, such as temperature fluctuations, and imperfections in material structure and dimensions.

The remainder of this dissertation is divided between the two aforementioned designs: SNRW photonic sensors and highly doped mid-IR plasmonic devices. In Chapter 2, the general optical (bio)sensing process is explained. Some of the most popular optical evanescent field sensing configurations are discussed; this includes the bimodal configuration, which is employed in our work. The theory of operation of novel waveguides, namely, slot waveguides and silicon nanowire waveguide is presented. Chapter 3 discusses our SNRW photonic sensors, in terms of their performance against other structures, and their sensitivity limit. The dimensions of our SNRW were chosen based on a study on the specific dimensions that allow single-mode operation, which is mandatory for the bimodal interferometer to function properly. Finally, the performance and sensitivity of the bimodal interferometer is studied.

Chapter 4 gives an overview on the basics of plasmonics, including the physics behind their operation, and their applications. The Drude model, which is used to model our doped silicon material, is discussed as well. Then, an overview on the applications in mid-IR regions is given. The confinement issue faced by conventional plasmonic devices in the mid-IR is explained; also, some of the efforts that address this issue are reviewed.

In Chapter 5, we present a comprehensive study on doped silicon plasmonics. First, we discuss how we modelled our doped silicon material for computational purposes; then, we discuss the effect of changing the doping concentration on the characteristics of silicon. We also show, through simulations, that doped silicon can propagate for long-distances in the mid-IR, whereas silver cannot. We then move on to studying the dispersion characteristics of doped silicon slot waveguide in the mid-IR. This is done for several dimensions, so as to provide a more comprehensive insight into the significance of certain architectural parameters. A similar study is performed for doped silicon rectangular shell waveguides. Some of the potential applications, such as sensing and slow light, are investigated and presented. The sensitivity of doped silicon nanoparticles is also explored. Finally, the ability of the waveguide to transmit light through sharp bends and junctions is demonstrated. A summary of our findings is presented in Chapter 6. Suggestions on how to improve upon this work are also presented.

# Chapter 2: Overview on Photonic Biosensors

The ideal on-chip diagnostic device integrates all processes from sample extraction to biosensing and detection to signal delivery. The dream of creating such a device was facilitated during the 1980s when several microfluidic structures, such as microvalves and micropumps, had been realized by silicon micromachining technologies. These structures provided a simple solution for guiding the sample across the chip [4]. This presented the dawn of the newly emerging field of “micro total analysis systems” ( $\mu$ TAS11), commonly referred to as “lab-on-a-chip” [5]. Biosensors are the main diagnostic component in the much sought-after lab-on-a-chip devices. A prerequisite to paving the way to on-chip detection is by designing highly sensitive and robust biosensors with label-free and real-time detection. The purpose of this chapter is to give insight into the general operation principles of biosensors, as well as review some of the most common optical sensor configurations.

## 2.1 What Is a Biosensor?

A biosensor is essentially a transducer that converts a biorecognition event into a measurable signal. A characteristic component exclusive to biosensors is the bioreceptor. The bioreceptor is typically an enzyme that is capable of recognizing and binding to a desired target molecule: the analyte. The bioreceptor may also be an antibody, an aptamer, a DNA probe, a protein or even a microorganism [6]. The choice of bioreceptor depends on the physical quantity (e.g. virus, cancerous cell, etc.) that needs to be detected. This eliminates the need to use expensive reagents that are typically required in traditional laboratories.

A critical process to creating a biosensor is the immobilization of bioreceptors. This process basically connects bioreceptors to transducers. If bioreceptors were just aimlessly floating around the vicinity of the transducers, their presence would not be very effective, and as a result, the transducer’s sensitivity would be greatly reduced. Thus, the purpose of the immobilization process is to attach the bioreceptors to a strategically chosen area in

the transducer. This area will be referred to as the “sensing surface” throughout this chapter.

Hence, the physical properties of the transducers will be altered by the reactions occurring at the newly introduced sensing surface. This physical change may be depicted in various means, such as a change in the interference pattern, resonant frequency or coupling angle, as will be seen in future sections. In addition, the transducer/sensor configuration will determine the type of electrical measurement used to interpret the physical change. Once a change is sensed it will be mapped to a certain “diagnosis.” These mappings are based on prior experimentations of the device. A summary of the sensing procedure and the immobilization taking place in the biosensor is generalized in Figure 2.1.

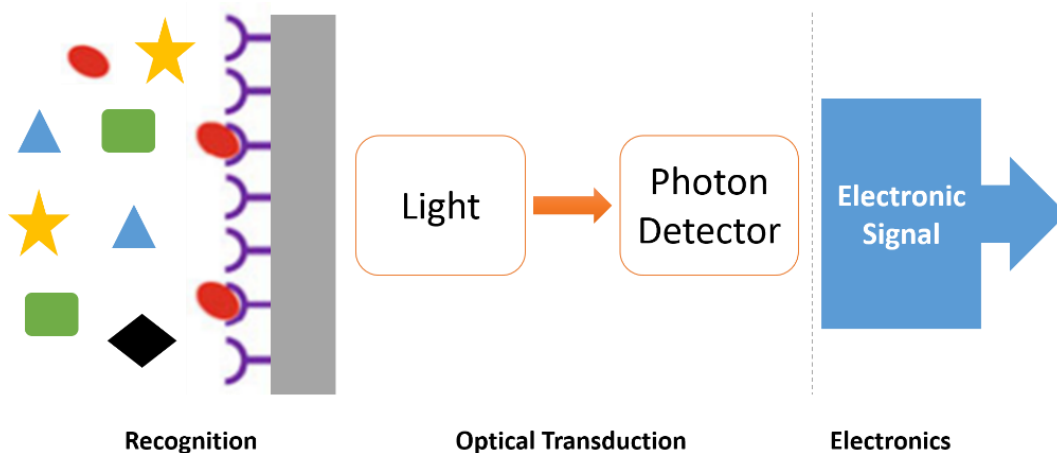


Figure 2.1. Simplified biosensor model

## 2.2 Brief Overview of Immobilization

This section is out of scope with our work but is provided nonetheless for the purpose of sketching a fuller picture of the biosensor operation. The choice of an appropriate immobilization procedure is a critical step in the biosensor design, and ought to be optimized according to the application. The immobilization process mandates an efficient coverage of the transducer surface with bioreceptors. However, a truly successful immobilization process is expected to minimize nonspecific adsorption, as well as preserve the original bioreceptor properties (e.g. biological activity, affinity, specificity, structure, etc.), ensure their stability for storage and regeneration, and have a short response time.

Additionally, the resolution and selectivity of any biosensor device is limited by the effectiveness of the bioreceptor layer.

Among the immobilization strategies available are affinity, cross-linking, adsorption by deposition, covalence and entrapment. Figure 2.2 [7] depicts some of the several means that can be used to biofunctionalize the sensor surface: (1) chemical activation of plain surface, (2) bioreceptor immobilization (3) and final detection of the target molecule (4). The bioassays in (3) and (4) are: (a) Mixed self-assembled monolayer (SAM) with reactive and non-reactive silanes compounds with specific antibodies covalently immobilized for protein recognition; (b) hydrophilic and biocompatible reactive monolayer based on pegylated-silane or dextran compounds with proteins covalently immobilized for antibody recognition; (c) Affinity tags immobilized on the surface to achieve appropriate orientation of specific antibodies for protein recognition; (d) covalent immobilization of DNA or RNA probes for hybridization with complementary DNA/RNA strands.

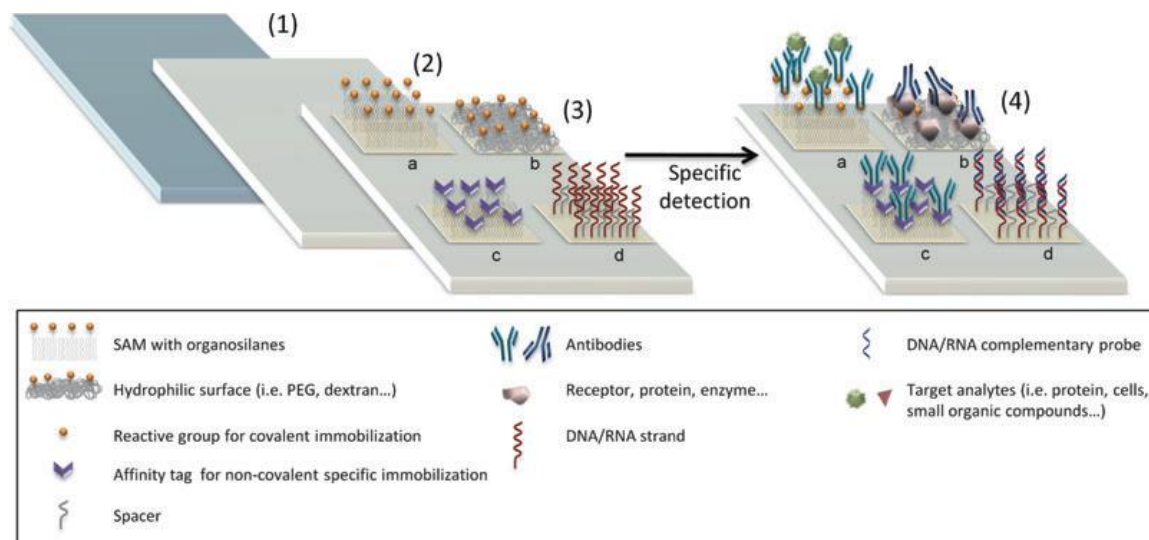


Figure 2.2. Common surface biofunctionalization strategies (adopted from [7])

Possibly the simplest immobilization strategy, physical adsorption is based on the deposition of the bioreceptor onto the transducer surface. The deposition occurs as a result of the hydrophobic and electrostatic interactions between the bioreceptor and the surface. However, this method suffers from weak bondage, which can lead to the easy desorption of the active receptors under flow conditions. In addition, the application of regeneration cocktails—chemicals responsible for breaking the interaction event—can also result in



desorption. Moreover, in this scheme, the folding of the bioreceptors onto the surface (e.g. orientation of bioreceptor with respect to the surface, which consequently affects the bind event) is not controllable. This makes physical adsorption generally a poor candidate for immobilization.

In covalent binding, biomolecules are bound to the surface through the functional groups that they contain, and whose blocking will not greatly affect the biomolecule's catalytic activity. First, the surface is activated using multifunctional reagents, then the biomolecule is coupled to the activated surface, afterwards, the excess biomolecules are removed. This process can occur on the transducer surface, or on a thin membrane fixed on the transducer. As an example, proteins couple well to amino or carboxylic or thiol groups. On the other hand, for the immobilization of nucleic acids, DNA synthesis is used to combine reactive groups at the end of the sequence.

Affinity binding involves orientation-controlled attachment of biomolecules; this prevents enzyme deactivation and ensures that the binding sites remain free. This can be achieved through the use affinity proteins, such as A or G Protein, or through the use of carbohydrate residue. Another popular approach is based on the biotin and (strept) avidin systems, where avidin is sandwiched between biotin and biotinylated bioreceptor [7].

## 2.3 Photonic Biosensors

Optical transduction methods reveal themselves as the most promising candidates for biosensing, providing the highest sensitivity. These devices also have the advantage of being label-free, meaning they do not require fluorescent tags. Traditionally, biosensors require a label attached to the target; this label is detected during readout. Labels can be fluorophores, magnetic beads, or active enzymes. However, labeling comes with a byproduct: the binding properties of a biomolecule may go under sever change, and the yield of the target-label coupling reaction is highly variable [8]. Thus, label-free sensing methods are encouraged and sought after.

Optical sensors typically consist of a waveguide that has a refractive index higher than the surrounding environment, so that it can achieve optical power confinement. Conventionally, the sensing surface is located at the evanescent field. In this scenario, most of the light is confined inside the waveguide (typically made of silicon), while the "tail" of the light can remain on the outer edges of the waveguide, provided that the waveguide is small enough. Hence, the bioreceptors are typically arranged on the edges of the waveguide where they can interact with the evanescent field. The induced physical change

that occurs due to the biological event is represented as a change in the effective refractive index. Such a change can be measured using many configurations such as resonators and gratings, but some claim [9], [10] that the winning technique is provided by interferometric devices. The following section contains a brief overview of some of the most popular sensing configurations that are based on evanescent field detection. In these cases, the width is designed to be small enough in order to allow the evanescent tail of the light to leak out of the waveguide. The bioreceptors are placed right outside the waveguide, in order to interact with the evanescent tail.

## 2.3.1 Evanescent Field Sensors

### 2.3.1.1 Mach-Zehnder Interferometers (MZI)

Perhaps the most common configuration for interferometric waveguides is the MZI [11]-[14]. A typical optical integrated MZI sensor consists of an optical waveguide fabricated on top of a silicon substrate. The waveguide splits into a reference arm and a sensing arm, as shown in Figure 2.3. The reference arm is covered, while the sensing arms is exposed to the microfluidic channel, which lies on top of the MZI. The bioreceptors are placed on the sensing arm; thus, when the sample is injected, the overall effective index of the sensing arm is altered, causing some delay in the electromagnetic field travelling through the arm. The two arms are coupled into an output rib waveguide, where the overall interference pattern is altered by the delay in the sensing arm. The dimensions of the optical waveguides must ensure single-mode behavior and high surface sensitivity. Single-mode operation is a must because light propagates at different velocities for different modes. Therefore, if multiple modes are propagating, each with a unique sensitivity, they will interfere with each other, resulting in a decrease in the output signal. During the read-out, the output intensity is detected and refractive index change is transformed into a phase shift. The output light intensity,  $I$ , and output phase shift,  $\Delta\varphi$ , are given by:

$$I = \frac{I_0}{2} [E_S^2 + E_R^2 + 2E_S E_R \cos \Delta\varphi] \quad (2.1)$$

$$\Delta\varphi = 2\pi \frac{L}{\lambda} (n_{eff}^S - n_{eff}^R) \quad (2.2)$$

where  $I_0$  is the input light intensity,  $L$  is the length of the sensor area,  $\lambda$  the wavelength and  $E_S, E_R$  are the electric fields at the sensor and reference arms, respectively; similarly,  $n_{eff}^S, n_{eff}^R$  are the effective refractive indices produced in the sensor arm and reference arm, respectively [11]. It can be seen that the length of the sensor area is directly

proportional to the sensitivity of the MZI. One of the main drawbacks of this configuration is the cosine dependency, which basically means that sensitivity is dependent on the position of the interferometric curve, with maximum sensitivity at quadrature points. A modulation system that can track the interferometric read-out is a possible solution to such an issue [15].

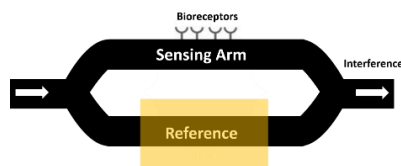


Figure 2.3. Top view of Mach-Zehnder sensor

### 2.3.1.2 Bimodal Waveguides

Distinct from the aforementioned MZI, bimodal waveguides do not require a reference arm. However, their principle of operation is very similar to MZI waveguides in that the sensing is done by inducing a change in the output interference pattern. These devices employ a single ridge waveguide that supports an interference mode. First, light in transverse electric polarization is coupled into a ridge waveguide, which is configured to support a single transversal mode. As illustrated by Figure 2.4, after a certain distance, the height of the ridge waveguide is altered so that it supports two modes—fundamental and first order modes; this causes a known interference pattern at the output. The sensing surface is integrated on the dual-mode part of the waveguide. When the refractive index changes due to the biorecognition events occurring at the surface, the intensity distribution of the interference pattern changes accordingly. Thus, in this case, the output of the bimodal waveguide with an air cladding can be thought of as the original interference pattern. The simplicity of this design is one of the main advantages; it can be easily fabricated as it does not require Y-junctions as the MZI. Furthermore, the compactness of the configurations can allow for the existence of parallel multiple sensing channels on a single chip [15], [16].

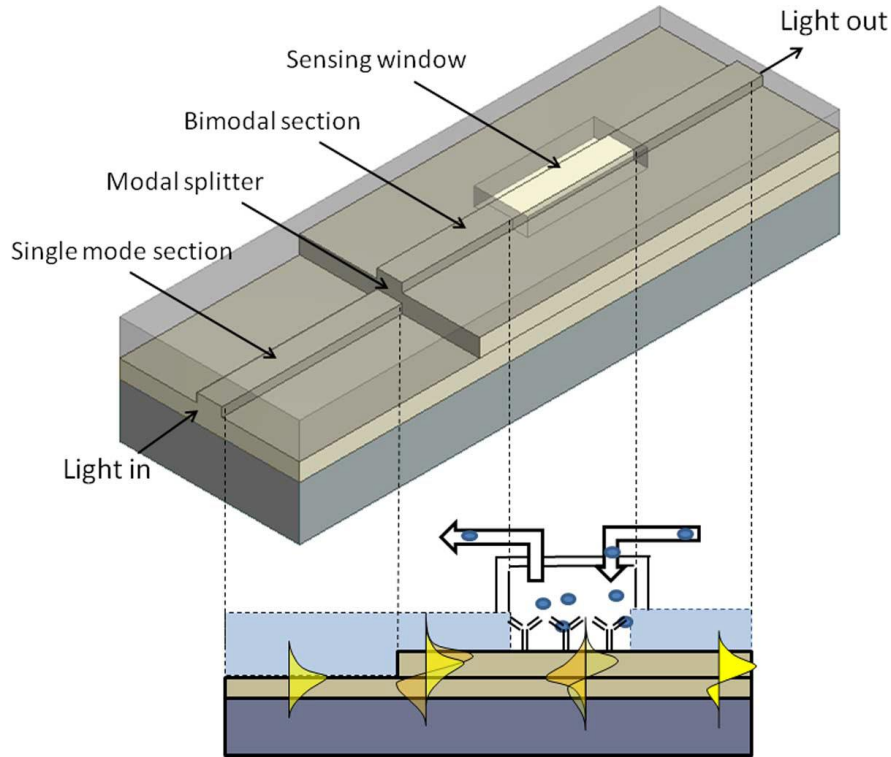


Figure 2.4. Structure of the bimodal waveguide (taken from [15])

### 2.3.1.3 Grating-Coupled Waveguide Sensors

Another class of waveguides are grating-coupled waveguide sensors [17], [18]. This is one of the older structures, and it basically consists of periodic disturbances, or gratings on a single-mode high-index layer fixed on a low-index substrate, as shown in Figure 2.5. The gratings produce multiple diffractions. One of those diffractions has the same momentum as the supported waveguide mode, and therefore can couple to that mode. The guided mode has a certain angle of incidence when the in-coupling condition is fulfilled [19]:

$$n_{eff} = n_{air} \sin \theta + l \left( \frac{\lambda}{\Lambda} \right) \quad (2.3)$$

where  $n_{eff}$  is the effective refractive index of the waveguide,  $n_{air}$  is the refractive index of air,  $\theta$  is the angle of incidence of the light,  $l$  is the diffraction order, and  $\Lambda$  is the grating period. Clearly, as the refractive index of the surroundings changes, the in-coupling angle changes accordingly. So in this scenario, the sensing is achieved by measuring the angle of incidence,  $\theta$ .

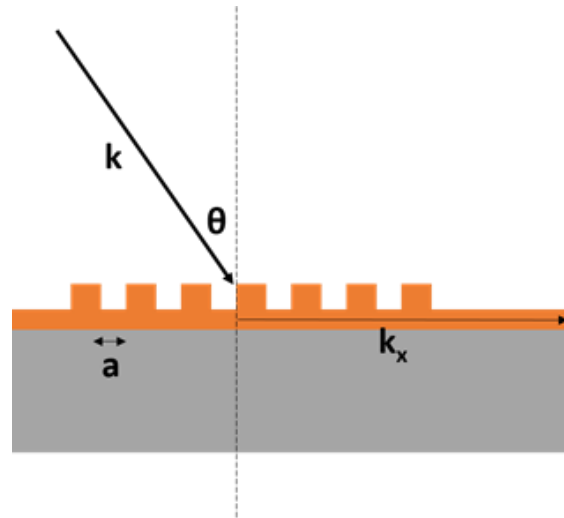


Figure 2.5. Grated optical waveguide

### 2.3.1.4 Ring Resonator Waveguide

One of the most popular optical sensing schemes is the ring resonator sensor [19]-[25], shown in Figure 2.6. It consists of a circular waveguide and a rib waveguide with identical properties (material, thickness, width, etc.). Light is coupled to the rib waveguide, which is placed in high proximity with the circular waveguide. After that, light is coupled to the circular waveguide via the evanescent field emanating from the rib waveguide. The evanescent field continues to feed the circular waveguide in a constructive interference pattern. The material under test is placed in the center of the waveguide and interacts with the evanescent field in the circular waveguide. Next, the output signal from the ring-resonator is measured. In this scenario, the effective refractive index change occurring due to the presence of the analyte on the ring's surface is translated to a change in the output resonant frequency of the ring, such that [24],

$$\lambda = 2 \pi n_{eff} r/m \quad (2.4)$$

where  $r$  is the radius of the ring. Obviously, in this case, the reading is done by measuring the shift in the new resonant frequency with respect to the default resonant frequency (air cladding). The default resonant frequency can be measured theoretically, and experimentally, before the introduction of the analyte.

One of the main advantages of ring resonators is that unlike the aforementioned biosensor configurations, the sensitivity is determined by the number of revolutions

performed by the light within the ring, rather than by the actual length. So one can say that the sensitivity depends on the effective length of the ring. This phenomenon is modeled as follows [24],

$$L_{eff} = Q\lambda/2\pi n_{eff} \quad (2.5)$$

where  $Q$  is the quality factor, and  $L_{eff}$  is the effective length equal to the circumference multiplied by the number of revolutions. However, a general disadvantage of ring-resonators is that they suffer from optical losses due to the continuous bending in their structure. This disadvantage becomes more and more pronounced as the radius of the ring is reduced, making ring resonators non-ideal candidates for miniaturization.

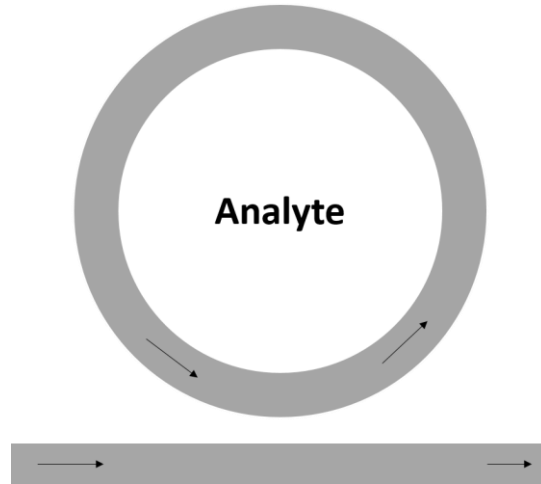


Figure 2.6. The ring resonator waveguide

### 2.3.2 Novel waveguides for biosensing applications

The previous configurations all relied upon evanescent field detection. Perhaps, the main disadvantage of this type of detection is that the majority of the light wave is buried within the bulk waveguide, and not contributing to the waveguide's sensitivity. In this section, we will discuss two recent photonic waveguides, namely the slot waveguide and the silicon nanowire optical waveguide, that allow the light to be confined in low-index regions, where the analyte may be inserted.

#### 2.3.2.1 Slot Waveguides

One of the more recent additions to the photonics industry are slot waveguides. This structure is able to guide light in the low refractive index region. This provides an amazing advantage in biosensing applications, as it presents the opportunity for the fluid

to be guided along with the full wave, rather than with the evanescent wave, thus improving the sensitivity. This waveguide, proposed by [26], consists of a nanometer-wide low-refractive-index,  $n_L$ , region, surrounded by two ribs of high-refractive-index regions,  $n_H$  (see Figure 2.7). According to Maxwell's theory, the continuity of the normal component of the electric flux density must be maintained through the sudden contrast between the high and low refractive index regions. This results in a strong discontinuity in the electric field, which consecutively results in a much higher field amplitude in the low-index region. Since the refractive index is proportional to the square of the permittivity, the ratio between the values of the normal electric field component at both sides of the wall is equal to the square of the index ratio across the wall. Because the dimensions of the slot are designed to be smaller than the decay length of the field, the electric field remains constricted in the high-index region. Unlike the previous sensing configurations, which relied on evanescent field detection, this unique waveguide can confine the field in the same area as the analyte, which greatly enhances the sensitivity.

Several sensing configurations have been based on the slot waveguide, and showed enhanced sensitivity, such as the slot ring-resonator sensor [27], [28], and the slot directional coupler [29]. Rather than using a single slot, Sun *et al.* [30] used multiple slots to enhance sensitivity. The combined slots act as a single medium to accommodate single-mode propagation. To convert the output of the slots to a measurable signal, three slots were arranged in a ring resonator configuration. The sensitivity was determined by measuring the slope of the output signal, which represented the phase shift against the refractive index change. A recent review on the biosensing configurations based on slot waveguide is presented in [31].

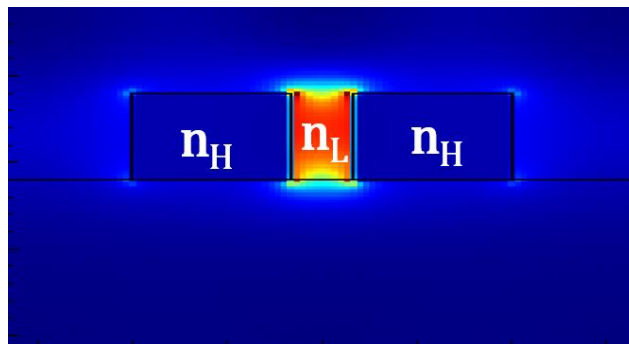


Figure 2.7. Modal profile of a slot waveguide

### 2.3.2.2 Arrays of Silicon Nanowire Optical Waveguides

Silicon Nanowire Optical Waveguides, or SNOWs, consist of a waveguide that is comprised of an array of silicon nanowires. In this configuration, the light guiding region is confined to the “effective” high-index region. In other words, since the silicon nanowires are placed in a high proximity, and have a diameter in the nanometer range, the light views them as a conventional bulk waveguide with an “effectively” higher index than the environment. When this structure is immersed in liquid, the effective refractive index change is much higher, due to the presence of voids within the structure, thus improving the sensitivity. A challenge in designing those structures is ensuring optical confinement, despite the presence of “voids” in the waveguide. Optical confinement can be enhanced if the effective index of the rib waveguide is higher than that of the surrounding. A simple way to approximate the effective index,  $n_{eff}$ , is by using the average index method given by [2]:

$$n_{eff} = \sqrt{\frac{n_{Si}^2 \times A_{Si} + n_{surround}^2 \times A_{surround}}{A_{Si} + A_{surround}}}, \quad (2.6)$$

where  $n_{Si}$  and  $n_{surround}$  are refractive index of silicon and surrounding medium respectively, and  $A_{Si}$  and  $A_{surround}$  represent the area of silicon and surrounding medium, respectively.

The height of the silicon nanowires plays a key role in confining light in the vertical direction. In addition, the refractive index difference between the silicon oxide layer and the substrate permits the transverse guidance of the optical signal. [2] demonstrated that for a single nanowire with a diameter below 100nm, the amplitude of the electric field within the nanowire is almost constant, and there is nearly zero distortion in the phase of the field. This implies that an array of nanowires with small diameters would be efficient in confining light. However, these desirable properties are only achieved when the electric field is polarized along the length of the nanowires.

SNOW has a great potential as a sensor because it provides a medium where the majority of the field can interact with the material being tested. Hence, the corresponding change mirrored in the effective refractive index would be enhanced. [32] illustrated this by creating a ring resonator sensor based on SNOW, where a conventional single-mode rib waveguide was used as a convenient coupling method to the nanowire-based ring resonator waveguide. The percentage change in the effective index of the SNOW based structure was shown to be about 4 times larger than that of the conventional bulk silicon based structure.



## 2.4 The FDTD Method

In order to characterize a sensor or any optical system numerically, some computational method is needed. The FDTD method is a well-established computational analysis technique for modelling electromagnetic systems. Commercial software that is based on the FDTD method is employed throughout this dissertation. Therefore, it is necessary to discuss this method briefly. This numerical method was first proposed by Yee in 1966 [33]. It is generally used to solve the time-dependent Maxwell curl equations. The FDTD method falls under the umbrella of finite difference (FD) methods, which are methods that approximate the solution to differential equations. In FD methods, the differential equation is described using Taylor's expansion. The simulation area is divided into a grid. In the case of a 1D problem, the simulation area can be envisioned as a line that is divided by a number of points; the spacing between each point is  $h$ . For instance, a simple 1D problem could have a differential equation in the form of  $f'(x) = 3x$ . This equation can be rewritten as  $f'(x) = (f(x+h) - f(x))/h$ , where  $h$  is the step size. By manipulating the equation algebraically, an approximate solution to the differential equation can be reached.

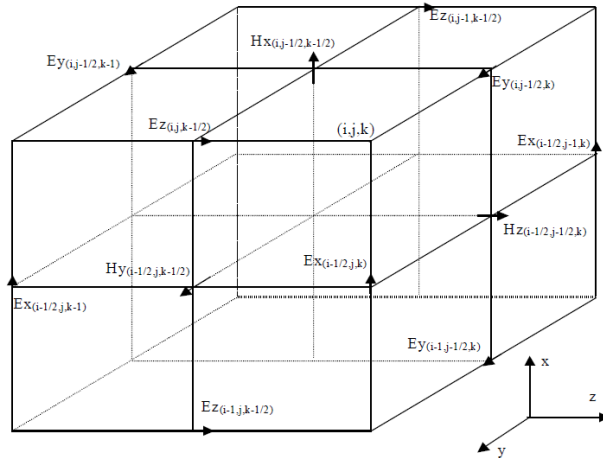


Figure 2.8. Displacement of the electric and magnetic field vector components in a cubic unit cell of the Yee space lattice.

To elaborate, consider a typical 3D computational domain. Figure 2.8 shows the electric field and magnetic field components in a 3D space, which is also known as the Yee grid. The Maxwell curl equations can be broken up to six equations. One of those equations is written as,

$$\frac{\partial E_z}{\partial y} - \frac{\partial E_y}{\partial z} = -\mu \frac{\partial H_x}{\partial t} \quad (2.7)$$

Equation (2.7) may be discretized using FD method as follows,

$$\frac{\partial E_z}{\partial y} = \frac{E_z^n(i, j + 1/2, k) - E_z^n(i, j - 1/2, k)}{\Delta y} \quad (2.8a)$$

$$\frac{\partial E_y}{\partial z} = \frac{E_y^n(i, j, k + 1/2) - E_y^n(i, j, k - 1/2)}{\Delta z} \quad (2.8b)$$

$$\frac{\partial H_x}{\partial t} = \frac{H_x^{n+1/2}(i, j, k) - H_x^{n-1/2}(i, j, k)}{\Delta t} \quad (2.8c)$$

where  $n$  is the time-step, and  $i, j$  and  $k$  are the space steps in the  $x, y$  and  $z$  directions, respectively. The remaining five equations are discretized in a similar manner. Next, the discretized form is substituted into Maxwell's equations and solved [34]. As can be deduced from observing the above equations, the step size in space should be small enough so as to take structural changes into account. Also, the time step must be small enough in order to ensure computational stability [35].

# Chapter 3: Bimodal Optical Biosensor Based on Silicon Nanowire Ridge Waveguide

In this chapter, we propose a novel ultra-sensitive waveguide. Our main goals is to design a waveguide that is: a) highly sensitive to changes in the surrounding environment. b) impervious to temperature changes. c) easy to fabricate. d) compact. e) eligible for integration with microfluidics and electronics. Our waveguide is based on silicon nanowires, as they have the inherent ability of improving the sensitivity as they introduce voids to the otherwise bulky structure, as discussed in the previous chapter. Unlike the rib-shaped nanowire structure proposed by [2], our nanowires are arranged in ridge-shaped envelope, which has several advantages over the rib-shaped envelope in terms of design flexibility, performance and manufacturability, as will be discussed in this chapter. We shall refer to our ridge-shaped nanowire waveguide as silicon nanowire ridge waveguide, or more simply as SNRW. The inherent sensitivity provided by the SNRW make it eligible for label-free sensing. The performance of SNRW is characterized by modal and FDTD simulations. Also, to highlight the distinctiveness of the SNRW, it is compared to evanescent and non-evanescent field sensors. But in order to truly evaluate the SNRW as a sensor, we needed to use it as a building block in a sensing configuration. The sensing configuration we chose to use is the bimodal configuration. That choice was made primarily due to the compactness and simplicity of the bimodal interferometer, and other details that will be discussed in this chapter.

## 3.1 Silicon Nanowire Ridge Waveguide (SNRW)

The proposed SNRW is a waveguide that is comprised of an array of silicon nanowires on an insulator substrate. The basic principle of operation is as follows: when a sample is injected into the biosensor, the voids within the SNRW adopt the refractive index of the newly introduced analyte. Hence, the strong contribution of the analyte to the overall effective index will greatly enhance the sensitivity—this is where the significance of the nanowires to the sensing process lies.

On the other hand, the ridge shape is characterized by having a higher-thickness region at the center of the waveguide. This structure is particularly useful for a multitude of reasons. For starters, single-mode operation is mandatory for several sensing configurations, as is the case for the MZI, the ring-resonator, and the bimodal waveguide. Since the number of modes in the ridge waveguide is mainly decided by the dimensions of the central high-thickness region, the dimensions of the lower-thickness region are designed in a very flexible manner. For instance, they can be extended over the entire substrate, while still allowing the SNRW to single-mode operation. This design flexibility offers another advantage: large dimensions are usually considered a fabrication convenience as they do not require extensive fabrication techniques. Also, because the manufacture of nanowires typically relies on etching, the substrate is always in danger of being eroded. Hence, the design of nanowires that fully cover the substrate is desired. Besides the design flexibility and the fabrication convenience, the larger size the SNRW offers a third advantage that has to do with performance. The larger physical dimensions induce a larger optical mode, which in turn magnifies the area where the light and analyte interact, thus, improving the sensitivity. Moreover, the presence of the low-thickness region in the SNRW ensures that no evanescent-tail is being leaked, and thus, safeguards a more efficient use of the light power.

## 3.2 Design Consideration for the SNRW

The proposed structure is shown in Figure 3.1. The silicon nanowires are placed on top of a silicon dioxide ( $\text{SiO}_2$ ) substrate. The nanowire diameter and pitch were chosen to be 100nm. This diameter is small enough to guarantee optical confinement, but still large enough to avoid resorting to expensive manufacturing techniques such as e-beam lithography. The width of the lower-thickness region of the SNRW was chosen to be  $10\mu\text{m}$  with a thickness of  $1\mu\text{m}$ . These dimensions are large enough to facilitate the manufacturing process, and allow for design flexibility.

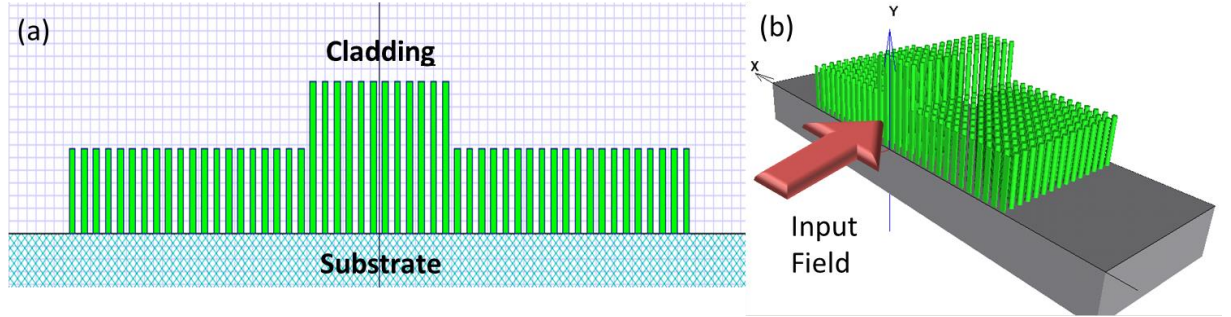


Figure 3.1. The SNRW structure. The nanowires are arranged in a ridge shape and placed on top of a silicon dioxide substrate. (a) Front view. (b) 3D view.

The rib height,  $h$ , and rib width,  $w$ , of the higher-thickness region, seen in Figure 3.2(a), had to be chosen carefully to ensure single-mode operation, and to qualify as the main building element in the bimodal waveguide. For this reason, using Optiwave software, 2D modal simulations were conducted on the SNRW in order to discover the thickness/width combinations that allow for single-mode operation. The simulation window was  $15\mu\text{m}$  wide, and had a  $5\mu\text{m}$ -thick cladding and a  $3\mu\text{m}$ -thick substrate layer. The cladding was assumed to be air. The waveguide was excited at the optical transmission frequency at  $1.55\mu\text{m}$ . At this frequency, silicon has a 3.45 refractive index, and  $\text{SiO}_2$  has a 1.45 refractive index [36]. As [2] mentioned in their work, only the modes along the length of the nanowires (y-polarized modes) can propagate. For this reason, only y-polarized modes were excited. A 2D map, shown in Figure 3.2(b), shows a single-mode (shading) region and a multi-mode region (white background) for rib heights ranging from 0.5 to  $1\mu\text{m}$ , and rib widths ranging from 0 to  $3.5\mu\text{m}$ . Since the silicon nanowires create a lower effective-index-region than the bulk silicon, they contrast less with the surrounding refractive index. This causes them to permit single-mode (see Figure 3.2(c)) operation for larger dimensions than bulk silicon. For instance, according to our simulations, the bulk silicon ridge waveguide cannot support single-mode operation for rib dimensions as small as  $1.5 \times 1.8\mu\text{m}$  (expressed in  $w \times h$  format). Conversely, the SNRW can support single-mode operations for dimensions as large as  $3.25 \times 1.8\mu\text{m}$ . This dimension flexibility provided by the SNRW is an extra-advantage that could facilitate the fabrication process. By reexamining Figure 3.2(b), it is clear that the SNRW fails as a single-mode waveguide in two scenarios: a) when the height is too small that the entire waveguide is effectively seen as a wide rib nanowire waveguide. In this case, the first-order mode splits into two adjacent fields, as shown in Figure 3.2(d). b) When the height is too large; in this case, the first-order mode splits vertically rather than horizontally, as shown in Figure 3.2(e). So, before we return to our initial objective in this sub-section, which is designing the rib dimensions for single-mode operation, we need to contemplate future design considerations. First, we

intend to use the SNRW as a building block for the bimodal interferometer, which uses a single-mode section, and a higher-thickness dual-mode section that produces vertically-split modes such as the one shown in Figure 3.2(e). Therefore, we need to choose dimensions that can be easily elongated to support dual-mode operation. A second consideration is the fabrication convenience; since smaller dimensions usually rely on more complex and expensive fabrication technologies, we will choose the largest dimensions that allow for single-mode operation. A third and final design consideration is acknowledging that this 2D map is only applicable for vacuum surroundings. Once the SNRW starts to function as a sensor, it is possible for it to interact with materials with large refractive indices. This will reduce the contrast between the silicon nanowires and the cladding, which in turn will shrink the single-mode area in the 2D map. Therefore, it would be wise to choose dimensions that are not too close to the single/multi-mode interface in our map, so as to give further protection from potential violations against single-mode behavior that could occur due to the presence of high-index analytes. So as a trade-off between the second and third consideration, the rib width and rib height were chosen to be  $2\mu\text{m}$  and  $800\text{nm}$ , respectively.

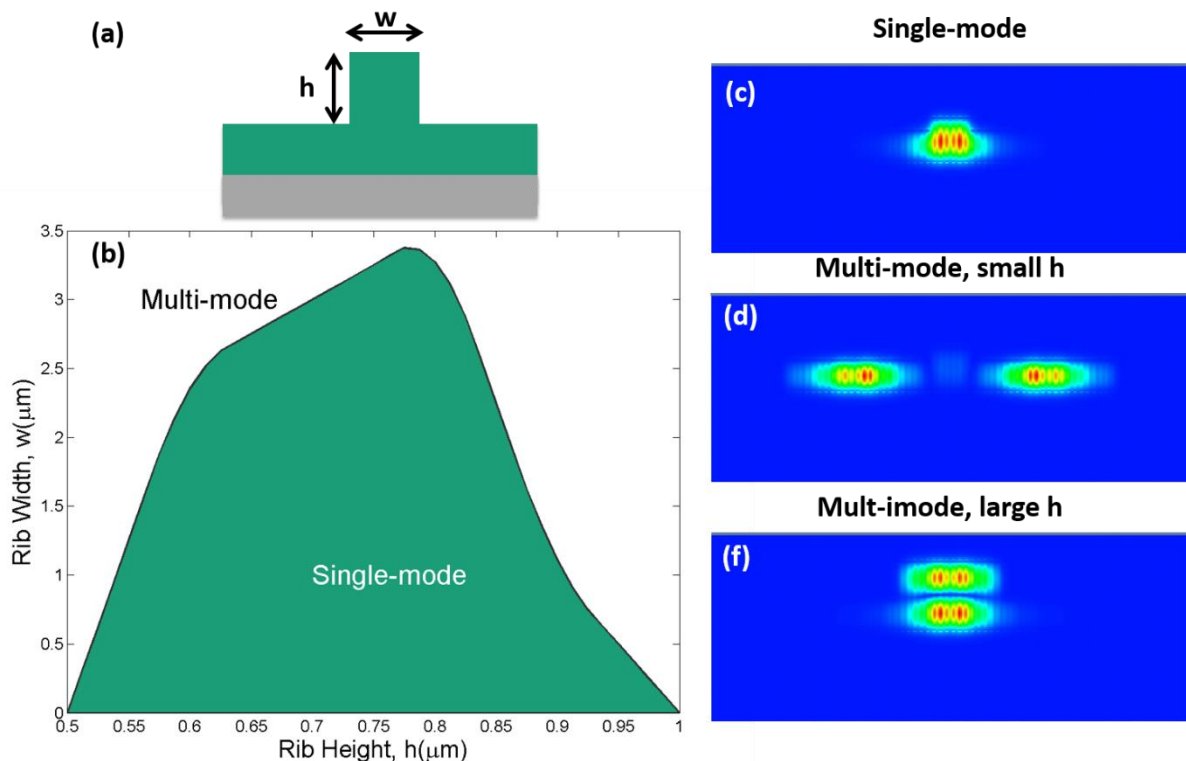


Figure 3.2. (a) Width,  $w$ , and height,  $h$ , of the rib (higher-thickness region in the ridge waveguide). (b) 2D map showing single-mode vs. multi-mode operation of various dimensions of the rib waveguide. (c) fundamental mode of single-mode SNRW. (d) first-order mode of SNRW with small height. (e) first-order mode of SNRW with large height.

### 3.3 The Relative Sensitivity of the SNRW

In order to test the viability of the proposed design, modal sensitivity simulations were performed. The response of the sensor was tested by measuring the induced effective index change when the refractive index of the cladding is varied from 1 to 1.6. The results were then compared to a typical bulk silicon ridge waveguide (BSRW). The dimensions of the BSRW were kept identical to those of the SNRW, and were found to maintain single-mode operation. Figure 3.3 shows the comparison between the two structures; the percentage effective-index-change is plotted against the change in the surrounding environment. The response of the SNRW to the change in the surrounding environment is around 170 times greater than that of the bulk silicon ridge.

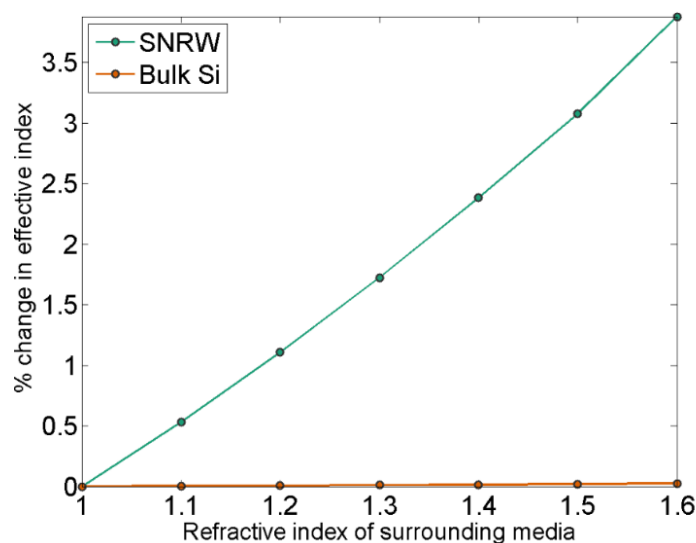


Figure 3.3. Percentage change of effective index for the SNRW and the BSRW as a response to the change in the surrounding environment.

The above results were expected as the BSRW has a very small portion of the evanescent field interacting with the environment. On the other hand, a good portion the optical mode created by the SNRW is overlapping with the surroundings. Perhaps, it is somewhat unfair to compare the SNRW with an evanescent-field sensor. So in another effort to demonstrate the value of the SNRW, we compare it to two similar non-evanescent-field sensor structures that are capable of guiding light in a low-index medium, along with the analyte. The first structure, shown in Figure 3.4(a), is a rib-shaped silicon nanowire waveguide, similar to the one proposed by [2]. We shall refer to this structure as ‘rib

nanowires.' Initially, the dimensions of the rib nanowires were exactly the same as the high-thickness region of our SNRW ( $2 \times 1.8\mu\text{m}$ ). However, this dimension did not allow single-mode operation. Hence, the width of the nanowire section needed to be reduced to  $1.75\mu\text{m}$ . The second structure, shown in Figure 3.4(b), is a silicon-on-insulator (SOI) waveguide with some gratings on top, which we will refer to as 'SOI gratings'. In order to maintain single-mode operation, the width of the gratings was designed to be equal to  $1.75\mu\text{m}$ , similar to the rib nanowires. The height of the waveguide, on the other hand, needed to be reduced, not only to guarantee single-mode operation, but also to allow some of the field to leak into the cladding. For this purpose, the new height was designed to be  $700\text{nm}$  ( $500\text{nm}$  for the bulk section and an additional  $200\text{nm}$  for the gratings). Needless to say, the diameter of the nanowires as well as the gap between them for both structures was maintained at  $100\text{nm}$  for fair comparison. Note that the SOI gratings is not meant to function as a grating coupler sensor [18], but simply as a light-guiding medium.

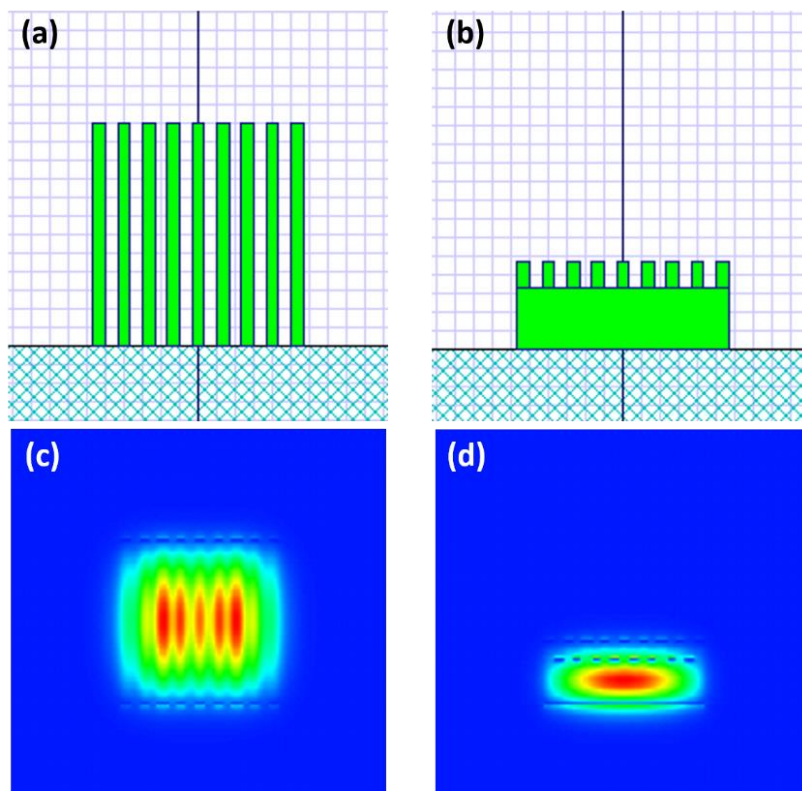


Figure 3.4. (a) Rib nanowire waveguide. (b) SOI grating waveguide. (c) optical mode for rib nanowires waveguide. (d) optical mode for SOI grating waveguide.

A simulation similar to the one conducted for the comparison between the BSRW and the SNRW was carried on; the results are shown in Figure 3.5. The SNRW is shown



to be far superior to the SOI gratings, with about 16 times as much sensitivity to changes in the surrounding environment. This performance could have been deduced from observing the SOI grating mode, shown in Figure 3.4(d). The majority of the mode is in the bulk, while only a small portion is present between the gratings, where it can interact better with the surrounding medium, or the “hypothetical” analyte. On the other hand, the rib nanowire waveguide shows a response to the refractive index change in the surrounding environment that is comparable to that of the SNRW, but just slightly smaller. However, that was to be expected as the mode shown in Figure 3.4(c), which depicts the rib nanowire mode, is also very comparable to the SNRW mode shown in Figure 3.2(c), except for the slight deformation in the SNRW mode caused by the ridge shape.

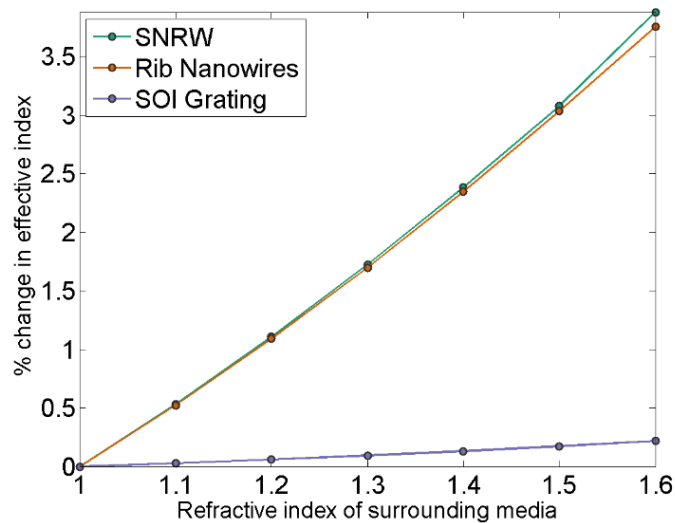


Figure 3.5. Percentage change in effective index for a refractive index change of the surrounding-environment for SNRW, rib nanowires, and SOI gratings.

In order to test the detection limits of the SNRW, very small refractive index changes were introduced to the surrounding environment, ranging from  $10^{-9}$  to  $10^{-1}$ . Figure 3.6 shows the percentage effective index change corresponding to minute refractive index changes in the surrounding environment. It is evident that the percentage effective index change is one order higher than that of the corresponding refractive index change in the surrounding environment (e.g. for  $10^{-6}$  change in the environment, there is a percentage effective index change in the order of  $10^{-5}$ ). The smallest detectable change occurs for a  $10^{-8}$  change in the surrounding medium.

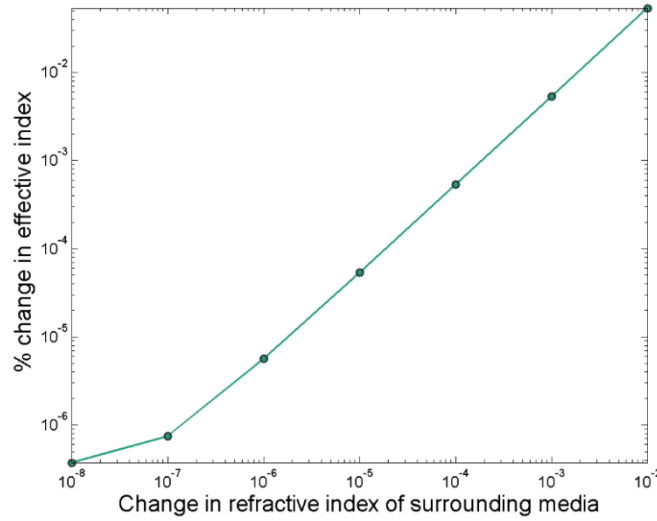


Figure 3.6. Percentage change of effective index for the SNRW as a response to minute changes in the surrounding environment.

### 3.4 Bimodal Interferometric Waveguide based on SNRW

In this section, we test our design using the bimodal sensing configuration, similar to the one proposed in [15]. The main appeal for this waveguide is its simplicity. It does not require  $y$ -junctions, or bends of any sort, as do popular sensing configurations, such as the MZI and the ring-resonator. These elements may introduce unnecessary manufacturing challenges, as well as optical bending losses. In general, resonance based sensors, such as the ring-resonator, are highly sensitive to fabrication imperfections, as well as temperature fluctuations due to the nature of the resonance effect itself. They also require some kind of temperature compensation mechanism to function properly [25]. On the other hand, interferometric devices are known to be less sensitive to such variations, which makes them more suitable for sensing application. While the output intensity of the bimodal waveguide is sensitive to temperature changes, its interference pattern does not depend on the intensity. This makes it superior to other interferometric devices, such as the MZI, which can produce false positives due to temperature fluctuations [14]. Also, the compact nature of this waveguide make it eligible for use as an on-chip sensor. It may be cascaded in order to allow the use of multiple sensing channels on a single chip, or to enhance the sensitivity—a feature not present in other popular sensing configurations.

The SNRW-based bimodal interferometer is designed as follows: the single-mode section feature the same SNRW dimensions described in Section 3.2. However, the width

of the lower-thickness region was reduced from  $10\mu\text{m}$  to  $6\mu\text{m}$  in order to allow the waveguide to be more compact. As for the dual-mode section, the rib height was increased from  $0.8\mu\text{m}$  to  $1.5\mu\text{m}$  in order to allow the fundamental and the vertically-split first-order mode to co-exist. A modal simulation was conducted for the dual-mode section to verify the presence of these modes. The results are shown in Figure 3.7(a) and Figure 3.7(b), which show the fundamental and first-order mode, respectively. The length of both the single and dual-mode sections was chosen to be  $5\mu\text{m}$ . To clarify the vision of the structure, the SNRW bimodal interferometer is shown in Figure 3.8.

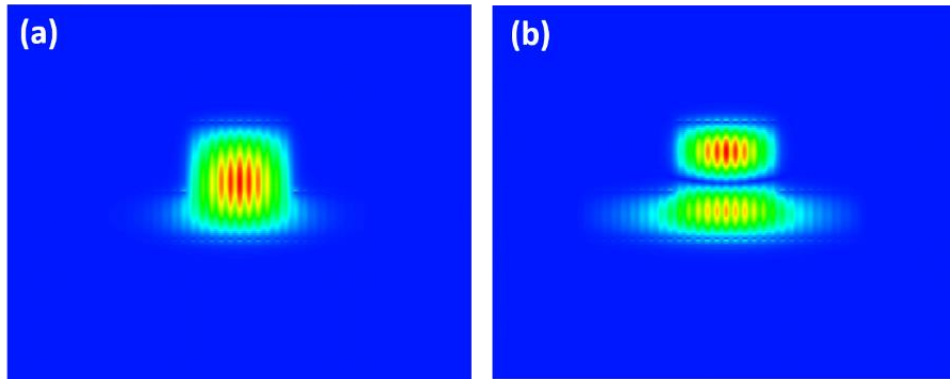


Figure 3.7. (a) Fundamental mode and (b) first-order mode of dual-mode section in the SNRW bimodal configuration.

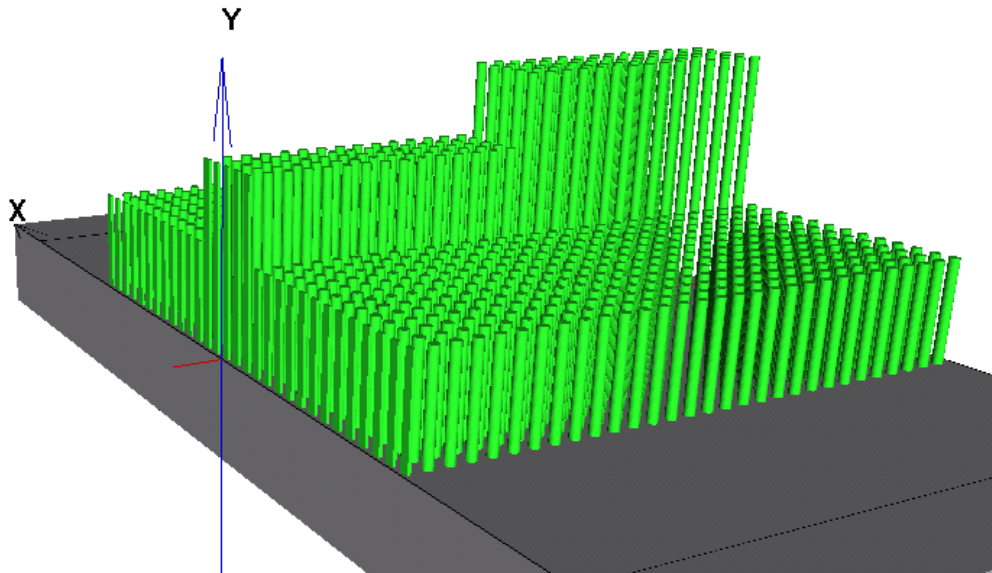


Figure 3.8. 3D SNRW bimodal waveguide.

3D FDTD simulations were conducted to test the performance of the SNRW as a sensor. The cladding thickness was  $5\mu\text{m}$ , while the substrate ( $\text{SiO}_2$ ) thickness was  $3\mu\text{m}$ . The width of the nanowire section was  $6\mu\text{m}$ . PML boundaries were invoked to minimize reflections from the boundaries. A mesh of  $0.02\mu\text{m}$  was applied to the x and z directions. A mesh of 0.4 was applied to the y-direction. Two monitors were employed: one XZ monitor to observe the propagation, and one XY monitor at the output to observe the transmitted power spectrum. The simulation time was 8000 time steps with a time step of about  $10^{-7}$ . In order to test the sensitivity, it was assumed that the analyte is filling the entire cladding. The refractive index of the cladding was varied from 1 to 1.6 with a 0.1 resolution—similar to what we did in the modal simulations. The spectrum of the normalized transmitted power for each cladding is shown in Figure 3.10. The propagation profile of the real part of the y-polarized electric-field component,  $E_y$ , in the z-direction is shown in Figure 3.9.

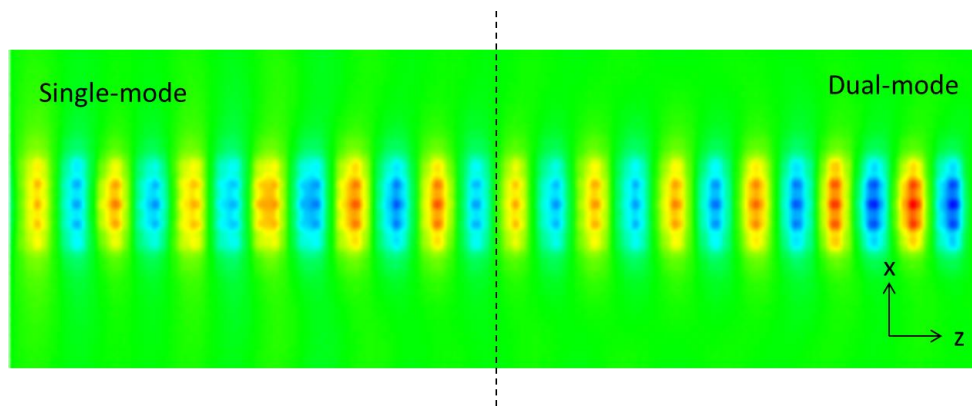


Figure 3.9. Propagation profile of the y-component of the electric field through a  $10\mu\text{m}$ -long SNRW bimodal sensor (top view)

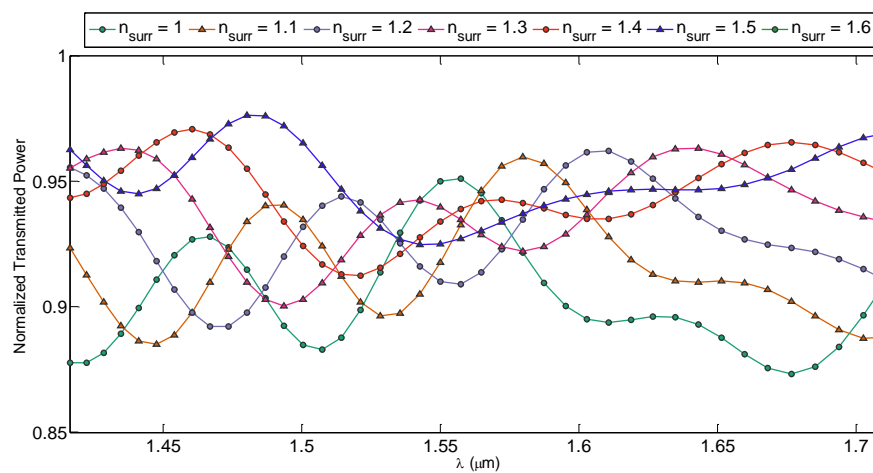


Figure 3.10. Normalized transmitted power spectrum for different refractive index surroundings ( $n_{\text{surr}}$ ) with rib width =  $2\mu\text{m}$ .

As can be seen from Figure 3.9, the optical signal is confined to the center of the SNRW for the 10 $\mu\text{m}$ -length of the bimodal waveguide. Figure 3.10 shows that for a 0.1 refractive index change in the surrounding medium, the normalized transmission power spectrum is red-shifted about 30nm. If we define the sensitivity as a the ratio between the spectral shift of the normalized transmission and the refractive index change, then the SNRW bimodal sensor would give an average sensitivity of 250nm/RIU. This is a remarkable sensitivity considering the small footprint of the device (6 x 10 $\mu\text{m}$ ). Previously reported sensitivities based on structures that allow light-confinement in the low-index region include a slot-based ring-resonator sensor with a 298nm/RIU sensitivity and a 10 x 13 $\mu\text{m}$  footprint [28], and a silicon-nanowire ring-resonator with a sensitivity of 335nm/RIU and a footprint of approximately 10 x 10 $\mu\text{m}$  [32]. Hence, if we define a sensitivity-to-footprint ratio (SFR) as a performance factor for optical sensors, the SNRW bimodal sensor would have the highest SFR at 4.167/mmRIU, whereas the silicon-nanowire and the slot ring-resonators would have a much smaller SFR at 3.35/mmRIU and 2.29/mmRIU, respectively. So ultimately, even though the SNRW employs a larger size as a single-element, once it is integrated with the bimodal waveguide, the entire configuration is relatively small. We attempted to slightly reduce the SNRW rib width from 2 $\mu\text{m}$  to 1.5 $\mu\text{m}$ . The idea is to allow the mode to be squeezed in more tightly, which would cause the electric fields to intensify and react more strongly to changes in the surrounding environment. By observing the transmission power spectra in Figure 3.11, the average sensitivity is increased to 300nm/RIU for the same (6 x 10 $\mu\text{m}$ ) footprint; this boosts the SFR to 5/mmRIU. Furthermore, the performance of ring-resonator-based structures in [28], [32] are limited by temperature fluctuations that can cause them to produce false positives, and may require a thermo-electric cooler to function properly [37].

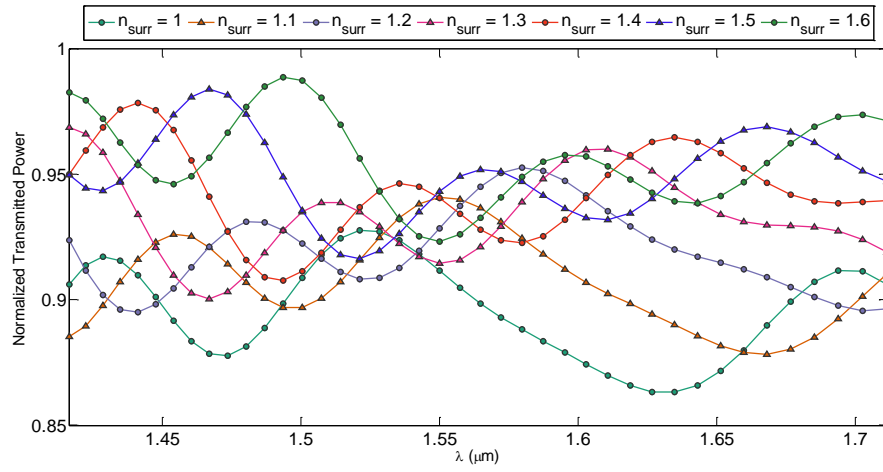


Figure 3.11. Normalized transmitted power spectrum for different refractive index surroundings ( $n_{\text{surr}}$ ) with rib width =  $1.5 \mu\text{m}$ .

# Chapter 4: Overview on Mid-Infrared Plasmonics

## 4.1 Plasmonics

Optical devices are popular in several everyday applications such as optical communications, and field-specific applications such optical tomography; the impact and potential of photonic applications is unquestionably wide and varied. However, this potential is limited by the laws of diffraction, which make it impossible for light to be confined within structures that have dimensions that are smaller than the wavelength of the incident light. These structures are otherwise known as “subwavelength structures.” Manipulating light on a subwavelength scale can yet be achieved by using a subwavelength structure that has a plasma resonance close to that of the incoming light. Hence, the photons would couple to the free-electron plasma in the material, creating subwavelength confinement. This is easily achieved using conductive materials, most notably, noble metals. This behavior is often simply referred to as “plasmonics.”

### 4.1.1 Surface Plasmon Polaritons

When an electromagnetic field shines upon a material occupying the negative half-space ( $z < 0$ ) that possesses a dielectric constant,  $\epsilon_m$ , with the opposite sign of the surrounding media,  $\epsilon_d$ , occupying the positive half space ( $z > 0$ ) (e.g. a metal with a dielectric surrounding), the free carriers within that material start to oscillate near the surface, forming a longitudinal wave. The cloud of electrons that get excited from the incident wave can be thought of as “plasmons”—in reference to electron plasma. The fact that the electron wave is confined to the surface, inspired the term, “surface plasmons.” The charges on this cloud are alternating at the metal/dielectric interface, as illustrated by Figure 4.1 (a); this polarization of charges inspired the name “polaritons.” Hence, to put it simply, “surface plasmon polaritons,” or SPPs, are oscillating charges that are localized at the metal/dielectric interface. The electromagnetic field associated with the electron wave has a maximum concentration at the interface and decays evanescently into the surrounding media, as shown in Figure 4.1 (b).

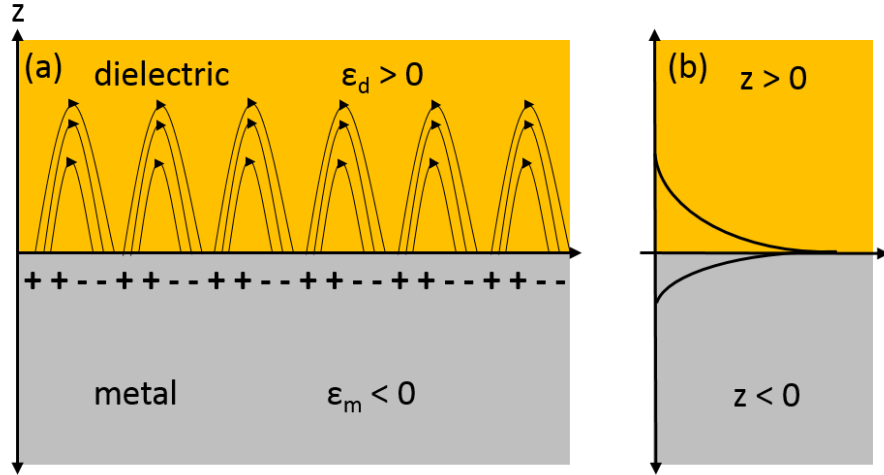


Figure 4.1. (a) Propagation of surface plasmon polaritons on a metal/dielectric interface, illustrating the electric field lines and charge polarization on the surface. (b) Modal profile of surface plasmons.

Since metal is a highly lossy material in nature, the SPP wave tends to decay rapidly within the metal while becoming more prominent in the dielectric. In order for SPPs to propagate, the resonance condition must be satisfied; this condition entails that the frequency of the incident wave be equal to the natural frequency of the electrons. It is instructive to look at the modal properties of this plasmonic wave to better understand its characteristics. This mode is a TM mode that can be obtained by solving Maxwell's equations and is described by the following electric and magnetic field components,

$$\text{for } z > 0 \begin{cases} E_z(z) = -A_1 \frac{\beta}{\omega \epsilon_0 \epsilon_d} e^{i\beta x} e^{-k_{2,z} z} \\ H_y(z) = A_2 e^{i\beta x} e^{-k_{2,z} z} \end{cases} \quad (4.1a)$$

$$\text{for } z < 0 \begin{cases} E_z(z) = -A_1 \frac{\beta}{\omega \epsilon_0 \epsilon_m} e^{i\beta x} e^{k_{1,z} z} \\ H_y(z) = A_1 e^{i\beta x} e^{k_{1,z} z} \end{cases} \quad (4.1b)$$

where  $k_{i,z}$  (where  $i = 1, 2, 3, \dots$ ) is the wavevector component perpendicular to the metal/dielectric interface,  $\omega$  is the angular frequency, and  $\beta$  is the propagation constant, which is the wavevector component in the direction of propagation. Maxwell's boundary conditions dictate that  $H_y(z)$  and  $\epsilon_i E_z(z)$  be continuous along the  $z$  direction, this yields the relations,

$$A_1 = A_2 \quad (4.2a)$$



$$\frac{k_2}{k_1} = -\frac{\varepsilon_m}{\varepsilon_d} \quad (4.2b)$$

In order for the TM mode wave equation ( $\frac{\partial^2 H_y}{\partial z^2} + (k_0^2 \varepsilon - \beta^2) H_y = 0$ , where  $k_0$  is free-space wavevector and is defined as  $k_0 = \frac{2\pi}{\lambda} = \frac{\omega}{c}$ , where  $\lambda$  is the wavelength and  $c$  is the speed of light) to be fulfilled, the wavevectors must yield,

$$k_1^2 = \beta^2 - k_0^2 \varepsilon_d \quad (4.3a)$$

$$k_2^2 = \beta^2 - k_0^2 \varepsilon_m \quad (4.3b)$$

By substituting (4.3a) and (4.3b) into (4.2b), we arrive at the expression for the propagation constant:

$$\beta = k_0 \sqrt{\frac{\varepsilon_d \varepsilon_m}{\varepsilon_d + \varepsilon_m}} \quad (4.4)$$

The above relation describes the dispersive property of single-interface propagating SPPs.  $\beta$  must be positive for the mode to propagate; therefore, it can be deduced that since the nature of metals mandates that  $\varepsilon_m < 0$ , the plasmonic mode will survive only if  $\varepsilon_d < |\varepsilon_m|$ . Also, equation (4.4) notes that the dispersion is maximized when  $\varepsilon_m = -\varepsilon_d$ ; this denotes the location of the plasma resonance [38].

### 4.1.2 Drude Model

The Drude model is an established way to describe the interaction between the light and the metal quantitatively. First, we start by describing the motion of free electron plasma excited by an electric field,  $E$ , using the motion equation,

$$m \frac{d^2 x}{dt^2} + m\gamma \frac{dx}{dt} = -qE, \quad (4.1)$$

where  $q$  is the electron charge,  $m$  is the optical effective mass of the electrons, and  $\gamma$  is the collision frequency which describes the damping that occurs due to the oscillations of electrons, where  $\gamma = \frac{1}{\tau}$ , and  $\tau$  describes the relaxation time of the electron plasma. Note that the electron-electron interactions as well as the details of lattice structure are neglected in this scenario, and it is assumed that  $m$  takes some lattice characteristics into account. We shall describe  $m$  as the effective index and denote it as  $m^*$ . By assuming that  $E(t) =$

$E_0 e^{-i\omega t}$  is a periodic wave with angular frequency,  $\omega$ , then the solution to the above differential equation would be in the form of  $x(t) = Ae^{-i\omega t}$ , where,

$$A = \frac{q}{m^*(\omega^2 + i\Gamma\omega)} \quad (4.2)$$

By incorporating the electron displacement into the macroscopic polarization,  $P = -nqx$ , where  $n$  is the electron density, it will yield,

$$P = -\frac{nq^2}{m^*(\omega^2 + i\Gamma\omega)} E \quad (4.3)$$

Thus, the displacement field,  $D = \epsilon_0 E + P$ , can be described by,

$$D = \epsilon_0 \left[ 1 - \frac{\omega_p^2}{(\omega^2 + i\Gamma\omega)} \right] E \quad (4.4)$$

where  $\omega_p = q \sqrt{\frac{n}{\epsilon_0 m^*}}$  is the plasma frequency of the free electron plasma. Therefore, the dielectric function of the free electron plasma can be written as,

$$\epsilon(\omega) = 1 - \frac{\omega_p^2}{(\omega^2 + i\Gamma\omega)} \quad (4.5)$$

Note that we arrive at this relation while assuming an ideal free-electron metal, where  $\epsilon$  tends to 1 for higher frequencies ( $\omega > \omega_p$ ). However, in practice, there is extra polarization due to the positive ions in the material; hence, the total polarization can be described by adding the term  $P_\infty = \epsilon_0(\epsilon_\infty - 1)E$  to equation 4.3. Thus, equation 4.5 can be modified to,

$$\epsilon(\omega) = \epsilon_\infty - \frac{\omega_p^2}{(\omega^2 + i\Gamma\omega)} \quad (4.6)$$

The above relationship is known as the Drude permittivity model. This model will be used in the following chapter to describe our materials [38].

## 4.1.3 Surface Plasmons Applications

### 4.1.3.1 Slow and Backwards Light

The inherent speed of light is an attractive solution to transport problems in general, however, it comes with an unattractive drawback: the inability to control optical signals. Optical computer networks are becoming an increasingly hot trend. Multiple efforts are put into building all-optical systems to eliminate the need for optical-electronic conversion systems, which tend to be inefficient [38]-[42]. Hence, there is an increasing need for reliable optical switches [43]. This is where slow light enters the picture. The ability to tune the speed of light will enhance the amount of control imposed on the light path, which in turn will enable building faster, more reliable systems that use less power. In addition, slow light can elongate the light-matter interaction time and can hence be used to enhance sensors [44].

When light propagates into a material, its speed is said to be reduced, as the phase velocity,  $v_p = c/n = \omega/\beta$ , is reduced. However, technically speaking, the speed of light is not defined by the phase velocity, but rather the group velocity, as it takes into account the velocity of all the frequency components within the light pulse [45]. The group velocity of light is defined as  $v_g = d\omega/d\beta$ , which is the rate of change of the phase velocity. It can be deduced then that the group velocity depends on the *change* of refractive index for a given range of frequencies, rather than the *value* of the refractive index. In other words, the dispersion characteristic of the material are taken into account, and play a huge role in determining the overall light speed. For instance, in order for light to be slowed down, there needs to be a large variation in the refractive index for a small range of frequencies ( $\Delta n/\Delta\lambda \sim \uparrow\uparrow$ ); this is the very definition of a highly dispersive material.

Plasmonic materials operating near their resonance tend to be highly dispersive, which makes them ideal contenders for implementing slow light. In addition, the effective refractive indices of plasmonic materials tend to be particularly high near the resonance (recall equation 4.4), which implies the presence of a significantly small phase velocity. To explain this in an intuitive manner, it can be stated that SPPs can be thought of as electrons coupled to electromagnetic waves. Hence, SPPs can be regarded as heavier particles than photons, and so it is sensible that the electromagnetic wave associated with them is a slower one.

The group velocity of light in plasmonic devices can be tuned using several mechanisms, such as controlling the device's dimensions [46] which allows for a wide range of frequencies to excite slow waves. More so, it has been proved numerically that a metal-insulator-metal (MIM) plasmonic waveguide is capable of not only slowing light, but of stopping light; this occurs when the power flow of the supported plasmonic mode ( $n_{eff} > \sqrt{\epsilon_d}$ ) is going in the opposite direction as that of an identical the supported photonic mode ( $n_{eff} < \sqrt{\epsilon_d}$ ) [47].

The phenomenon where the optical power is flowing in the opposite direction as the phase velocity is referred to as backwards propagation, or backwards light. In this scenario, the plasmonic material is operated in a spectral region that possesses a negative slope. Hence, applications relying on backwards waves are sometimes referred to as negative-index or negative refraction applications [47]. Backwards light can be used in metamaterial-like applications [49], such as perfect lenses that provide an unlimited resolution [50] and as cloaking devices [50], [52].

#### 4.1.3.2 Extraordinary Transmission

In 1944, Beth provided a formula that describes transmission through a circular subwavelength hole in a metal plane by solving Maxwell's equations [53]; he showed that the normalized transmission is proportional to  $(a/\lambda)^4$  where  $a$  is the diameter of the hole; this contradicted Kirchhoff's method, which showed an  $(a/\lambda)^2$  dependency. Hence, it can be deduced from Beth's theory that subwavelength holes are not an optimum medium for transmission. Therefore, it was surprising in 1998, when Ebbesen demonstrated that by using a subwavelength metallic cylindrical cavity, it is possible to get normalized transmission that is greater than unity [54]. This phenomenon has been referred to as extraordinary transmission (EOT). Ebbesen has attributed this unusual behavior to the presence of SPPs; this conclusion was reached on the premise that: 1) EOT did not exist for Germanium slits—marking the importance of metallic cavities. 2) The transmission spectra of metallic films showed a dependency on the angle of incidence, which is similar to the behavior of light that couples to SPPs through diffraction gratings [55]. In attempts to understand this phenomenon, it was discovered that the shape of the hole is not relevant, whereas the size of the hole is [56]. EOT is thought to occur due to the constructive coupling of two SP modes [56], [57]. In addition, EOT may be enhanced by using ENZ materials, or materials that have an almost zero permittivity [58], [58]. [60] demonstrated numerically the light in ENZ materials propagates along a thin shell, which aids in enhancing transmission. The unique properties of EOT allows it to be utilized in

applications such as subwavelength lithography, near-field scanning microscopy, optical modulators, and wavelength-tunable filters [54], [56]-[57].

#### 4.1.3.3 Plasmonic Sensors

Being surface waves with decent evanescent fields, SPPs are an intuitive solution to surface sensing techniques, where the material under test is placed directly on the surface of the optical sensor. A surface plasmon sensor is essentially a transducer, which essentially translates changes in a material of interest into refractive index changes. The sensor consists of a lasing device, an optical structure where the SPPs are interrogated, and an electronic read-out circuit to decipher the result of the SPP interrogation [61]. Certain characteristics of the sensor, such as sensitivity and stability, depend upon the properties of the transducer material, as well as its structure.

Because a good portion of the SPP mode is decaying into the lossy metal, the SPPs are not expected to propagate for long distances. For this reason, the SPP interrogation is performed simultaneously with the coupling of the incident light to the plasmonic waveguide. The dispersive nature of SPPs implies that the momentum of an SPP at any given frequency would be larger than the momentum of a free-space photon (recall equation 4.4, where  $\beta > k_0$ ); hence, momentum matching mechanisms are needed to couple light from free-space to plasmonics. There are two momentum matching main mechanisms: prism coupling and diffraction grating coupling [61], [62].

In prism coupling, the plasmonic material is sandwiched between air (or whatever surrounding media) and another dielectric material with a dielectric constant greater than that of the surrounding media. The dielectric material will exhibit the form of a prism. In this case, after the light is totally internally reflected within the prism, the in-plane momentum will be modified to  $k_{0x} = \sqrt{\epsilon} k_0 \sin\theta$ , where  $\epsilon$  is the prism permittivity. Thus, the momentum would have reached a value high enough to excite the surface plasmons [38].

The most appropriate configuration for sensing application is the Kretschmann configuration shown in Figure 4.2. The light is directed towards the prism, and then it is reflected within the prism, where the evanescent part of the field tunnels through the thin metal layer. The evanescent field then interacts with the analyte, or the material under test. Some of the detection methods that have been used with this configuration include measurement of resonant angle of incidence [63], measurement of the resonant wavelength of the incident wave [64], and measurement of the intensity of the reflected light wave [65].

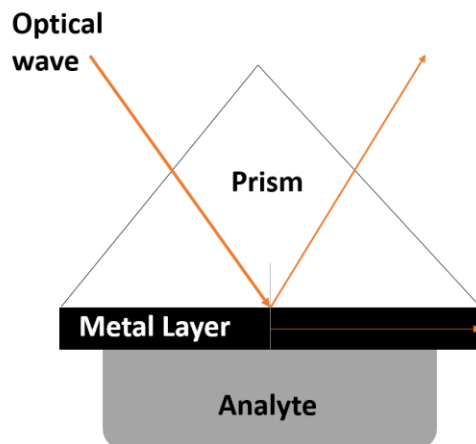


Figure 4.2. The Kretschmann configuration

Another way to resolve the momentum mismatch problem is by introducing periodic gratings to the surface as can be seen in Figure 2.5 (See Chapter 2, Section 2.3.2.3). The incident wave will be reflected away from the surface at several angles, which will modify the in-plane momentum to be equal to  $k_{0x} = k \sin \theta \pm m\Lambda$ , where  $m$  is an integer and  $\Lambda$  is the periodicity, which is equal to  $2\pi/a$ , where  $a$  is the lattice constant of the gratings. Thus,  $a, m$  and  $\theta$ , need to be adjusted to equate the in-plane momentum of the incident wave to the momentum of the surface plasmon wave. Some of the grating-based sensors work on measuring the light intensity variations at surface plasmon resonance [66]. Of these, a biosensor using gold gratings to measure biomolecular interaction in aqueous media has been reported [67].

#### 4.1.3.4 Nanoparticles

Plasmonic nanoparticles are conductive spheres with dimensions smaller than that of the wavelength. In 1908, Mie solved Maxwell's equations to reveal the extinction (scattering + absorption) properties of such particles [68], [69]. Nanoparticles are remarkable for having scattering cross-sections that are much larger than their diameter. Because of their attractive radiation properties, nanoparticles can be used as nanoantennas [70], [71], which are commonly used as near-field imaging devices [72]-[75]. Aside from imaging, nanoantennas based on nanoparticles can be used as therapeutic agents [75], [76].

Nanoparticles are frequently utilized for chemical and biological sensing applications [77], [78]. They are inherently sensitive as their SPP radiation surpasses their physical dimensions, which allows for a large evanescent field to overlap and characterize the surrounding medium. Generally, the sensitivity of a nanoparticle, or a nanorod—an

elongated nanoparticle—is defined as a shift in the resonance frequency of the scattering or absorption cross-section due to changes occurring in the surrounding environment. Also, the sensitivity of nanoparticles, or nanorods, is directly proportional to their aspect ratio [79]. Furthermore, the aforementioned strong sensitivity, as well as the low toxicity of metals [80] has prompted biophysicists to use nanoparticles as optical labels [75], [80], and [81]. The nanoparticle is injected into a living cell of interest, and can then be easily tracked by its strong scattering field.

## 4.2 The Mid-Infrared (Mid-IR)

Most of the research work done in the area of plasmonics has been centered on the visible and NIR spectral range, as these regions guarantee strong localization of SPP modes of common metals, which is necessary for several nanophotonic applications. Lately, though, there has been an increased level of interest in creating plasmonic structures for mid-IR applications. In this section, we mention some of the applications and merits of working in the mid-IR region. We also discuss the means by which applying plasmonics to the mid-IR can be made possible.

### 4.2.1 Mid-IR Applications

Generally, the mid-IR range is not strictly defined, but it appears that most mid-IR applications lie within the 2 to 20 $\mu\text{m}$  range. The appeal of the mid-IR region is chiefly due to the fact that it contains the absorption resonances of many molecules of interest, such as ammonia, carbon monoxide, methane and acetone. Each of these molecules has a unique spectral pattern that is considered to be a “molecular fingerprint.” These molecules are very diverse and prove to be critical in a variety of sensing applications ranging from chemical and biological sensing applications [83] to industrial sensing applications, such as food composition and analysis [84]. In addition, the mid-IR can be utilized for applications in environmental monitoring, as the absorption bands for most gases tend to lie in this spectral area [83], [85], [86] and [87]. Another feature unique to the mid-IR is that it contains hot body radiations. Thermal emissions are characterized by emissivity, where the peak emissivity for a perfect blackbody in temperatures ranging from 200 to 1400K is located in the mid-IR [87]. Moreover, the mid-IR hosts atmospheric transparency windows, particularly, the 3-5 $\mu\text{m}$  and the 8-13 $\mu\text{m}$  transmission windows [88], which can be used as band filters for thermal detection and imaging applications. This feature nominates the mid-IR for security related applications such as countermeasures against heat-seeking missiles [89], [89] and trace gas detection [91], [92]. A great advantage for working in the

mid-IR is that semiconductor electronics are transparent in this range, which may facilitate the integration of electronic and plasmonic components. This may pave the way for creating true on-chip optoelectronic devices [87].

In spite of its numerous benefits, the mid-IR region only started gaining attention somewhat recently, for the practical utilization of this range has been quite challenging. This is mainly due to the fact that an effective mid-IR laser has not been introduced until 1994 [93] when the quantum cascade laser was invented [93]-[95]. Additionally, low-noise detectors were unavailable until the advent of quantum-well infrared detectors [96]-[101].

## 4.2.2 Conventional Plasmonics at the Mid-IR

Since the real part of the permittivity of common metals has a very large negative value at the mid-IR, the electric field to possess a small penetration depth within the metal. The problem with this scenario is that the majority of the field is located in the cladding, which essentially means that the SPP is poorly confined. To elaborate, the effective refractive index of the SPP mode,  $n_{SPP}$ , for common metals in mid-IR becomes comparable to the dielectric permittivity of the cladding. This causes the out-of-plane wavevector,  $\kappa$ , which describes the rate of decay in the dielectric, to be very small, indicating the presence of poorly confined waves. This relation is shown in equation (4.7) [87], [102].

$$\kappa = k_0 \sqrt{n_{SPP}^2 - \epsilon_d} \quad (4.7)$$

Confinement is enhanced when  $n_{SPP} \gg \epsilon_d$ ; this is satisfied near the plasma resonance for metals, which lies in the visible and NIR range. This makes traditional plasmonic devices unpractical for applications that require high field localization such as sensing and on-chip transmission.

## 4.2.3 Designer Plasmonics

Due to the poor confinement of conventional plasmonic materials at the mid-IR, several directions have been taken in order to enhance the SPP localization in this range, and to create mid-IR plasmonic structures that can compete and even excel over the traditional NIR plasmonic structures. Amongst the approaches to realize this is by creating “spoof” SPPs [103]. This is generally done by introducing subwavelength corrugations to a perfect conductor; the incident wave excites some modes within each of the corrugations, with the fundamental mode being the most dominant. The multiple corrugations create a lossy effective medium, which essentially reduces the group velocity of light, hence shifting the dispersion curve towards the longer wavelengths. The new plasma resonance of the



structure will be determined by the cut-off frequency of the waveguide mode [87], [102], and [103]. The same scenario can be applied to metals, where the interaction of spoof SPPs and real SPPs will cause the plasma frequency of the metal to be reduced [103].

Another means to induce plasmonics at the mid-IR is through the use of highly doped semiconductors [97]; this will be the focus of our work. The idea is very simple: by increasing the carrier count of the semiconductor, it will start to behave as a metal. Furthermore, the concentration of carriers will determine the plasma frequency of the “new” semiconductor metal. This is easily explained by the relation,  $\omega_p = q\sqrt{n/\epsilon_0 m^*}$ , presented in section 4.1.2. For a doped semiconductor material, the plasma resonance will be described as,

$$\omega_p = q \sqrt{\frac{N_d}{\epsilon_0 m^*}} \quad (4.8)$$

where  $N_d$  is the doping concentration in  $\text{cm}^{-3}$ . Hence, plasma resonance tunability can be achieved through varying the doping concentration. Traditional semiconductors such as silicon [104] and germanium [105] were suggested to work as designer plasmonic materials. Using a semiconductor to induce plasmonic characteristics is recommended for several reasons. Semiconductors, in general, have smoother surfaces, as well as higher motilities, in comparison with metals, which causes them to suffer from less scattering losses [106]. In addition to this, semiconductors are much easier to handle in terms of nanofabrication.

We choose to focus on studying the plasmonic properties of doped silicon, seeing as silicon is the industry standard, and is the most established and understood between the two. The CMOS-compatibility of silicon is a great advantage, as it can aid in creating inexpensive devices that are eligible for batch fabrication. Moreover, these devices will also have the potential of bridging the gap between electronic devices and plasmonic devices and would allow for true chip-scale integration [107]. Such integration could mean smaller, faster, and cheaper devices.

# Chapter 5: Mid-IR Doped Silicon Plasmonics

By now, it is clear that merging the unique capabilities of plasmonic behavior with the fruitful mid-IR region, will open the door for many new applications. In this chapter, we inspect the capabilities of doped silicon as a plasmonic waveguide in the mid-IR spectral region, specifically the 2.5-12 $\mu\text{m}$  range. We start by constructing the material models that will be used in our simulations. Then in order to understand the spectral properties of doped silicon in the mid-IR, we study the dispersion characteristics of several structures, such as a slot structure, a rectangular-shell structure, and a silicon-insulator-silicon (SIS) structure. All these structures are capable of highly confining the light in the low-index-region, making them suitable for sensing applications, which are much sought-after in the mid-IR region. For this reason, we study the potential for sensitivity for several of our structures. We also study the sensing capabilities of a nanodisk, which unlike previous structures, relies on localized SPPs rather than propagating ones. Furthermore, we test our waveguide's ability for inducing slow light.

## 5.1 Material Modelling

### 5.1.1 Determining the Doping Concentration

Our main target is to tune the plasma resonance of doped silicon to a particular frequency of in the mid-IR region, and for that we need to find out the required doping concentration. We start by constructing a material model based on the Drude model for permittivity (Section 4.1.2, equation (4.6)). To obtain the parameters for our Drude model, we start by making the common assumption that  $\varepsilon_\infty$  is equal to the silicon permittivity. Given the targeted frequency ( $\omega$ ), the plasma frequency ( $\omega_p$ ) can be obtained by assuming that  $\Gamma \ll \omega$ ; from there, (4.6) can be approximated to  $\varepsilon_m(\omega) - \varepsilon_\infty = \omega_p^2/\omega^2$ . The downfall of this approach is that the condition for the collision frequency,  $\Gamma \ll \omega$ , must be satisfied. The collision frequency can be highly variable since it is dependent on the mobility, which in turn is affected by a host of factors such as the choice of dopant(s), the operating temperature and the intensity of the incident field [108]. However, for simulation purposes that do not require a propagation constant, it is ok for it to be neglected. In general, it is

best to use an iterative algorithm to obtain the values for the plasma frequency and the collision frequency. This is mandatory when the value of the desired collision frequency is comparable to that of the operating frequency. Once the desired plasma frequency is obtained, the required doping concentration can be calculated from (4.8).

### 5.1.2 Relationship between Doping Concentration and Plasma Resonance

We examine the effect of varying the doping concentration on the modal effective index of a simple plasmonic slot waveguide. The generic structure of our slot waveguide as well as the mode are shown in Figure 5.1. The simulation was done using Lumerical software; PML boundaries are used and a mesh size of 0.1nm is employed. These parameters are used for modal simulations throughout Sections 5.1, 5.2 and 5.3. The doping concentration is varied from  $1 \times 10^{15} \text{cm}^{-3}$  to  $5 \times 10^{20} \text{cm}^{-3}$ . For each doping concentration, the plasma frequency is calculated using (4.8). Then, by assuming that the doping is done with phosphorus, the mobility may be computed using the tool provided by [109].

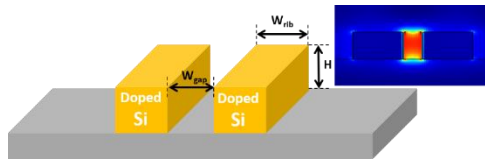


Figure 5.1. Slot structure; inset shows slot mode with gap width,  $W_{gap}$ , rib width,  $W_{rib}$ , and height,  $H$ .

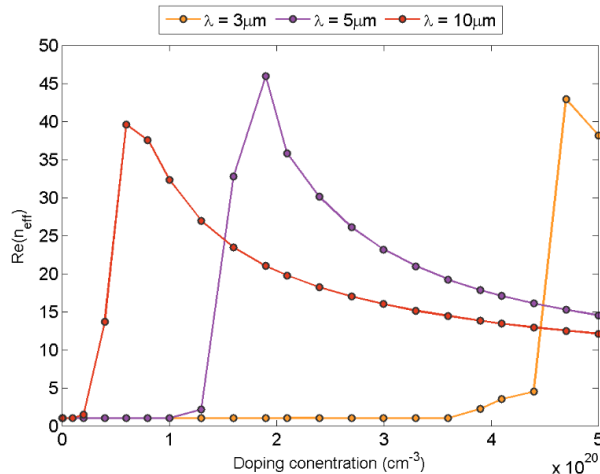


Figure 5.2. Doping concentration vs. modal effective index for  $\lambda = 3 \mu\text{m}$ ,  $5 \mu\text{m}$  and  $10 \mu\text{m}$  for a slot waveguide with  $W_{gap} = 5 \text{nm}$  and  $W_{rib} = 50 \text{nm}$ .

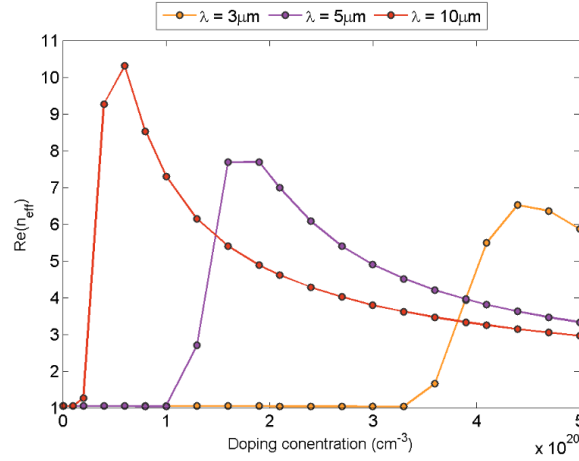


Figure 5.3. Doping concentration vs. modal effective index for  $\lambda = 3\mu\text{m}$ ,  $5\mu\text{m}$  and  $10\mu\text{m}$  for a slot waveguide with a  $W_{\text{gap}} = 100\text{nm}$  and  $W_{\text{rib}} = 50\text{nm}$ .

Accordingly, the damping frequency is computed using  $\Gamma = q/m^*\mu$ . Two slot dimensions are studied. The first slot has a rib width of 50nm and an extremely small gap width at 5nm; the modal effective indices for different doping levels are depicted in Figure 5.2. The wavelengths are fixed at 3 $\mu\text{m}$ , 5 $\mu\text{m}$ , and 10 $\mu\text{m}$ . The same scenario is applied for the second slot, which has the same rib width, but a much larger gap width at 100nm. The results for this slot are shown in Figure 5.3.

It is clear that for each wavelength, the effective index tends to shoot for a certain frequency. The gap size has no bearing on the location of the effective index peak, but a smaller gap size seems to generally correspond to a higher effective refractive index, indicating higher confinement. A high effective refractive index implies not only optical confinement, but also a proximity to the plasma resonance of the material. For higher wavelengths, plasma resonance is achieved at lower doping concentrations; this can be deduced from (4.8). To understand this phenomenon better, let us take a closer look at the 10 $\mu\text{m}$  curve in Figure 5.3. By observing the 1D and 2D modes at various doping concentrations, as shown in Table 5.1, it becomes clear that by increasing the doping, the optical confinement is enhanced. Note that the height of the waveguides was set to 300nm for the 2D modes. The optical confinement factor (OCF) is defined as,

$$OCF = \frac{\int_{-w/2}^{w/2} |E|^2 dx}{\int_{-\infty}^{\infty} |E|^2 dx} \quad (5.1)$$

where  $E$  is the electric field of the 1D mode, and  $w$  is the gap width. The optical confinement for each doping concentration is shown in Table 5.1.

Table 5.1. Optical confinement factors (OCFs) for different doping concentrations and the associated modes.

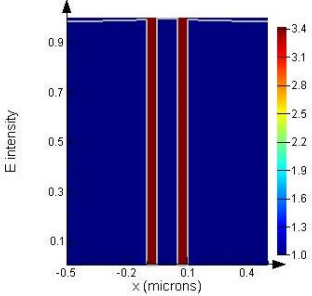
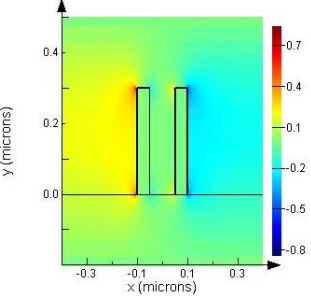
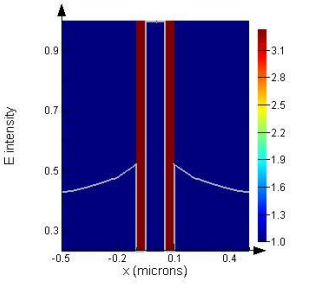
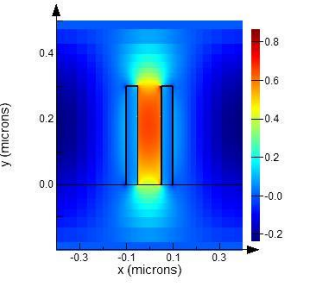
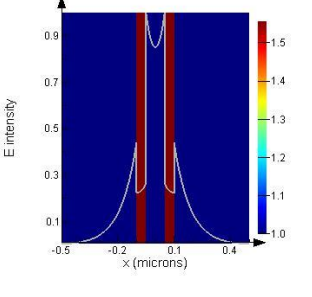
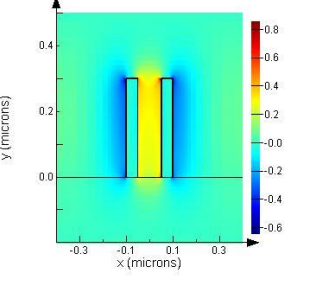
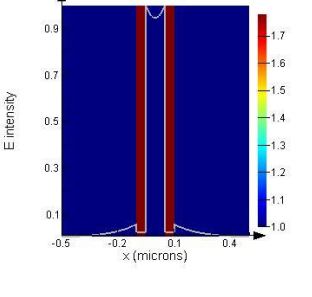
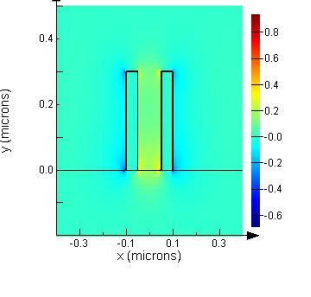
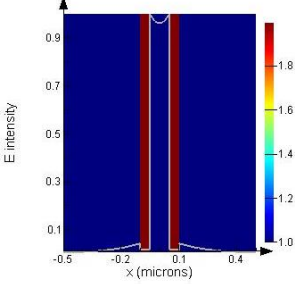
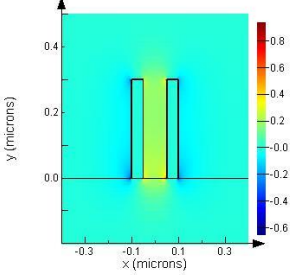
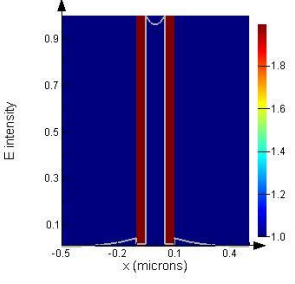
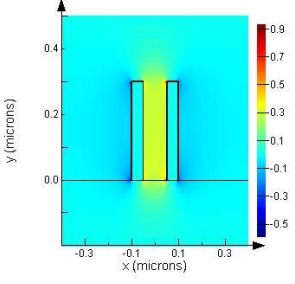
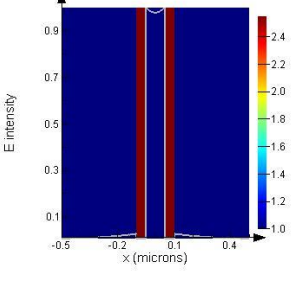
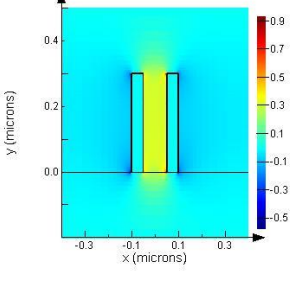
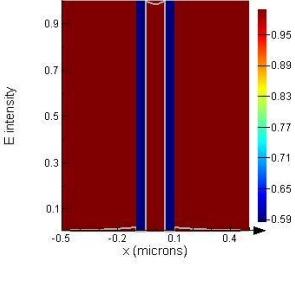
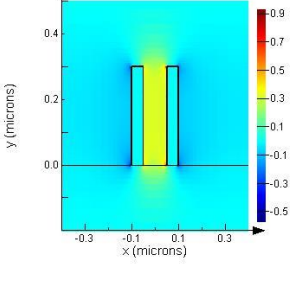
$N_d$ (cm <sup>-3</sup> )	OCF	1D Mode	2D Mode
0 (Si)	0.49		
$2 \times 10^{19}$	0.57		
$4 \times 10^{19}$	0.61		
$6 \times 10^{19}$	0.75		

Table 5.1 (Contd.)

$N_d$ (cm <sup>-3</sup> )	OCF	1D Mode	2D Mode
$8 \times 10^{19}$	0.83		
$2.1 \times 10^{20}$	0.94		
$3.6 \times 10^{20}$	0.96		
$5 \times 10^{20}$	0.97		

When the doping is increased, the mode appears to be transitioning from an unconfined state to a confined one. At  $N_d = 6.00 \times 10^{19} \text{cm}^{-3}$ , the plasmonic condition ( $\omega < \omega_p$ ) appears to have been achieved, and the mode appears to be localized. The higher doping concentrations have higher OCFs, indicating that they satisfy the plasmonic condition for the  $10\mu\text{m}$  wavelength. Higher concentrations also tend to have a lower effective index, as they are farther away from the plasma resonance.

### 5.1.3 Material Modeling

To study the dispersion characteristics of highly doped silicon in the mid-IR region, we constructed three material models with resonances in the 2 -  $10\mu\text{m}$  range. First, we were curious as to how much we can reduce the resonant plasma wavelength of doped silicon. For this purpose, we needed to use a doping concentration that is extremely high, yet feasible. So for our first material, we assumed that  $N_d \approx 5 \times 10^{20} \text{cm}^{-3}$ ; the plasma frequency and the collision frequency is obtained as explained previously. For simplicity purposes, we shall refer to this material as material A. The propagation constant,  $\beta$ , is maximized when the metal permittivity is equal to the negative of the dielectric permittivity ( $\epsilon_d = -\epsilon_m(\omega)$ ), marking the location of the plasma resonance (refer to equation (4.4)). Hence, according to Figure 5.4, which shows the plot of the real permittivity of the doped silicon against the wavelength, the material dispersion should be maximum around  $3\mu\text{m}$  (at  $2.7\mu\text{m}$  to be exact), if we assume that the surrounding material is air ( $\epsilon_d = 1$ ).

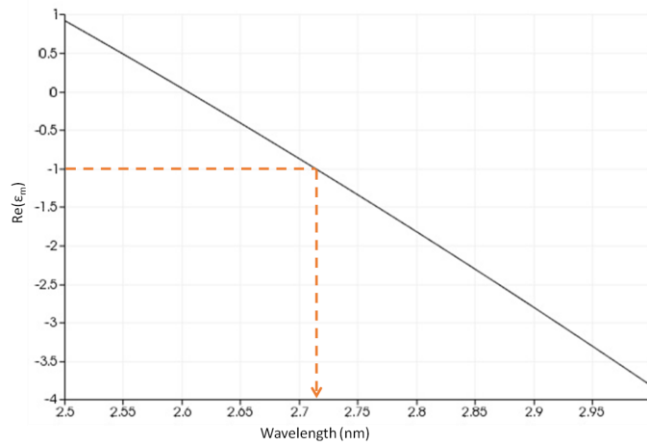


Figure 5.4. The real permittivity of doped silicon with  $N_d \approx 5 \times 10^{20} \text{cm}^{-3}$  versus the wavelength. Assuming that the surrounding dielectric material is air, the dispersion will be maximum near  $3\mu\text{m}$ .

We then attempted to create dispersive material models based on the Drude model for permittivity for plasma resonances at slightly longer wavelengths, namely,  $5\mu\text{m}$  and  $10\mu\text{m}$ . We shall refer to the doped silicon with resonances at  $5\mu\text{m}$  and  $10\mu\text{m}$  as material B and material C, respectively. The Drude parameters were obtained using the technique described in Section 2.1. The doping concentration for material B and material C were found to be around  $1.5 \times 10^{20} \text{ cm}^{-3}$  and  $3.6 \times 10^{19} \text{ cm}^{-3}$ , respectively. This is in good agreement with the results depicted in Figure 5.2 and Figure 5.3.

#### 5.1.4 Single-Interface Propagation

As discussed in Section 4.2.2, conventional plasmonics based on noble metals face some confinement issues at the mid-IR. On the other hand, plasmonics based on doped silicon are expected to resolve this issue, seeing as their plasma resonance was designed to be in the mid-IR range. To verify this, we tested the SPP propagation of a  $400\text{nm}$ -thick slab over a  $\text{SiO}_2$  substrate using doped silicon, and compared it to that of a  $400\text{nm}$ -thick silver slab in the mid-IR. Using Optiwave software, PML boundary conditions were used and a mesh size of  $0.44\mu\text{m}$  was used in all directions. The simulation time was  $4 \times 10^{-4}\text{s}$ . The waveguides were excited at  $3\mu\text{m}$  and the wave was propagated for  $10\mu\text{m}$ . Figure 5.5 shows the FDTD results for the single-interface propagation. As shown in Figure 5.5(a), the wave is confined near the surface for doped silicon and is able to propagate successfully for  $10\mu\text{m}$ . This is unlike the SPP propagation in silver, which shows very little transmission beyond the  $4\mu\text{m}$  mark, and depicts a very leaky wave, as shown in Figure 5.5(b).

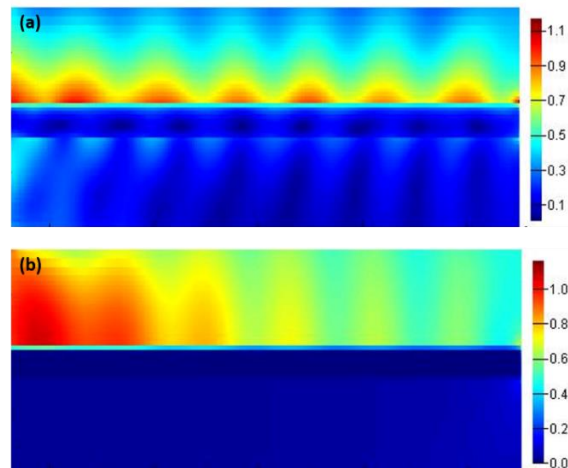


Figure 5.5. Single-interface propagation of a  $400\text{nm}$  (a) doped silicon slab, (b) silver slab on an  $\text{SiO}_2$  substrate.



## 5.2 The Finite-Width Slot Waveguide

In this section, we perform detailed dispersion calculations for various dimensions of the doped silicon slot waveguide, shown in Figure 5.1. We also investigate its performance as a mid-IR sensor, as well as a slow light medium.

### 5.2.1 Modal and Dispersion Simulations for Slot Waveguide

We examine the dispersion relations for the slot waveguide, with a 5nm gap and 50nm rib width, using the materials we constructed in Section 5.1. We also study the dispersion relations of a similar slot waveguide with a 100nm gap and 50nm rib width. However, before we move on to studying the dispersion of doped silicon, we perform a brief study on the dispersion of undoped silicon. Figure 5.6 shows the silicon dispersion curve in the mid-IR region, from 1 $\mu\text{m}$  to 12 $\mu\text{m}$ , for a slot waveguide with a 5nm gap and another one with a 50nm gap. The modal effective index for the 5nm gap slot is generally higher than that of the 100nm gap slot. This is due to the higher localization of the mode of the 5nm gap, as evidenced by inset b. There are two main regions in this dispersion graph. Region 1 is the dielectric region, which is exhibited by a conventional dielectric mode, shown in insets a and b, for the 100nm and 5nm gap, respectively. Region 2 starts around 3 $\mu\text{m}$ , and is characterized by having an extremely leaky mode, as made apparent by insets c and d, 100nm and 5nm, respectively.

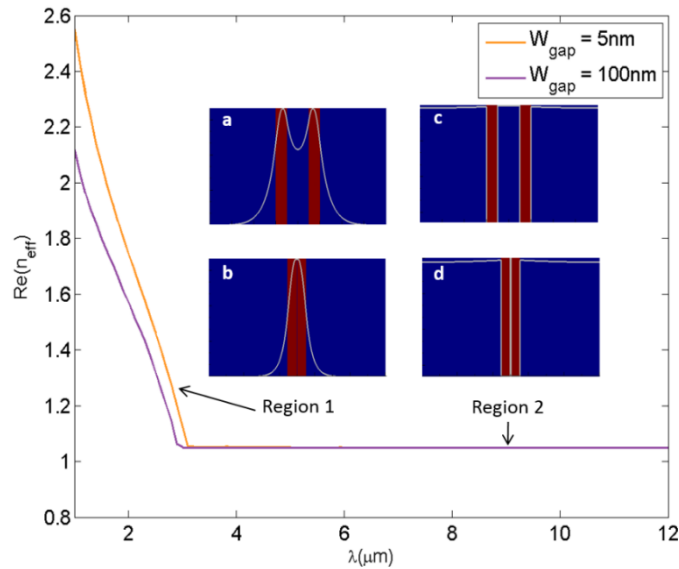


Figure 5.6. The dispersion relation for the silicon slot structure with a 5nm gap and a 100nm gap. Insets a and b belong in Region 1 and describe the dielectric mode for the 100nm gap slot

waveguide and the 5nm gap slot waveguide, respectively. Insets c and d belong in Region 2 and depict a leaky mode for the 100nm gap slot waveguide and the 5nm gap slot waveguide, respectively.

We now study the dispersion of the 5nm gap slot waveguide with a 50nm rib width using material A. Figure 5.7 confirms that the plasma resonance indeed occurs around  $2.7\mu\text{m}$ . As implied by (5), the modal effective index should reach infinity around the plasma resonance; and indeed the simulation showed a very high modal effective index at order of  $10^5$ . There are three regions characterized with different behaviors in the dispersion curve. Region 1 ( $1\text{nm} < \lambda < 2.7\mu\text{m}$ ) represents dielectric operation where the mode is guided by total internal reflection. Region 2 ( $2.7\mu\text{m} < \lambda < 2.8\mu\text{m}$ ) is represented by a steep negative slope between the peak and Region 1; this indicates a negative group velocity. The negative dispersion paired with the high modal effective index in Region 2 conveys that this spectrum area is very valuable for slow and fast light applications. Region 3 ( $\lambda < 2.8\mu\text{m}$ ) depicts the plasmonic region and shows a highly confined slot mode.

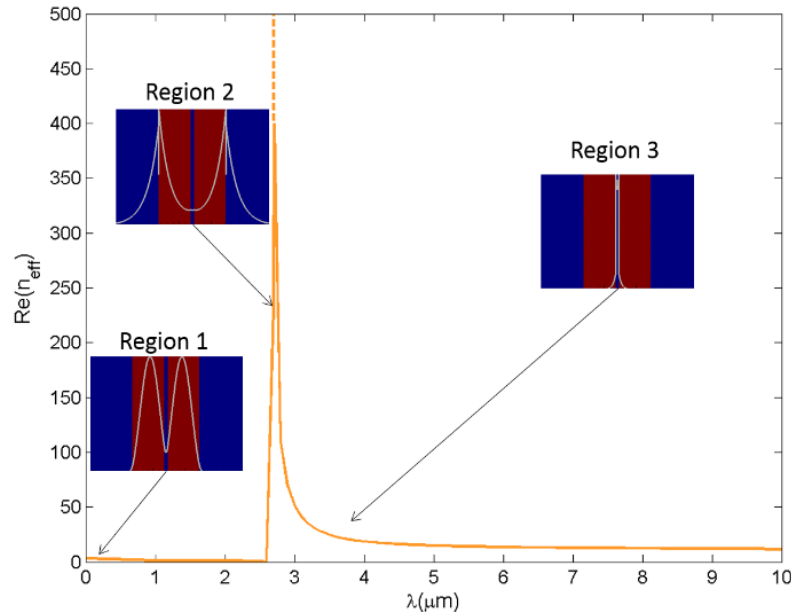


Figure 5.7. The dispersion relation for the slot structure showing the 3 main regions: Region 1: dielectric region, Region 2: negative dispersion, Region 3: plasmonic region.

Materials B and C were designed to resonate at specific wavelengths. The curves in Figure 5.8 confirm that the dispersion curves were effectively tuned to resonate at the desired wavelengths, which are  $5\mu\text{m}$  and  $10\mu\text{m}$ . It is clear that by lowering the doping concentration, the dispersion curve is red-shifted. The general trend—behavior of the three

regions—of the curves seems to be the same regardless of the doping amount. Also, similar to material A, the simulation was able to compute extremely high effective indices at the plasma resonance with the order of  $10^5$  for material B and material C.

The dispersion curves were studied in a similar approach for a slot with a 100nm gap and 50nm rib width. The 100nm gap is of interest not only because it is easier to fabricate, but also because it is large enough to confine fluids, making it eligible for biological and chemical sensing applications. Figure 5.9 shows the dispersion curves for material A, B and C for the 100nm gap. It is apparent that the main difference between the curves for the 5nm gap and the 100nm gap is that the 100nm gap seems to host smaller effective modal indices. This indicates that confinement is lower for larger gaps. This is intuitive, since the gap, which is responsible for squeezing the mode, is physically larger. However, the simulation shows a modal effective index of  $10^5$  at the plasma resonance for each one of the materials, conveying the possibility that the plasmonic gap width renders itself irrelevant when the structure is excited at its plasma resonance.

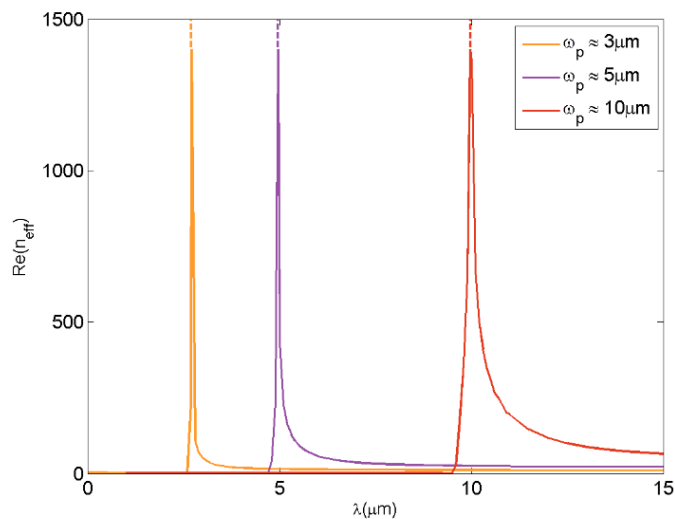


Figure 5.8. Dispersion curves for the 5nm gap slot structure for three different doping concentrations. The plasma resonance exists around 3, 5, and 10 $\mu$ m.

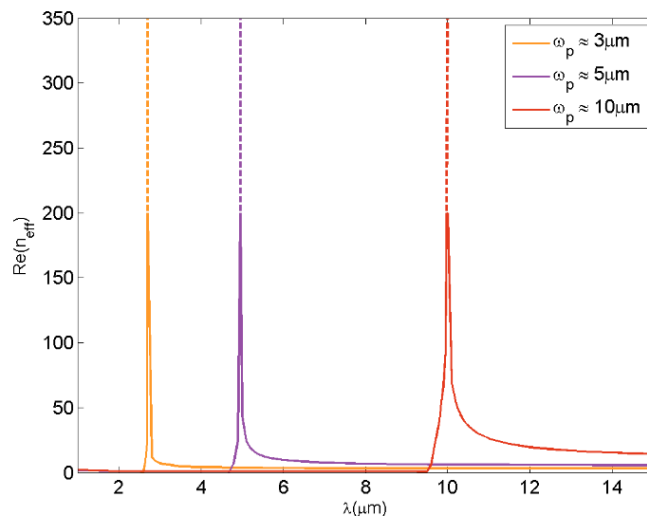


Figure 5.9. Dispersion curves for the 100nm gap slot structure for three different doping concentrations. The plasma resonance exists around 3, 5, and 10 $\mu$ m.

We expand to the previous studies by studying the general effect of varying the slot dimensions. We start by examining the effect of varying the rib width on the effective index at the plasma resonance for the three materials with a fixed gap width of 5nm. The rib width is varied from 50nm to 10mm. The modal effective index has not been affected in the least bit by this variation, and remained constant for each of the materials. The same simulations have been repeated for the 100nm gap slot, and still, the modal effective index remained the same. Theoretically, the modal effective index should be infinite at the plasma resonance regardless of the dimensions, so these results are acceptable. However, changing the dimensions affects the modal effective index *near* the resonance. For that reason, we test the effect of varying the gap width from 5nm to 100nm by exciting all three materials near their resonances. The results are shown in Figure 5.10. As expected, the highest modal effective index is corresponding to the 5nm gap, owing to the extreme localization of the slot mode created by the small gap. The effective index variation is almost exponential with the gap width. Also, the material with least amount of doping—material C—has a consistently higher modal effective index than the other materials.

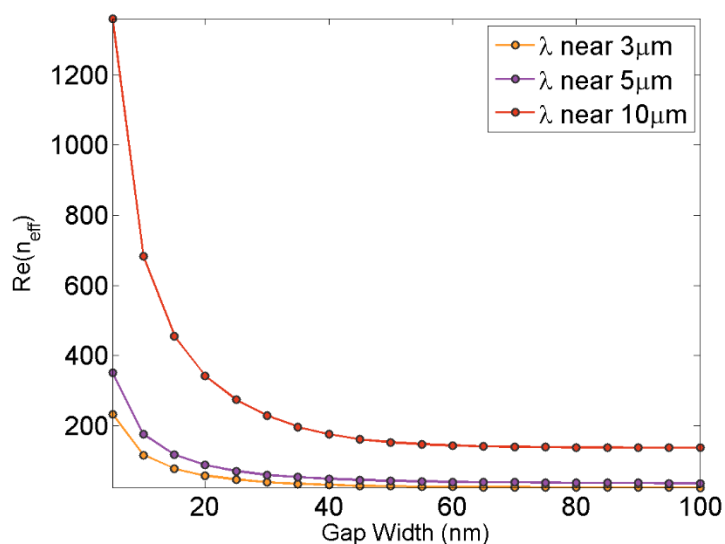


Figure 5.10. Plot of the effective modal index near resonance against the gap width. The plot shows the curves for a doped silicon slot with three doping concentrations with their resonances indicated in the legend; the rib width is fixed at 50nm.

It is also important to observe the effect of the rib width on the modal effective index. For this purpose, three rib widths—50nm, 100nm, 250nm—were employed using material A, while varying the gap width from 5nm to 100nm, as described by Figure 5.11. Altering the rib width does not have the same drastic effect on the effective index as altering the gap width. It is also clear that for very small gap widths (5-20nm), there is a complete overlap between the curves, indicating that the gap width is far more dominant than the rib width. The effect of the rib width becomes more pronounced for larger gap widths. The general trend appears to be that larger rib widths have smaller effective indices. It is also apparent that the difference between a 50nm and 100nm rib width is much more obvious than the difference between 100nm and 250 nm, which is very minute.

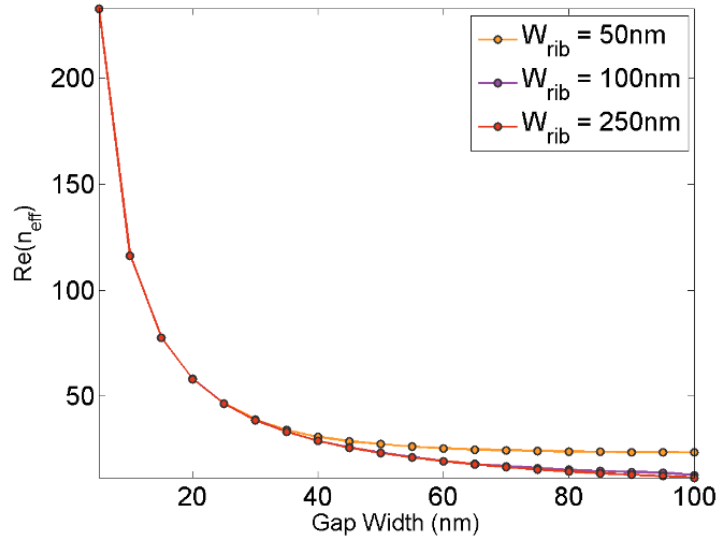


Figure 5.11. Plot of the effective modal index near resonance against the gap width for the doped silicon slot. The rib widths are set at 50, 100 and 250nm, and the doping concentration is fixed at  $5 \times 10^{20} \text{cm}^{-3}$ , while the gap width is varied from 5nm to 100nm.

## 5.2.2 Applications for the Plasmonic Slot Waveguide

### 5.2.2.1 Chemical and Biological Sensing Applications

As mentioned in the previous section, the 100nm gap slot makes for a good candidate for chemical and biological sensing. Slot structures are ideal for sensing since they are capable of confining the light in the same area where the fluid-under-test is guided. This aids in creating a large overlap between the two, and maximizing the sensitivity. To demonstrate this, we excite a material C slot waveguide with a 100nm gap width and a 50nm rib width near its cut-off, and study the sensitivity by changing the surrounding refractive index to 1.25 and 1.5. We perform another study where only the refractive index of the gap is changed. Figure 5.12 shows that for an increase in the surrounding refractive index, the curve is red-shifted in a considerable amount. We investigate the potential for sensing by measuring the effect of changing the refractive index of the surrounding environment on the effective index of the waveguide. We quantify this by measuring the wavelength shift per refractive index change in the surroundings. This gives an average of 920nm per refractive index unit (RIU) when the refractive index of the entire surrounding is changed, and 1050nm/RIU when the refractive index of the gap is changed. The two sensitivities are fairly close, indicating that the placement of the material under test only mildly affects its sensitivity. Moreover, since the material's response to its surroundings is high, then it is expected that once this material is put into a sensor configuration—such as

the Mach-Zehnder interferometer, or the ring-resonator—the sensitivity should be boosted considerably.

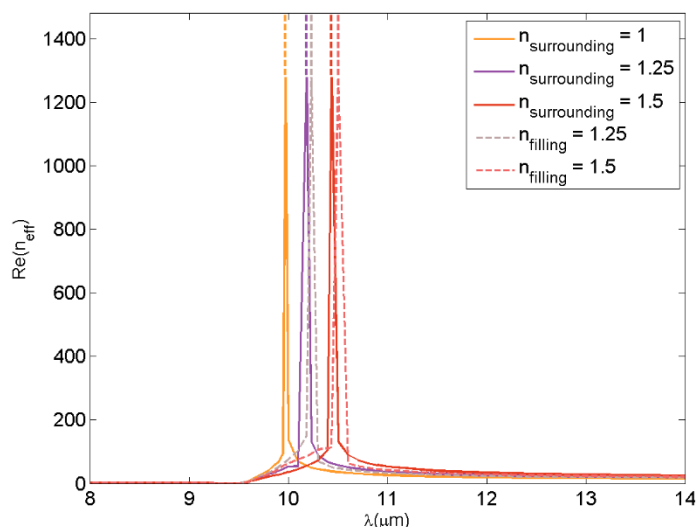


Figure 5.12. The solid curves depict the dispersion of a 100nm gap width, 50nm rib width doped silicon slot waveguide immersed in a dielectric medium. The dashed curves depict the dispersion of a slot waveguide with a dielectric filling in the gap only.

### 5.2.2.2 Slow Light and Negative-Index Applications

The presence of a negative slope in the dispersion relation indicates that the phase velocity and group velocity have opposite signs, which implies the presence of a backwards wave or fast light [110], [45]. Viewed from another perspective, the negative slope means that the material has a negative refractive index, which makes it suitable for building metamaterials [111].

On the other hand, the highest modal effective index that was found during our simulations was 307530; this was achieved for the 5nm gap slot waveguide based on material C. The very high effective index signifies a very low phase velocity, which makes this design an excellent candidate for slow light operation [110]. The group velocity of light can also be further tuned by adjusting the dimensions of the waveguide—smaller dimensions for slower light, as implied by Figure 5.10 and Figure 5.11.

To demonstrate the capability of the slot waveguide for light slowing, 3D FDTD simulations are used. Using Lumerical software, PML conditions were invoked, and a mesh size of 0.1nm was used. A signal is near the material C resonance (10 $\mu$ m) of a 5nm gap,

50nm-wide, 50nm-thick, and 2 $\mu\text{m}$ -long plasmonic slot waveguide. These results are then compared with a silicon waveguide with the exact configuration as the plasmonic slot. Figure 5.13 shows the time simulation versus the real part of the electric field component in the propagation direction. The delay is defined as the time difference between the peaks of the two signals. There is a delay of about 200fs between the output of the plasmonic slot and the silicon slot. The amplitude of the wave propagated through doped silicon wave is smaller than the one propagated through silicon. This is because of the higher losses of doped silicon, owing to the larger penetration depth.

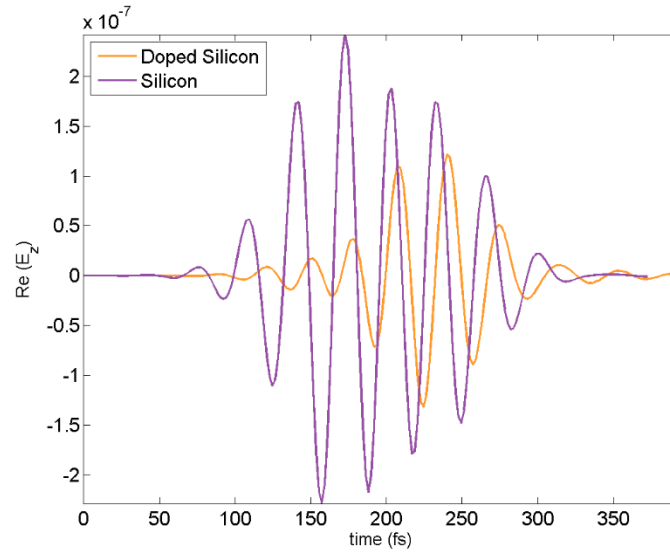


Figure 5.13. The time plot of the output electric field pulse from a plasmonic doped silicon slot waveguide and a dielectric silicon slot waveguide.

### 5.3 Rectangular Shell Waveguide

Following a similar approach as the one employed in Section 5.2, we study the dispersion curves for a rectangular shell structure, similar to the structure proposed in [112]. A major benefit for using this structure is that it provides 2D confinement, and hence, has the potential for providing higher localization than the slot structure. Another advantage for this structure is that it provides an intuitive solution for confining gases, making it excellent for environmental and chemical sensing applications, as will be demonstrated. Also, the discontinuity between the metal-dielectric interfaces exists vertically and horizontally, which allows the invariable propagation of both TE and TM waves; this is discussed in detail in [112].



Using material A, the dispersion curves for a 30 x 50nm rectangular gap waveguide (shown in Figure 5.14(a)) are studied. The modes are evaluated for three thicknesses: 25nm, 35nm and 45nm. The biggest difference between this waveguide and the slot waveguide is the presence of a very narrow operational bandwidth ( $\sim 2.6 - 3.3\mu\text{m}$ ). Outside of this band, the mode is cut-off. This suggests that this structure creates a natural mid-IR resonator filter. It may also be operated near the cut-off frequencies for ENZ applications such as extraordinary transmission. There are two main regions in the dispersion curve as shown in Figure 5.14(b). Region 1 represents the negative dispersion region, while Region 2 represents the plasmonic region. Region 2 features a slot mode as depicted in the inset in Figure 5.14(b). Similar to the plasmonic slot mode, this mode will be of great use in sensing applications as it ensures a large overlap between the material under test and the incident light wave. Region 1, on the other hand, features a very steep negative slope, which indicates a negative group velocity around these wavelengths, nominating this waveguide for slow and fast light applications. As expected, the doping has allowed this structure to resonate at  $2.7\mu\text{m}$ . At the resonance, the effective modal index obtained through the simulation is very high and has reached a value in the order of  $10^6$ . The variation in the thickness showed almost no change in the dispersion of the curve.

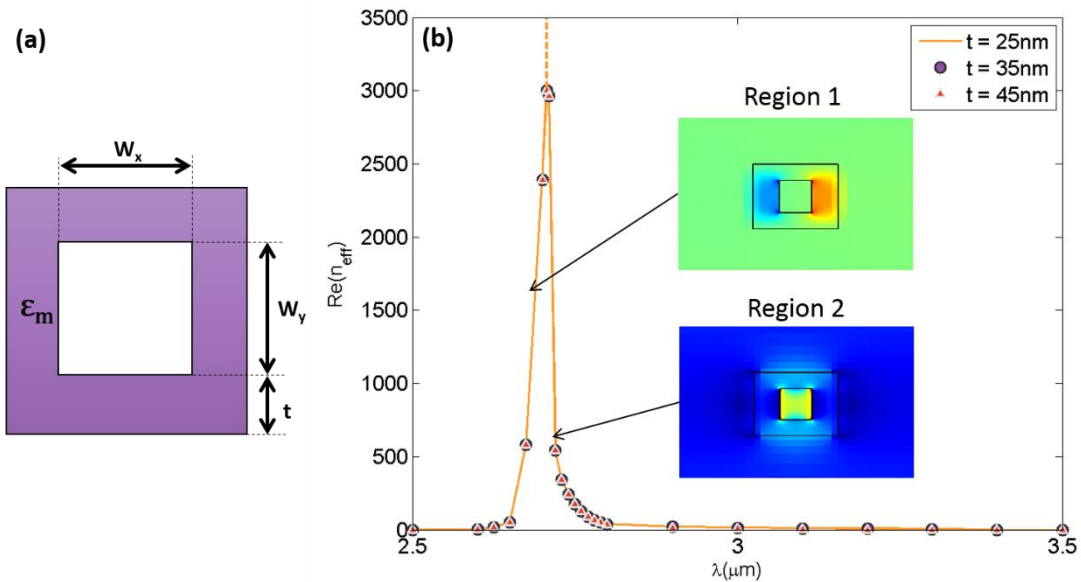


Figure 5.14. Performance of a rectangular shell sensor. (a) The rectangular shell structure with gap width,  $W_x$ , equal to 30nm, and gap height,  $W_y$ , equal to 50nm and variable thickness,  $t$ . (b) The dispersion relation for a doped silicon rectangular shell waveguide with plasma resonance around  $3\mu\text{m}$  for  $t = 25, 35$  and  $45\text{nm}$ .

Similar to what has been done with the slot waveguide, the ability to engineer the dispersion curve through varying the doping concentration is demonstrated. Accordingly,

the dispersion curves for materials A, B and C are studied, as illustrated by Figure 5.15. Each material appears to be appropriately tuned to its resonant frequency. The effective modal index found by the simulation at the plasma resonance is in the order of  $10^6$ . On the whole, the material with the least amount of doping hosts the largest modal effective indices throughout the mid-IR spectrum. This is evidenced by material C which has the highest effective index values, followed by material B, then material A.

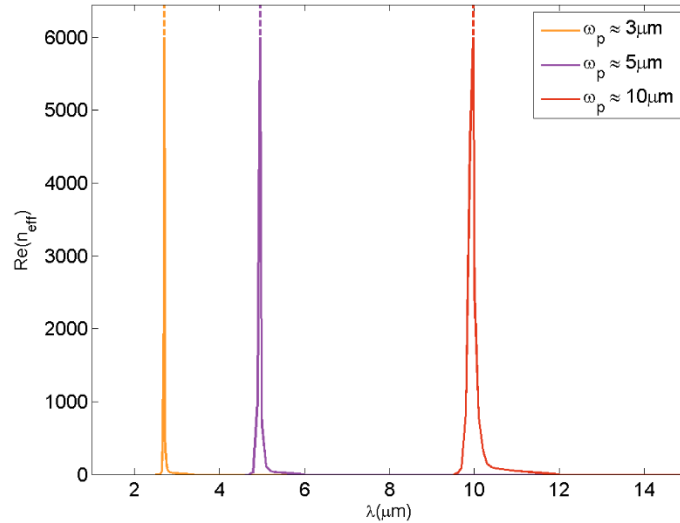


Figure 5.15. Dispersion relations for the 30 x 50nm rectangular shell waveguide for three different doping concentrations.

As mentioned previously, the 2D confinement that is intrinsic to the rectangular shell waveguide is ideal for confining gases under test while maximizing its overlap with the incident light. We tested this by filling the center of a 25nm-thick, 30 x 50nm rectangular shell waveguide, based on material C, with hypothetical substances that have effective indices equal to 1.25 and 1.5, as shown in Figure 5.16. The dispersion of the rectangular shell waveguide filled with a material that has a 1.25 refractive index is red-shifted by 260nm from the air-filled rectangular shell. Alternatively, the dispersion of the waveguide filled with a material that has a 1.5 refractive index is red-shifted by 530nm from the air-filled rectangular shell. Hence, we can quantify the potential for using the rectangular waveguide for sensing as we have in Section III, which would give an average response to the change in the surrounding environment of 1040nm/RIU. This inherent sensitivity property eliminates the need for using expensive fluorescent markers, and allows for label-free sensing mechanisms [28]. The small dimensions of the inner shell also imply that only

a small volume of the sample is needed to perform an effective analysis, hence, reducing the cost of the sensing procedure.

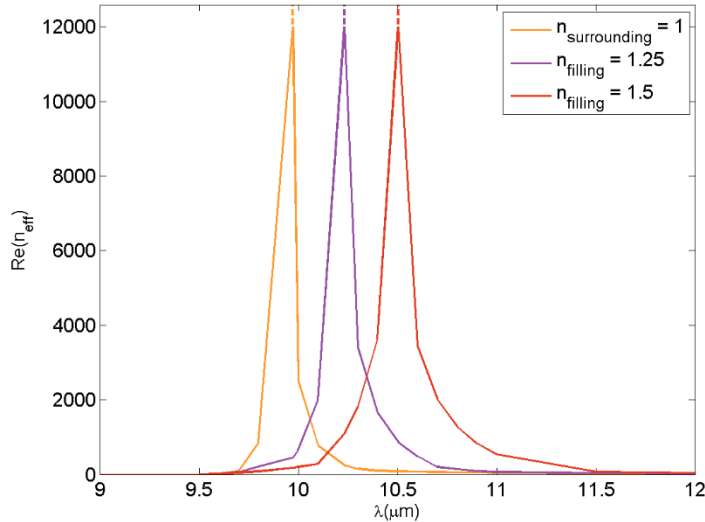


Figure 5.16. The dispersion relations for the rectangular shell waveguide using doped silicon with plasma resonance around  $10\mu\text{m}$  with fillings of  $n = 1, 1.25$  and  $1.5$ .

## 5.4 Doped Silicon SIS Waveguide

\*Portions of this section were done in collaboration with Ms. Sarah Shafaay.

The dispersion properties of an infinitely wide plasmonic gap, or an SIS waveguide is studied and interrogated for potential applications. The SIS waveguide will be based on material A. The general architecture of the structure of interest is shown in Figure 5.17, which illustrates a doped silicon slot waveguide on a substrate layer.

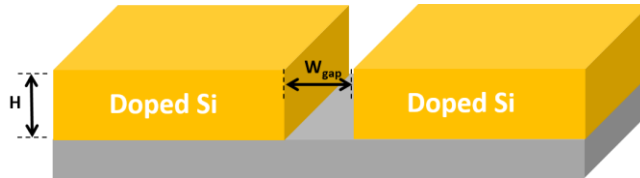


Figure 5.17. SIS structure using doped silicon, where  $H$  is the slot height and  $W_{gap}$  is the gap width of the slot.

We used 2D modal simulations to draw the dispersion curves. It is assumed that the rib width extends to infinity, so for that reason, PML conditions are enforced on the waveguide. The step size of the mesh was set to 1nm. These parameters are used for all modal simulations in section 5.4. Figure 5.18 shows the dispersion of a doped silicon SIS

waveguide with a 200nm gap, and a 20nm thickness. The real part of the effective refractive index is plotted against the wavelength,  $\lambda$ . Details of the dispersion curve are provided in Figure 5.19, which shows a zoomed-in version of the dispersion of the plasmonic region. As expected the plasma resonance is around  $2.7\mu\text{m}$ . Moreover, the dispersion shows four regions: Region 1 ( $\lambda < 2.2\mu\text{m}$ ) a radiative region; Region 2 ( $2.2\mu\text{m} < \lambda < 2.5\mu\text{m}$ ) is a cut-off region; Region 3 ( $2.5\mu\text{m} < \lambda < 2.7\mu\text{m}$ ) is the negative-dispersion region; Region 4 ( $\lambda > 2.7\mu\text{m}$ ) is the plasmonic region. The modal profile for regions 3 and 4 is depicted in the insets of Figure 5.18. Region 1 cannot be utilized as it only supports radiative modes. Region 2 be used for epsilon-near-zero applications such as extraordinary transmission [54], [58]. Region 3 can be used for metamaterial applications, or negative-dispersion applications such as fast and backwards light [113], [114]. Region 4 is the where the plasmonic regimen takes place; we are going to focus on this region throughout the remainder of this paper. In addition, the region around the plasma resonance exhibits a very high effective refractive index, and can therefore be used for slow light applications [46].

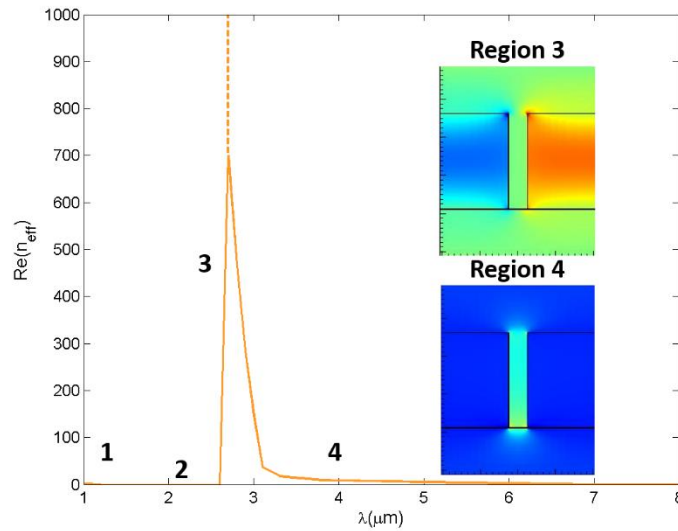


Figure 5.18. Dispersion of SIS doped silicon waveguide showing the real part of the effective refractive index against the wavelength. There are 4 regions: 1. Radiative region. 2. Cut-off region. 3. Negative-dispersion region. 4. Plasmonic region. The modal profile for each region is shown in the insets.

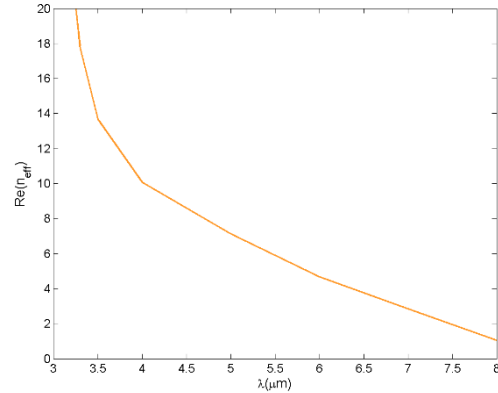


Figure 5.19. Dispersion of an SIS doped silicon waveguide showing the plasmonic region.

The effect of varying the height,  $H$ , and the slot gap width,  $W_{gap}$ , is studied. Figure 5.20 shows the dispersion of a doped silicon SIS waveguide with a gap width equal to 100nm, and three different heights, namely, 20, 50 and 100nm. Figure 5.21, on the other hand, shows the dispersion of a 200nm-wide doped silicon SIS waveguide. Figure 5.22, shows the dispersion of a 1 $\mu$ m-gap doped silicon SIS waveguide. Both figures employ the same heights as Figure 5.20. It can be seen that the effective refractive index is significantly higher for a smaller gap width. Alternatively, a smaller height results in a mildly larger effective refractive index, and also a generally less steep curve. These results are intuitive as it is expected of smaller gaps to confine the light better, hence, resulting in a larger effective refractive index.

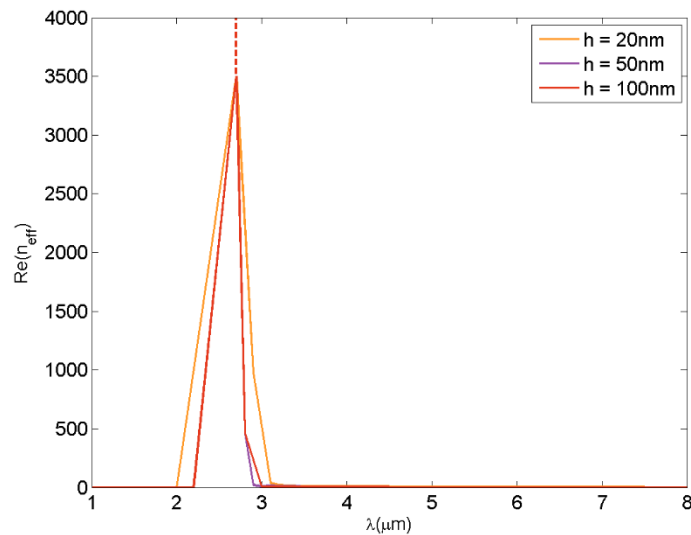


Figure 5.20. Dispersion of SIS doped silicon waveguide showing the real part of the effective refractive index against the wavelength for a 100nm gap and heights of 20, 50, and 100nm.

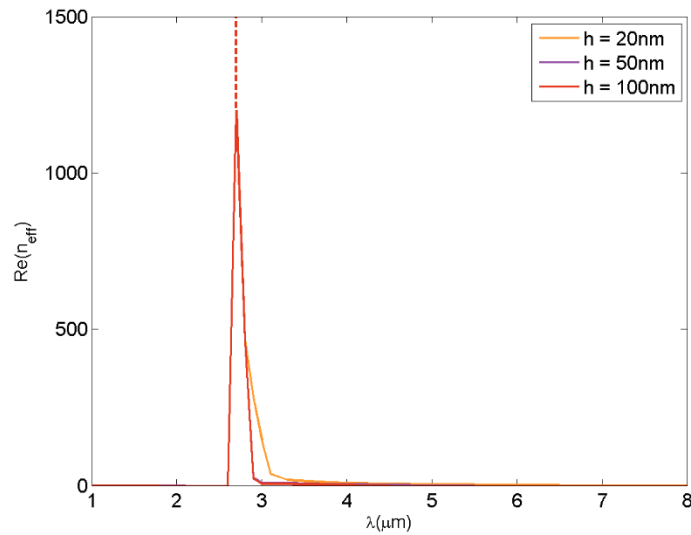


Figure 5.21. Dispersion of an SIS doped silicon waveguide showing the real part of the effective refractive index against the wavelength for a 200nm gap and heights of 20, 50, and 100nm.

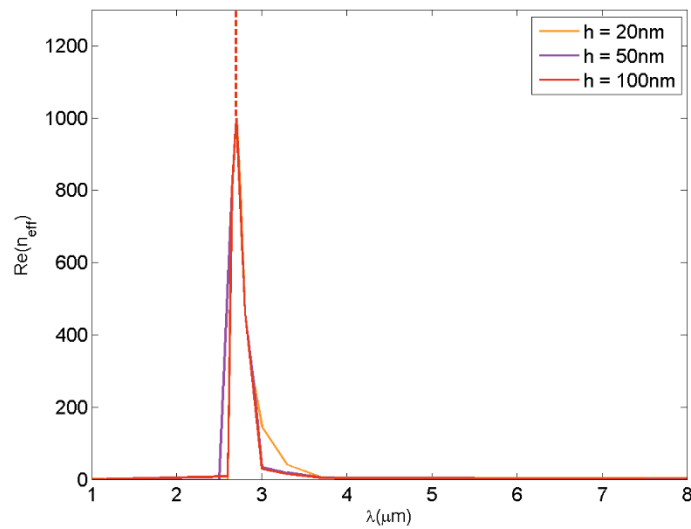


Figure 5.22. Dispersion of an SIS doped silicon waveguide showing the real part of the effective refractive index against the wavelength for a 1 $\mu$ m gap and heights of 20, 50, and 100nm.

The SIS structure can be used to create sharp bends, junctions or splitters. In the following sub-sections, we will study the behavior of 90 degree bends, as well as T-junction and X-junction splitters using material A doped silicon. However, we first need to confirm that the light can survive for long distances within an infinitely wide SIS structure. Hence, using the 2D FDTD engine provided by Optiwave, we were able to confirm the modal confinement in a material AN SIS waveguide as shown in Figure 5.23. PML boundary

conditions were used. The mesh size was 0.1nm in the x- directions, and 0.4 $\mu$ m in the y and z-directions. The simulations time was 16000 time steps, with each time step equal to approximately  $10^{-7}$ . The mode was excited at 3 $\mu$ m and is shown to propagate for 10 $\mu$ m for the 5nm gap, 25nm gap, 50nm gap, and 100nm gap SIS waveguide and displayed very high localization.

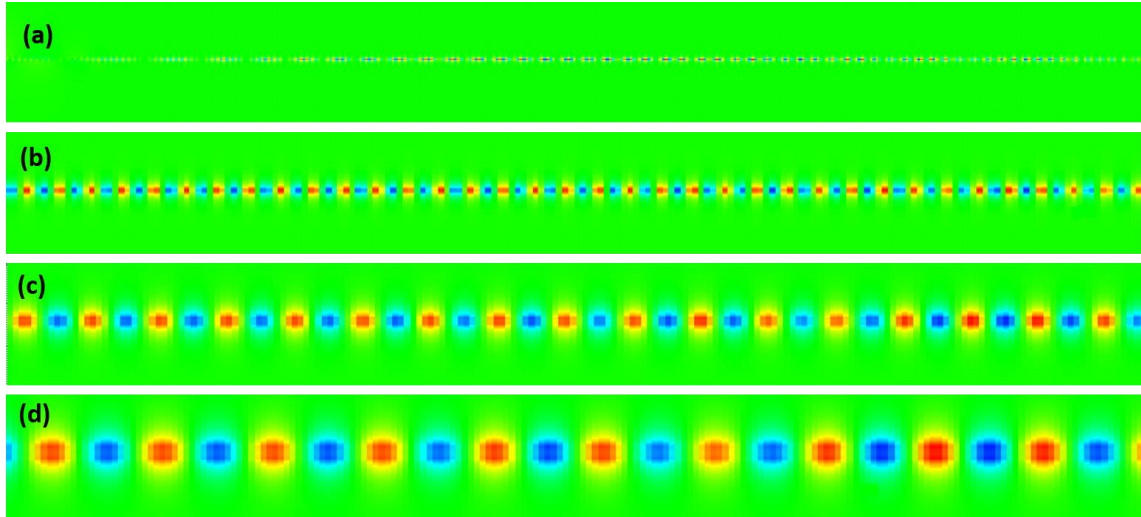


Figure 5.23. 2D FDTD simulation showing the propagation of 5 $\mu$ m signal through 10 $\mu$ m long slot waveguides with: (a) 5nm gap, (b) 25nm gap, (c) 50nm gap and (d) 100nm gap.

### 5.4.1 90 Degree Bends

Sharp bends are highly desirable in CMOS integrated circuits; however, due to diffraction limits, it is nearly impossible to confine light in 90 degree bends based on pure silicon. Plasmonic devices are known for their excellent ability to transmit light through sharp bends, but are challenging to integrate with CMOS devices. Since it possesses plasmonic behavior, and can also be fabricated using standard technology, doped silicon may be a solution for creating sharp bends in the mid-IR frequencies. Using 2D FDTD simulations, we tested the transmission through a 100nm-wide 90 degree bend (modal profile of the bend is shown in the inset of Figure 5.24) using doped silicon for the 3 to 10 $\mu$ m range. The Lumerical software was used for this purpose. The mesh size was 1nm for all directions. PML boundary conditions were invoked. These simulation parameters were used for all the subsequent 2D and 3D FDTD simulations in this section. In order to separate the effect of introducing the bend to the waveguide from the effect of propagation losses, the reflection and transmission monitors where placed fairly close to the source. As shown in Figure 5.24, the transmission is perfect at 100%, and there is no reflection.

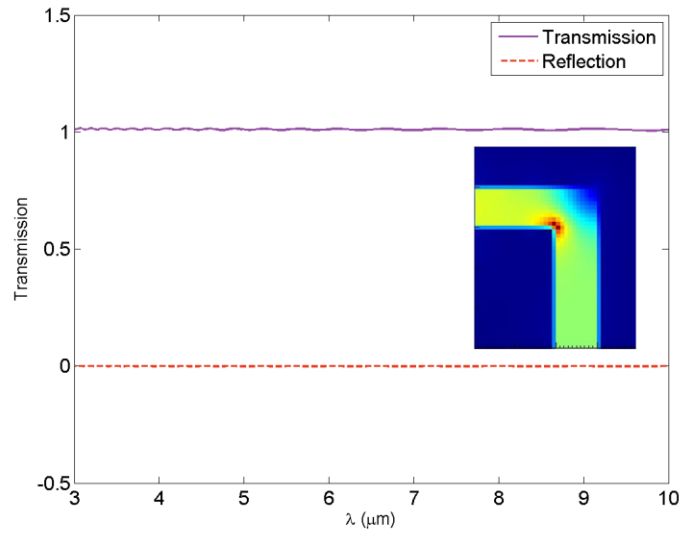


Figure 5.24. Transmission through a 100nm gap 90 degree bend. Inset shows the propagation profile within the bend.

### 5.4.2 T-Junction Splitters

Following the same mindset, we tested the performance of a T-junction splitter with a 100nm gap, the modal profile of which is shown in Figure 5.25(b). As shown in Figure 5.25(a), the transmission in the two arms is identical and is around 40%. This is in good agreement with the performance of silver in the NIR frequencies as demonstrated by [115].

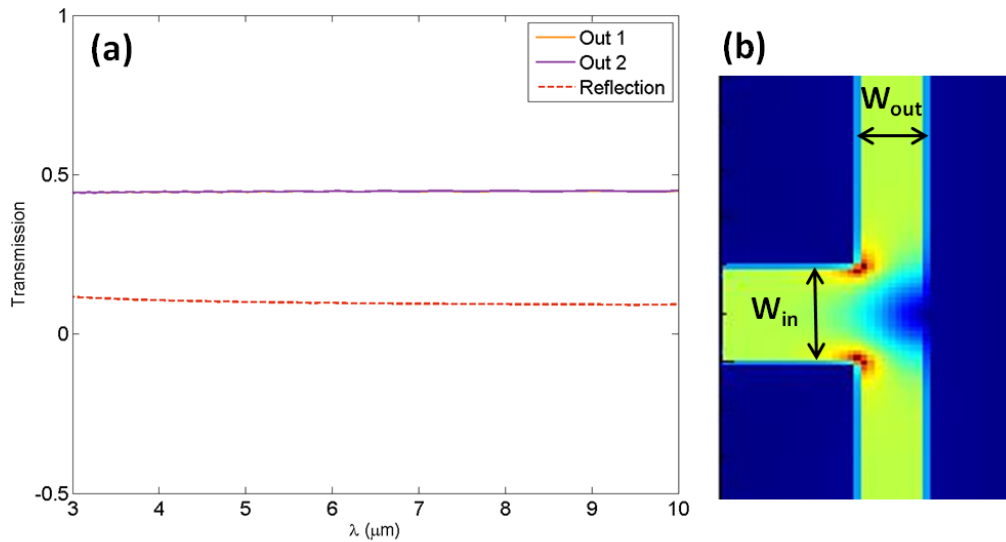


Figure 5.25. (a) Transmission spectrum of a 100nm doped Si t-junction splitter. (b) Propagation profile of a doped Si t-junction splitter.



It was also shown in [115] that it is possible to eliminate reflection by matching the impedance between the input and output arms. This is done by setting the width of the input arm to be around twice the width of the output arms. We tried testing this using doped silicon in the 3 to 10 $\mu\text{m}$  range, with the width of the input arm at 200nm, while the output arms were kept at 100nm. The transmission spectrum is shown in Figure 5.26; as expected, there is nearly no reflection, and the transmission from the two arms is around 50%.

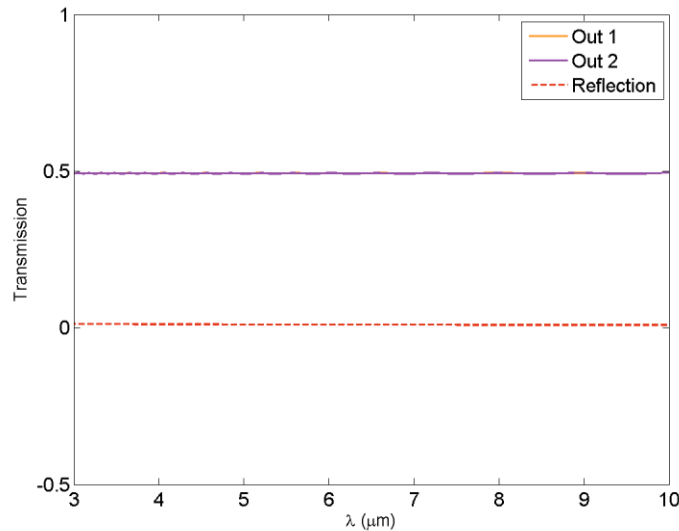


Figure 5.26. Transmission spectrum of a doped Si t-junction splitter with a 200nm wide input arm and 100nm wide output arms.

### 5.4.3 X-Junction Splitters

We studied the performance of an x-junction splitter, the modal profile of which is shown in Figure 5.27(b). First, we studied the performance of a 100nm X-junction splitter. The results, shown in Figure 5.27(a), depict around 25% transmission for all output arms, and 25% reflection. The deviation between the vertical (1, 2) and horizontal (3) output arms is less than 1%.

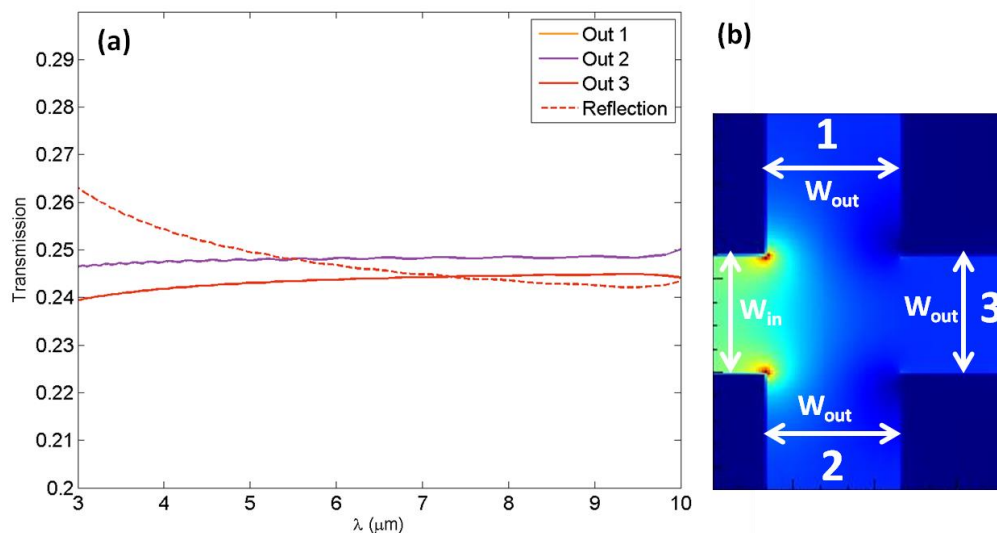


Figure 5.27. (a) Transmission spectrum of a 100nm gap doped Si x-junction splitter. (b) Propagation profile of a doped Si x-junction splitter.

Similar to what has been done with the T-junction, we optimized the X-junction by tripling the width of the width of the input waveguide, so that the reflection is minimized. As shown in Figure 5.28, the transmission was increased to 34% in two arms (Out 1, Out 2) and to 28.5% in the third arm (Out 3).

We were also interested in studying the effect of increasing the width of all arms, to see when the power splitting ratio would fail. We define a deviation of more than 15% in the transmitted power between the vertical and horizontal arms as a failure in power splitting. Such deviation was not visible until the arms were increased to  $2\mu\text{m}$ . Figure 5.29 shows that for a gap width as large as  $1\mu\text{m}$ , the deviation between vertical (Out 1, Out 2) and horizontal (Out 3) arms is just below 1%. On the other hand, when the width was increased to  $2\mu\text{m}$ , the transmission spectrum, shown in Figure 5.30, showed a deviation of at least 15% between the vertical and horizontal arms in the 3 to  $5\mu\text{m}$  range. This is a vast improvement over the performance of traditional plasmonics in the visible and NIR range, which can maintain a good ratio of power splitting between the arms for gap widths of only 200nm and below.

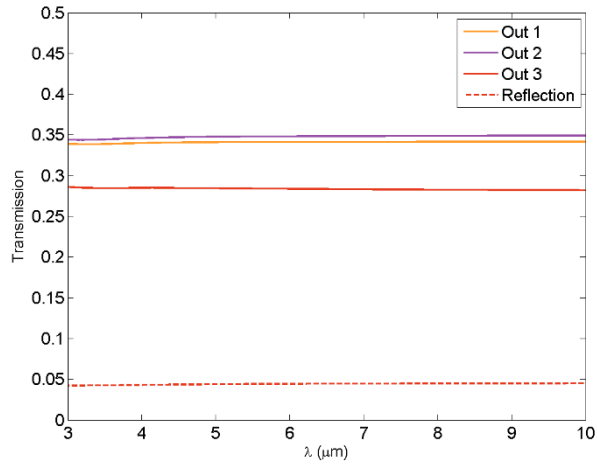


Figure 5.28. Transmission spectrum of a 100nm gap doped Si x-junction splitter with a 300nm-wide input arm and 100nm-wide output arms.

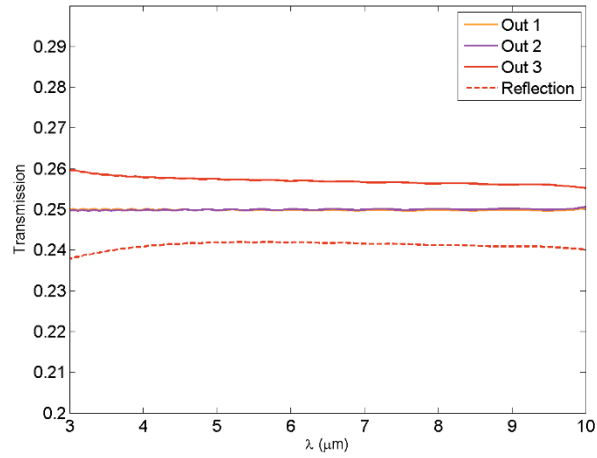


Figure 5.29. Transmission spectrum of an x-junction splitter with a 1μm-wide gap.

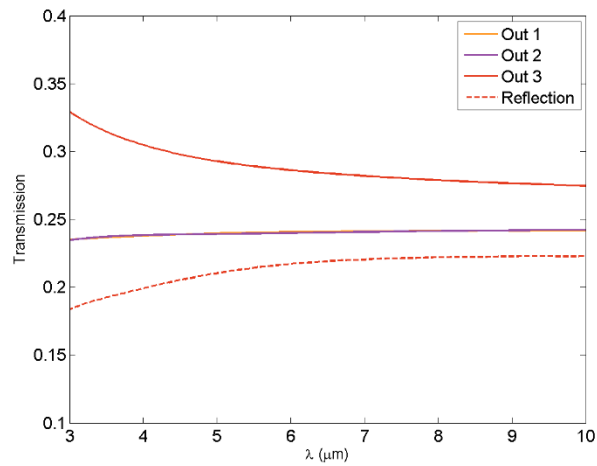


Figure 5.30. Transmission spectrum of an x-junction splitter with a 2μm-wide gap.

### 5.4.4 Propagation Losses in SIS Waveguides

As mentioned before, the monitors for the previous simulations were placed quite close to the bends, so as to not account for propagation losses, however it is necessary to understand how losses affect the performance of the waveguide. That said, the purpose of this section is to study the propagation losses in a straight SIS waveguide using 3D FDTD simulations. Ten pulses with wavelengths from 1 to  $10\mu\text{m}$  were propagated separately along a  $1\mu\text{m}$ -long doped silicon SIS waveguide. The simulations were conducted once for an SIS waveguide with a 100nm-wide gap, and again for a waveguide with a 200nm-wide gap. The waveguide was 600nm-thick, and was placed on top of an infinitely thick sapphire substrate. Sapphire was used instead of silicon dioxide for its transparency in the mid-IR range [116]. The losses are plotted in dB/cm for each wavelength in Figure 5.31. The losses generally appear to be quite high, but are maximum at  $3\mu\text{m}$ , which is near the plasma resonance of our doped silicon material. Interestingly, the losses for the 200nm-wide gap are steadily smaller than those for the 100nm-wide gap, except near the resonance at  $3\mu\text{m}$ . This may be because the effective refractive index of smaller gaps tends to be larger than that of larger gaps near the resonance (see Figure 5.20 - Figure 5.22). A high effective refractive index could imply high confinement, which implies a high penetration depth within the doped silicon, indicating the possibility of high losses.

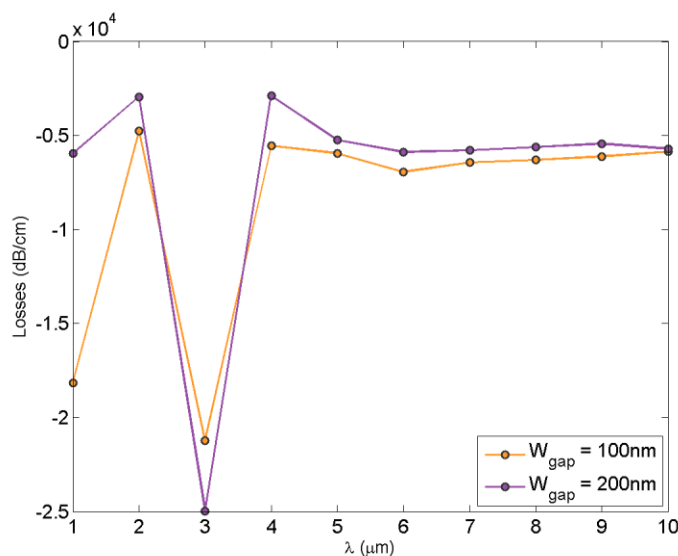


Figure 5.31. Propagation losses for a  $1\mu\text{m}$ -long SIS waveguide with a 100nm-wide gap and a 200nm-wide gap.

## 5.5 Doped Silicon Nanoparticles

As discussed in Section 4.1.3.4, plasmonic nanoparticles are viable candidates for chemical and biological sensing applications due to their large scattering and absorption cross-sections when excited by an electromagnetic source at their plasma resonance [68]. Their enhanced absorption and scattering has landed them applications in biomedical imaging [74], [75], therapeutics [75], [76], and sensing [77], [78]. Generally, the sensitivity of a nanoparticle or nanorod is defined as a shift in the peak of the scattering or absorption cross-section due to changes in the surrounding environment [79]. Here, we devise a mid-IR sensor using doped silicon in the form of a nanodisk with a 100nm radius. Using 2D FDTD simulations, a total-field scattered-field source with a wavelength centered around  $3\mu\text{m}$  (near the plasma resonance) is used to excite the nanoparticle. The mesh size was 1nm. The sensitivity of the nanodisk was evaluated by changing the refractive index of the surrounding environment while calculating the extinction cross-section (absorption + scattering). The refractive index change introduced to the environment was made in 0.25 increments as shown in Figure 5.32. When the nanodisk is surrounded by air, the resonance of the extinction cross-section is around  $2.7\mu\text{m}$ , which is the plasma resonance. The extinction cross-section appears to increase by approximately 300nm for a 0.25 increase in the surrounding refractive index. The sensitivity, on the other hand, appears to be around 310nm/RIU. Note that nanospheres inherently have higher sensitivities than nanodisks due to their larger area. Consequently high-aspect-ratio nanorods have an even higher sensitivity than both, as the sensitivity has been shown to be directly proportional to the nanorod aspect ratio [79]. Keeping that in mind, the value we obtained for sensitivity in comparison to the sensitivities of some nanospheres from recent literature [117], [118] is quiet decent. Note that 3D FDTD nanospheres simulations were not conducted due to the lack of availability of the necessary computational resources.

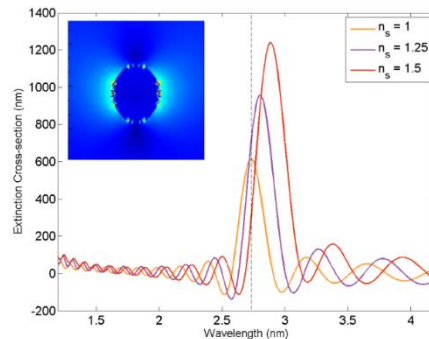


Figure 5.32. Nanodisk sensor based on doped silicon with plasma resonance at  $3\mu\text{m}$ , with surrounding refractive index,  $n = 1, 1.25$  and  $1.5$ . Inset shows the mode profile at  $3\mu\text{m}$ .

# Chapter 6: Conclusion

Two novel waveguides based on silicon photonics were carefully studied and analyzed. With regards to the viability of silicon photonics, the verdict is simple: silicon photonics are excellent light-guiding mediums. Besides the obvious CMOS compatibility privileges it offers, silicon proved to be an excellent manipulator of light over a wide range of frequencies, while being able to operate using the photonic and the plasmonic regimen. Perhaps no other material is as flexible in terms of design as is silicon. This flexibility allowed us to design nanometer materials and highly-doped materials that can provide new and unusual functionalities, such as ENZ operation and non-evanescent field sensing.

In our first work—the SNRW bimodal sensor—we were able to design a robust, label-free optical biosensor. The SNRW is generally provided as a basic element that can be used to build different sensing configurations. Recall the introduction of this dissertation: there were 3 design challenges/goals for the SNRW. Using our simulations, we showed that: 1) light can be confined and propagated for distances as long as  $10\mu\text{m}$ , with hardly any losses, using the SNRW. Also, the low-thickness region in the SNRW confines the evanescent tail and ensures that none of the light power is wasted. 2) Modal simulations demonstrated that the SNRW could detect changes in the surrounding environment as small as  $10^{-8}$ . Furthermore, the SNRW structure is about 170 times more sensitive to changes in the surrounding environment than the conventional BSRW. More importantly, it displayed a sensitivity higher than that of similar non-evanescent field sensors (structures that are capable of guiding light in low-index media), such as SOI gratings and rib nanowires waveguides—even though the latter demonstrated very competitive performance. However, the edge of the SNRW is not limited to its reaction to its surroundings. This brings us to our third design goal: c) the SNRW demonstrated a much-desired spatial flexibility in that it allows single-mode operation using relatively large dimensions. This high spatial tolerance for single-mode operation is not found in rib nanowires. Also, the inherently larger dimensions of the SNRW makes it easier to fabricate.

The effectiveness of the SNRW was verified when it was tested as a sensor using the bimodal configuration. The bimodal configuration is extremely elegant in that it has a simple, straight-forward design that does not call for bends, junctions, or complex coupling mechanisms. Such complications usually cause power leakage and are more challenging to fabricate. The compact nature of the bimodal waveguide makes it an excellent candidate for on-chip integration. By applying the SNRW to the bimodal waveguide, a very high

sensitivity at 300nm/RIU was achieved. The sensitivity itself is comparable to previously reported sensitivities, but the SFR is much larger for the SNRW bimodal sensor, thanks to the small-footprint of the bimodal waveguide.

Many directions could be taken with the bimodal SNRW. Perhaps, as a long-term goal, the SNRW could be used as a sensor in a truly portable lab-on-a-chip device. Creating such a device would require collaborations with VLSI engineers, who may design the electronic read-out circuitry, and nanotechnology experts, who can design the microfluidic channels needed for sample extraction and delivery, and the device packaging. A suitable micro-fluidic channel could be perpendicular to the SNRW, so that it injects the sample across the width of the nanowires. Aside from the electronics and microfluidics, it would also be necessary to collaborate with biochemists/biophysicists who can provide insight into suitable immobilization mechanisms. However, these are the long-term goals. Much more modest, but nonetheless, urgent and necessary goals, include the fabrication and testing of the bimodal SNRWs. For instance, in our simulations, we performed the sensing characterization by varying the refractive index of the surrounding medium. In a real-life scenario, there would never be a single-refractive index around the waveguide, but rather, a much more complex anisotropic fluid. Taking these real-world imperfections into account will direct us on how to improve and optimize our device.

In our second design, we show that through the doping of silicon, it is transformed from a dielectric material to a plasmonic material with resonance in the mid-infrared region. We were able to design highly confined plasmonic modes through the use of several structures, such as slots, SIS waveguides and rectangular-shell waveguides. The properties of our doped silicon waveguide can be heavily manipulated, as the dispersion curves may be engineered to resonate at a wavelength of our choice by selecting the appropriate doping concentration. It was also shown that the gap width, rather than the rib width, of slot structures is primarily responsible for modal effective index fluctuations. Therefore, making it a crucial design tool for applications that require a very high effective index such as slow light. The spectral vicinity of the plasma resonance of the doped silicon in the mid-infrared provides the opportunity for a host of important applications such as negative-index applications, epsilon-near-zero applications such as extraordinary transmission, and slow and backwards light applications. For instance, we proved through simulations that our doped silicon slot waveguide can work as a slow-light medium. Up until recently, most of these innovative applications were only possible through the use of meta-materials which are very challenging to design and fabricate.

With regards to the prospect of building mid-IR sensors based on doped silicon waveguide, it was discovered that the slot and rectangular structure show great promise for sensing applications in the mid-IR. Their dispersion curves respond strongly to changes in the environment with wavelength shifts as high as 1050nm/RIU. In addition, the 1D and 2D analyte confinement provided by the slot waveguide and the rectangular waveguide, respectively, make these structures ideal for sensing applications. The nanodisk can also be an effective mid-IR sensor, with sensitivity averaging values as high as 300nm/RIU. The sensitivity for the doped silicon nanodisk is superior to the recently reported sensitivities of nanospheres. This is a good implication that the sensitivity for the doped silicon nanosphere would be much larger than prior art nanospheres.

Aside from sensing, using the SIS waveguide, we were able to map plasmonic characteristics depicted by noble metals in the NIR to the mid-IR. This was one of our primary goals, as it opens the door to CMOS-compatible, on-chip plasmonic devices. We tested some common light-manipulating sub-wavelength plasmonic structures that may be used in mid-IR optoelectronic circuits. These structures included 90-degree bends, T-splitters and X-splitters. As a result, we were able to obtain transmission spectra that were very much like the ones produced by noble-metals in the NIR. The only difference, perhaps, is that the doped silicon SIS waveguide can operate with a higher efficiency for much larger plasmonic gaps.

As is the case with highly-confined plasmonics, our doped silicon waveguide tends to suffer from a lot of losses near its plasma resonance as was shown by our 3D simulations. In order to fully understand the scale of the losses, it is important to fabricate and characterize the waveguide based on experimental facts. But perhaps the main contribution of our work is that we provided fellow scientists and engineers a detailed operational profile on a doped silicon waveguide that has the potential for being used in all sorts of mid-IR applications.



# Publications

## Submitted

1. Rania Gamal, Yehea Ismail, and Mohamed Swillam, "Optical biosensor based on a silicon nanowire ridge waveguide," *submitted for publication in Photonics West 2015*, July 2014.
2. Rania Gamal, Sarah Shafaay, Yehea Ismail, and Mohamed Swillam, "Nanoscale confinement using dielectric waveguides at the Mid-infrared region," *submitted for publication in Photonics West 2015*, July 2014.
3. Rania Gamal, Yehea Ismail, and Mohamed Swillam, "Nanoscale confinement of silicon slot Waveguides in the mid-infrared," *submitted for publication in the Journal of Lightwave Technology*, August 2014.
4. Rania Gamal, Yehea Ismail, and Mohamed Swillam, "Bimodal optical biosensor based on a silicon nanowire ridge waveguide," *submitted for publication in the Journal of Nanophotonics*, August 2014.

## Under Submission

1. Rania Gamal, Sarah Shafaay, Yehea Ismail, and Mohamed Swillam, "Silicon-insulator-silicon mid-infrared plasmonics." In preparation.

# References

- [1] G. T. Reed, and A. P. Knights, *Silicon photonics: an introduction*, West Sussex: John Wiley & Sons, 2004.
- [2] M. Khorasaninejad, and S. S. Saini, "Silicon nanowire optical waveguide (SNOW)," *Optics express*, vol. 18, no. 22, pp. 23442-23457, 2010.
- [3] S. Balslev, A. M. Jorgensen, B. Bilenberg, K. B. Mogensen, D. Snakenborg, O. Geschke, J. P. Kutter, and A. Kristensen, "Lab-on-a-chip with integrated optical transducers," *Lab on a Chip*, vol. 6, no. 2, pp. 213-217, 2006.
- [4] D. Mark, S. Haeberle, G. Roth, F. V. Stetten, and R. Zengerle, "Microfluidic lab-on-a-chip platforms: requirements, characteristics and applications," *Chemical Society Reviews*, vol. 39, no. 3 (2010): 1153-1182.
- [5] Z. H. Fan, and D. J. Harrison, "Micromachining of capillary electrophoresis injectors and separators on glass chips and evaluation of flow at capillary intersections," *Analytical Chemistry*, vol. 66, no. 1, pp. 177-184, 1994.
- [6] J. Noh, H. Kim, and T. Chung, "Biosensors in Microfluidic Chips," *Microfluidics*, pp. 117-152, 2011.
- [7] M. C. Estevez, M. Alvarez, and L. M. Lechuga, "Integrated optical devices for lab-on-a-chip biosensing applications," *Laser & Photonics Reviews*, 2012.
- [8] F. J. Blanco, M. Agirregabiria, J. Berganzo, K. Mayora, J. Elizalde, A. Calle, C. Domínguez, and L. M. Lechuga, "Microfluidic-optical integrated CMOS-compatible devices for label-free biochemical sensing," *Journal of Micromechanics and Microengineering*, vol. 16, no. 5, pp. 1006, 2006.
- [9] V. Passaro, F. Dell'Olio, B. Casamassima, and F. D. Leonardis, "Guided-wave optical biosensors," *Sensors*, vol. 7, no. 4, pp. 508-536, 2007.
- [10] R. G. Heideman, R. P. H. Kooyman, and J. Greve, "Performance of a highly sensitive optical waveguide Mach-Zehnder interferometer immunosensor," *Sensors and Actuators B: Chemical*, vol. 10, no. 3, pp. 209-217, 1993.
- [11] B. J. Luff, J. S. Wilkinson, J. Piehler, U. Hollenbach, J. Ingenhoff, and N. Fabricius, "Integrated optical mach-zehnder biosensor," *Journal of lightwave technology*, vol. 16, no. 4, pp. 583, 1998.

- [12] B. Sepulveda, J. S. D. Rio, M. Moreno, F. J. Blanco, K. Mayora, C. Domínguez, and L. M. Lechuga, "Optical biosensor microsystems based on the integration of highly sensitive Mach–Zehnder interferometer devices," *Journal of optics A: pure and applied optics*, vol. 8, no. 7, pp. S561, 2006.
- [13] M. Weisser, G. Tovar, S. Mittler-Neher, W. Knoll, F. Brosinger, H. Freimuth, M. Lacher, and W. Ehrfeld, "Specific bio-recognition reactions observed with an integrated Mach–Zehnder interferometer," *Biosensors and Bioelectronics*, vol. 14, no. 4, pp. 405-411, 1999.
- [14] K. E. Zinoviev, A. B. González-Guerrero, C. Domínguez, and L. M. Lechuga, "Integrated bimodal waveguide interferometric biosensor for label-free analysis," *Journal of Lightwave Technology*, vol. 29, no. 13, pp. 1926-1930, 2011.
- [15] D. Duval, A. B. González-Guerrero, S. Dante, J. Osmond, R. Monge, L. J. Fernández, K. E. Zinoviev, C. Domínguez, and L. M. Lechuga, "Nanophotonic lab-on-a-chip platforms including novel bimodal interferometers, microfluidics and grating couplers," *Lab on a Chip*, vol. 12, no. 11, pp. 1987-1994, 2012.
- [16] D. Duval, L. M. Lechuga, and A. B. Gonzalez, "Silicon Photonic Based Biosensors: The Future of Lab-on-a-Chip Diagnostic Devices," *IEEE Photonics Society*, vol. 26, no. 4, 2012.
- [17] W. Lukosz, and K. Tiefenthaler, "Sensitivity of integrated optical grating and prism couplers as (bio) chemical sensors," *Sensors and Actuators*, vol. 15, no. 3, pp. 273-284, 1988.
- [18] P. M. Nellen, K. Tiefenthaler, and W. Lukosz, "Integrated optical input grating couplers as biochemical sensors," *Sensors and Actuators*, vol. 15, no. 3, pp. 285-295, 1988.
- [19] J. Vörös, J. J. Ramsden, G. Csucs, I. Szendrő, S. M. De Paul, M. Textor, and N. D. Spencer, "Optical grating coupler biosensors," *Biomaterials*, vol. 23, no. 17, pp. 3699-3710, 2002.
- [20] A. Ksendzov, and Y. Lin, "Integrated optics ring-resonator sensors for protein detection," *Optics letters*, vol. 30, no. 24, pp. 3344-3346, 2005.
- [21] M. White, H. Oveys, and X. Fan, "Liquid-core optical ring-resonator sensors," *Optics Letters*, vol. 31, no. 9, pp. 1319-1321, 2006.
- [22] M. Sumetsky, R. S. Windeler, Y. Dulashko, and X. Fan, "Optical liquid ring resonator sensor," *Optics Express*, vol. 15, no. 22, pp. 14376-14381, 2007.
- [23] D. Vos, Katrien, I. Bartolozzi, E. Schacht, P. Bienstman, and R. Baets, "Silicon-on-Insulator microring resonator for sensitive and label-free biosensing," *Optics express*, vol. 15, no. 12, pp. 7610-7615, 2007.

- [24] X. Fan, I. M. White, H. Zhu, J. D. Suter, and H. Oveys, "Overview of novel integrated optical ring resonator bio/chemical sensors," In *Proc. SPIE*, vol. 6452, p. 64520M, 2007.
- [25] H. Zhu, I. M. White, J. D. Suter, P. S. Dale, and X. Fan, "Analysis of biomolecule detection with optofluidic ring resonator sensors," *Optics Express*, vol. 15, no. 15, pp. 9139-9146, 2007.
- [26] V. R. Almeida, Q. Xu, C. A. Barrios, and M. Lipson, "Guiding and confining light in void nanostructure," *Optics letters*, vol. 29, no. 11, pp. 1209-1211, 2004.
- [27] C. A. Barrios, K. B. Gylfason, B. Sánchez, A. Griol, H. Sohlström, M. Holgado, and R. Casquel, "Slot-waveguide biochemical sensor," *Optics letters*, vol. 32, no. 21, pp. 3080-3082, 2007.
- [28] T. Claes, J. G. Molera, K. D. Vos, E. Schachtb, R. Baets, and P. Bienstman, "Label-free biosensing with a slot-waveguide-based ring resonator in silicon on insulator," *Photonics Journal, IEEE*, vol. 1, no. 3, pp. 197-204, 2009.
- [29] Q. Xu, V. R. Almeida, R. R. Panepucci, and M. Lipson, "Experimental demonstration of guiding and confining light in nanometer-size low-refractive-index material," *Optics letters*, vol. 29, no.14, pp. 1626-1628, 2004.
- [30] H. Sun, A. Chen, and L. R. Dalton, "Enhanced evanescent confinement in multiple-slot waveguides and its application in biochemical sensing," *Photonics Journal, IEEE*, vol. 1, no. 1, pp. 48-57, 2009.
- [31] C. A. Barrios, "Optical slot-waveguide based biochemical sensors," *Sensors*, vol. 9, no. 6, pp. 4751-4765, 2009.
- [32] M. Khorasaninejad, N. Clarke, M. P. Anantram, and S. S. Saini, "Optical biochemical sensors on SNOW ring resonators," *Optics Express*, vol. 19, no. 18, pp. 17575-17584, 2011.
- [33] K. Yee, "Numerical solution of initial boundary value problems involving Maxwell's equations in isotropic media," *IEEE Transactions on Antennas and Propagation*, vol. 14, no. 3, pp. 302-307, 1966.
- [34] Optiwave Systems Inc., "OptiFDTD: Technical Background and Tutorials," 2011.
- [35] R. Courant, K. Friedrichs, and H. Lewy, "Über die partiellen Differenzgleichungen der mathematischen Physik," *Mathematische Annalen*, vol. 100, no .1, pp. 32-74, 1928.
- [36] Mikhail Polyanskiy, "Refractive Index Info," Internet: <http://refractiveindex.info/>, [30 July 2014].
- [37] H. Zhu, I. M. White, J. D. Suter, P. S. Dale, and X. Fan, "Analysis of biomolecule detection with optofluidic ring resonator sensors," *Optics Express*, vol. 15, no. 15, pp. 9139-9146, 2007.

- [38] S. A. Maier. *Plasmonics: Fundamentals and Applications: Fundamentals and Applications*. New York: Springer, 2007.
- [39] A. Arsenault, S. Fournier-Bidoz, B. Hatton, H. Miguez, N. Tétreault, E. Vekris, S. Wong, S. M. Yang, V. Kitaev, and G. A. Ozin, "Towards the synthetic all-optical computer: science fiction or reality?," *Journal of Materials Chemistry*, vol. 14, no. 5, pp. 781-794, 2004.
- [40] P. Raghavan, and E. Upfal, "Efficient routing in all-optical networks," *Proceedings of the twenty-sixth annual ACM symposium on Theory of computing*, ACM, 1994.
- [41] B. Beauquier, J.-C. Bermond, L. Gargano, P. Hell, S. Pérennes, and U. Vaccaro, "Graph problems arising from wavelength-routing in all-optical networks," 1997.
- [42] Z. Kang, W. Lin, and G. P. Wang, "Dual-channel broadband slow surface plasmon polaritons in metal gap waveguide superlattices," *JOSA B*, vol. 26, no. 10, pp. 1944-1948, 2009.
- [43] M. Bajcsy, S. Hofferberth, V. Balic, T. Peyronel, M. Hafezi, A. S. Zibrov, V. Vuletic, and M. D. Lukin, "Efficient all-optical switching using slow light within a hollow fiber," *Physical review letters*, vol. 102, no. 20, pp. 203902, 2009.
- [44] H. Wen, M. Terrel, S. Fan, and M. Digonnet, "Sensing with slow light in fiber Bragg gratings," *Sensors Journal, IEEE*, vol. 12, no. 1, pp. 156-163, 2012.
- [45] P. W. Milonni, *Fast light, slow light and left-handed light*, CRC Press, 2010.
- [46] L. Yang, C. Min, and G. Veronis, "Guided subwavelength slow-light mode supported by a plasmonic waveguide system," *Optics letters*, vol. 35, no. 24, pp. 4184-4186, 2010.
- [47] J. Park, K.-Y. Kim, I.-M. Lee, H. Na, S.-Y. Lee, and B. Lee, "Trapping light in plasmonic waveguides," *Optics express*, vol. 18, no. 2, pp. 598-623, 2010.
- [48] C. M. Soukoulis, S. Linden, and M. Wegener, "Negative refractive index at optical wavelengths," *Science*, vol. 315, no. 5808, pp. 47-49, 2007.
- [49] V. M. Shalaev, "Optical negative-index metamaterials," *Nature photonics*, vol. 1, no. 1, pp. 41-48, 2007.
- [50] J. B. Pendry, "Negative refraction makes a perfect lens," *Physical review letters*, vol. 85, no. 18, pp. 3966, 2000.
- [51] A. Alù, and N. Engheta, "Multifrequency optical invisibility cloak with layered plasmonic shells," *Physical review letters*, vol. 100, no. 11, pp. 113901, 2008.
- [52] W. Cai, U. K. Chettiar, A. V. Kildishev, and V. M. Shalaev, "Optical cloaking with metamaterials," *Nature photonics*, vol. 1, no. 4, pp. 224-227, 2007.
- [53] H. A. Bethe, "Theory of diffraction by small holes," *Physical Review*, vol. 66, no. 7-8, pp. 163, 1944.

- [54] T. W. Ebbesen, H. J. Lezec, H. F. Ghaemi, T. Thio, and P. A. Wolff, "Extraordinary optical transmission through sub-wavelength hole arrays," *Nature*, vol. 391, no. 6668, pp. 667-669, 1998.
- [55] R. H. Ritchie, E. T. Arakawa, J. J. Cowan, and R. N. Hamm, "Surface-plasmon resonance effect in grating diffraction," *Physical Review Letters*, vol. 21, no. 22, pp. 1530, 1968.
- [56] L. Martin-Moreno, F. J. Garcia-Vidal, H. J. Lezec, K. M. Pellerin, T. Thio, J. B. Pendry, and T. W. Ebbesen, "Theory of extraordinary optical transmission through subwavelength hole arrays," *Physical review letters*, vol. 86, no. 6, pp.1114, 2001.
- [57] S. G. Rodrigo, "Extraordinary Optical Transmission," *Optical Properties of Nanostructured Metallic Systems*, pp. 37-75, Springer: Berlin Heidelberg, 2012.
- [58] D. C. Adams, S. Inampudi, T. Ribaudo, D. Slocum, S. Vangala, N. A. Kuhta, W. D. Goodhue, V. A. Podolskiy, and D. Wasserman, "Funneling light through a subwavelength aperture with epsilon-near-zero materials," *Physical review letters*, vol. 107, no. 13, pp. 133901, 2011.
- [59] A. Alù, F. Bilotti, N. Engheta, and L. Vegni, "Metamaterial covers over a small aperture," *Antennas and Propagation, IEEE Transactions*, vol. 54, no. 6, pp. 1632-1643, 2006.
- [60] Y. Jin, P. Zhang, and S. He, "Abnormal enhancement of electric field inside a thin permittivity-near-zero object in free space," *Physical Review B*, vol. 82, no. 7, pp. 075118, 2010.
- [61] J. Homola, Sinclair S. Yee, and G. Gauglitz, "Surface plasmon resonance sensors: review," *Sensors and Actuators B: Chemical*, vol. 54, no. 1, pp. 3-15.
- [62] J. Homola, "Present and future of surface plasmon resonance biosensors," *Analytical and bioanalytical chemistry*, vol. 377, no. 3, pp. 528-539, 2003.
- [63] K. Matsubara, S. Kawata, and S. Minami, "Optical chemical sensor based on surface plasmon measurement," *Applied Optics*, vol. 27, no. 6, pp. 1160-1163, 1988.
- [64] L-M. Zhang, and D. Uttamchandani, "Optical chemical sensing employing surface plasmon resonance," *Electronics Letters*, vol. 24, no. 23, pp. 1469-1470, 1988.
- [65] B. Liedberg, C. Nylander, and I. Lunström, "Surface plasmon resonance for gas detection and biosensing." *Sensors and actuators*, vol. 4, pp. 299-304, 1983.
- [66] D. C. Cullen, and C. R. Lowe, "A direct surface plasmon—polariton immunosensor: Preliminary investigation of the non-specific adsorption of serum components to the sensor interface," *Sensors and Actuators B: Chemical*, vol. 1, no. 1, pp. 576-579, 1990.

- [67] D.C. Cullen, R. G. W. Brown, and C. R. Lowe, "Detection of immuno-complex formation via surface plasmon resonance on gold-coated diffraction gratings," *Biosensors*, vol. 3, no. 4, pp. 211-225, 1988.
- [68] C. F. Bohren, "How can a particle absorb more than the light incident on it?" *American Journal of Physics*, vol. 51, no. 4, pp. 323-327, 1983.
- [69] P. Zijlstra, and M. Orrit, "Single metal nanoparticles: optical detection, spectroscopy and applications," *Reports on Progress in Physics*, vol. 74, no. 10, pp. 106401, 2011.
- [70] K. L. Wustholz, A.-I. Henry, J. M. McMahon, R. G. Freeman, N. Valley, M. E. Piotti, M. J. Natan, G. C. Schatz, and R. P. Van Duyne. "Structure-Activity Relationships in Gold Nanoparticle Dimers and Trimers for Surface-Enhanced Raman Spectroscopy," *Journal of the American Chemical Society*, vol. 132, no. 31, pp. 10903-10910, 2010.
- [71] S. Kühn, U. Håkanson, L. Rogobete, and V. Sandoghdar, "Enhancement of single-molecule fluorescence using a gold nanoparticle as an optical nanoantenna," *Physical review letters*, vol. 97, no. 1, pp. 017402, 2006.
- [72] L. Novotny, and S. J. Stranick, "Near-field optical microscopy and spectroscopy with pointed probes," *Annu. Rev. Phys. Chem.*, vol. 57, pp. 303-331, 2006.
- [73] M. T. Wenzel, T. Härtling, P. Olk, S. C. Kehr, S. Grafström, S. Winnerl, M. Helm, and L. M. Eng. "Gold nanoparticle tips for optical field confinement in infrared scattering near-field optical microscopy," *Optics express*, vol. 16, no. 16, pp. 12302-12312, 2008.
- [74] K. Sokolov, M. Follen, J. Aaron, I. Pavlova, A. Malpica, R. Lotan, and R. Richards-Kortum, "Real-time vital optical imaging of precancer using anti-epidermal growth factor receptor antibodies conjugated to gold nanoparticles," *Cancer research*, vol. 63, no. 9, pp. 1999-2004, 2003.
- [75] X. Huang, I. H. El-Sayed, W. Qian, and M. A. El-Sayed, "Cancer cell imaging and photothermal therapy in the near-infrared region by using gold nanorods," *Journal of the American Chemical Society*, vol. 128, no. 6, pp. 2115-2120, 2006.
- [76] H. El-Sayed, X. Huang, and M. A. El-Sayed, "Selective laser photo-thermal therapy of epithelial carcinoma using anti-EGFR antibody conjugated gold nanoparticles," *Cancer letters*, vol. 239, no. 1, pp. 129-135, 2006.
- [77] X. Xu, J. Wang, K. Jiao, and X. Yang, "Colorimetric detection of mercury ion ( $Hg^{2+}$ ) based on DNA oligonucleotides and unmodified gold nanoparticles sensing system with a tunable detection range," *Biosensors and Bioelectronics*, vol. 24, no. 10, pp. 3153-3158, 2009.

- [78] C. M. Cobley, S. E. Skrabalak, D. J. Campbell, and Y. Xia. "Shape-controlled synthesis of silver nanoparticles for plasmonic and sensing applications," *Plasmonics*, vol. 4, no. 2, pp. 171-179, 2009.
- [79] K.-S. Lee, and M. A. El-Sayed, "Gold and silver nanoparticles in sensing and imaging: sensitivity of plasmon response to size, shape, and metal composition," *The Journal of Physical Chemistry B*, vol. 110, no. 39, pp. 19220-19225, 2006.
- [80] K. J. Lee, P. D. Nallathamby, L. M. Browning, C. J. Osgood, and X.-H. N. Xu. "In vivo imaging of transport and biocompatibility of single silver nanoparticles in early development of zebrafish embryos," *ACS Nano*, vol. 1, no. 2, pp.133-143.
- [81] C. McDougall, D. J. Stevenson, C. T. Brown, F. G.-M., and K. Dholakia, "Targeted optical injection of gold nanoparticles into single mammalian cells," *Journal of biophotonics*, vol. 2, no. 12, pp. 736-743, 2009.
- [82] A. S. Urban, T. Pfeiffer, M. Fedoruk, A. A. Lutich, and J. Feldmann, "Single-Step Injection of Gold Nanoparticles through Phospholipid Membranes," *ACS nano* 5, no. 5, pp. 3585-3590, 2011.
- [83] G. William, B. Kuyken, X. Liu, M. V. Camp, S. Assefa, D. Gill, T. Barwicz, S. Shank, Y. Vlasov, R. Osgood, R. Baets, and G. Roelkens, "Mid-IR Silicon Photonics," *Optical Fiber Communication Conference*. Optical Society of America, 2013.
- [84] Shiroma, Cecilia and Rodriguez-Saona, Luis, "Application of NIR and MIR spectroscopy in quality control of potato chips," *Journal Of Food Composition and Analysis*, vol. 22, no. 6, pp. 596-605, 2009.
- [85] P. Werle, F. Slemra, K. Maurera, R. Kormannb, R. Mücke, and B. Jänkerd, "Near and mid-IR laser optical sensors for gas analysis," *Optics and Lasers in Engineering*, vol. 37, no. 2, pp. 101-114, 2002.
- [86] U. Willer, M. Saraji, A. Khorsandi, P. Geiser, and W. Schade, "Near-and mid-IR laser monitoring of industrial processes, environment and security applications," *Optics and Lasers in Engineering*, vol. 44, no. 7, pp. 699-710, 2006.
- [87] S. Law, V. Podolskiy, and D. Wasserman, "Towards nano-scale photonics with micro-scale photons: the opportunities and challenges of mid-infrared plasmonics," *Nanophotonics* 2, no. 2, pp. 103-130, 2013.
- [88] These data, produced using the program IRTRANS4, were obtained from the UKIRT worldwide web pages, "<http://www.jach.hawaii.edu/UKIRT/astrophysics/utis/atmos-index.html>," accessed 7/29/14.



- [89] H. H. P. T. Bekman, J. C. van den Heuvel, F. J. M. van Putten, and Ric Schleijsen, "Development of a mid-IR laser for study of infrared countermeasures techniques," *European Symposium on Optics and Photonics for Defence and Security*. International Society for Optics and Photonics, 2004.
- [90] A. Godard, "Infrared (2–12  $\mu\text{m}$ ) solid-state laser sources: a review," *Comptes Rendus Physique* vol. 8, no. 10, pp. 1100-1128, 2007.
- [91] M. W. Todd, R. A. Provencal, T. G. Owano. B. A. Paldus, A. Kachanov, K. L. Vodopyanov, M. Hunter, S. L. Coy, J. I. Steinfeld, and J. T. Arnold, "Application of mid-IR cavity-ringdown spectroscopy to trace explosives vapor detection using a broadly tunable (6–8  $\mu\text{m}$ ) optical parametric oscillator," *Applied Physics B*, vol. 75, no. 2-3, pp. 367-376, 2002.
- [92] T. Töpfer, K. P. Petrov, Y. Mine, D. Jundt, R. F. Curl and F. K. Tittel, "Room-temperature mid-IR laser sensor for trace gas detection," *Applied Optics*, vol. 36, no. 30, pp. 8042-8049, 1997.
- [93] J. Faist, Jerome, F. Capasso, C. Sirtori, D. L. Sivco, J. N. Baillargeon, A. L. Hutchinson, Sung-Nee G. Chu, and A. Y. Cho, "Quantum cascade laser," *Science*, vol. 264, no. 5158, pp. 553-556, 1994.
- [94] J. Faist, F. Capasso, C. Sirtori, D. L. Sivco, J. N. Baillargeon, A. L. Hutchinson, S. G. Chu, and A/ Y. Cho, "High power mid-infrared ( $\lambda \sim 5 \mu\text{m}$ ) quantum cascade lasers operating above room temperature," *Applied Physics Letters*, vol. 68, no. 26, pp. 3680-3682, 1996.
- [95] Y. Yao, A. J. Hoffman, and C. F. Gmachl. "Mid-infrared quantum cascade lasers," *Nature Photonics*, vol. 6, no. 7, pp. 432-439, 2012.
- [96] B. F. Levine, "Quantum-well infrared photodetectors," *Journal of Applied Physics*, vol. 74, no. 8, pp. R1-R81, 1993.
- [97] J. C. Ginn, R. L. Jarecki Jr, E. A. Shaner, and Paul S. Davids, "Infrared plasmons on heavily-doped silicon," *Journal of Applied Physics*, vol. 110, no. 4 pp. 043110, 2011.
- [98] J. Y. Andersson, L. Lundqvist, and Z. F. Paska, "Quantum efficiency enhancement of AlGaAs/GaAs quantum well infrared detectors using a waveguide with a grating coupler," *Applied Physics Letters*, vol. 58, no. 20, pp. 2264-2266, 1991.
- [99] J. Y. Andersson and L. Lundqvist, "Near-unity quantum efficiency of AlGaAs/GaAs quantum well infrared detectors using a waveguide with a doubly periodic grating coupler," *Applied Physics Letters*, vol. 59, no. 7, pp. 857-859, 1991.
- [100] K. W. Berryman, S. A. Lyon, and M. Segev, "Mid-infrared photoconductivity in self-organized InAs quantum dots," *Applied Physics Letters*, vol. 79, no. 3, pp. 421-423. 1997.

- [101]Y. Wei, A. Gin, M. Razeghi, and G. J. Brown, "Advanced InAs/GaSb superlattice photovoltaic detectors for very long wavelength infrared applications," *Applied Physics Letters*, vol. 80, no. 18, pp. 3262-3264, 2002.
- [102]N. Yu, Q.J. Wang, M.A. Kats, J.A. Fan, F. Capasso, S.P. Khanna, L. Li, A.G. Davies and E.H. Linfield, "Terahertz plasmonics," *Electronics Letters*, vol. 46, no. 26, pp. 52-57, 2010.
- [103]J. B. Pendry, L. Martin-Moreno, and F. J. Garcia-Vidal, "Mimicking surface plasmons with structured surfaces," *Science*, vol. 305, no. 5685, pp. 847-848, 2004.
- [104]F. Marquier, K. Joulain, J. P. Mulet, R. Carminati, and J. J. Greffet, "Engineering infrared emission properties of silicon in the near field and the far field." *Optics communications*, vol. 237, no. 4, pp. 379-388, 2004.
- [105]R. Soref, J. Hendrickson, and J. W. Cleary, "Mid-to long-wavelength infrared plasmonic-photonics using heavily doped n-Ge/Ge and n-GeSn/GeSn heterostructures," *Optics express*, vol. 20, no. 4, 3814-3824, 2012.
- [106]D. M. Caughey and R. E. Thomas, "Carrier mobilities in silicon empirically related to doping and field," *Proceedings of the IEEE*, vol. 55, pp. 2192, 1967.
- [107]H. M. K. Wong and A. S. Helmy, "Optically defined plasmonic waveguides in crystalline semiconductors at optical frequencies," *JOSA B*, vol. 30, no. 4, pp. 1000-1007, 2013.
- [108]Caughey, D. M, Thomas, R. E, "Carrier mobilities in silicon empirically related to doping and field," *Proceedings of the IEEE*, vol. 55, pp. 2192, 1967.
- [109]Brigham Young University, "Resistivity & Mobility Calculator/Graph for Various Doping Concentrations in Silicon," Online: <http://www.cleanroom.byu.edu/ResistivityCal.phtml>, [3 September 2013].
- [110]T F. Krauss, "Slow light in photonic crystal waveguides," *Journal of Physics D: Applied Physics*, vol. 40, no. 9, pp. 2666, 2007.
- [111]T. Yang and K. B. Crozier, "Analysis of surface plasmon waves in metal-dielectric-metal structures and the criterion for negative refractive index," *Optics Express*, vol. 17, no. 2, pp. 1136-1143, 2009.
- [112]M. A. Swillam, and A. S. Helmy, "Analysis and applications of 3D rectangular metallic waveguides," *Optics Express*, vol. 18, no. 19, pp. 19831-19843, 2010.
- [113]E. Feigenbaum, and M. Orenstein, "Backward propagating slow light in inverted plasmonic taper," *Optics express*, vol. 17, no. 4, pp. 2465-2469, 2009.
- [114]M. Wegener, G. Dolling, and S. Linden, "Plasmonics: Backward waves moving forward," *Nature materials*, vol. 6, no. 7, pp. 475-476, 2007.

- [115]G. Veronis, and S. Fan, "Bends and splitters in metal-dielectric-metal subwavelength plasmonic waveguides," *Applied Physics Letters*, vol. 87, no. 13, 2005.
- [116]T. Baehr-Jones, A. Spott, R. Ilic, A. Spott, B. Penkov, W. Asher, and M. Hochberg, "Silicon-on-sapphire integrated waveguides for the mid-infrared," *Optics express*, vol. 18, no. 12, pp. 12127-12135, 2010.
- [117]M. Piliarik, P. Kvasnička, N. Galler, J. R. Krenn, and J. Homola, "Local refractive index sensitivity of plasmonic nanoparticles," *Optics express*, vol. 19, no. 10, pp. 9213-9220, 2011.
- [118]J. S. Sekhon, and S. S. Verma. "Refractive index sensitivity analysis of Ag, Au, and Cu nanoparticles," *Plasmonics*, vol. 6, no. 2, no. 311-317, 2011.